ISSN 2149-2123

JOURNAL OF SCIENCE & ENGINEERING

HITITE

HJSE Official Journal of Graduate School of Natural & Applied Sciences, Hitit University www.hjse.hitit.edu.tr

Volume 2, Issue 2, 2015

www.hjse.hitit.edu.tr

JOURNAL OF SCIENCE & ENGINEERING
HITTITE

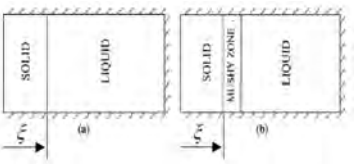

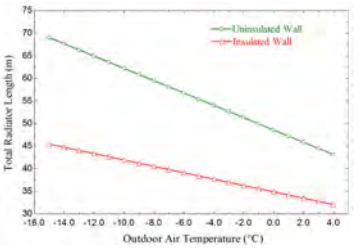

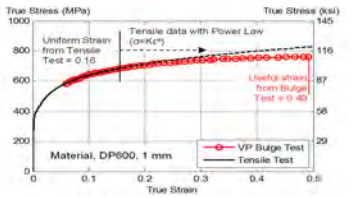

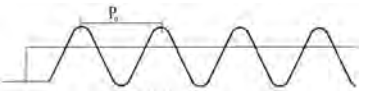

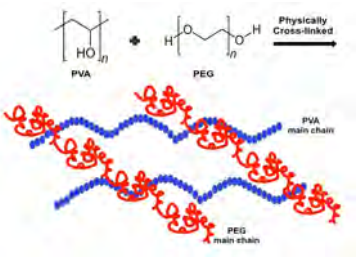

JOURNAL OF SCIENCE & ENGINEERING
HITTITE

CONTENT

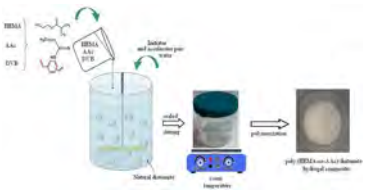

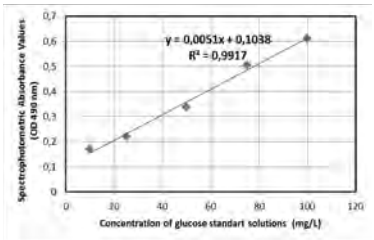

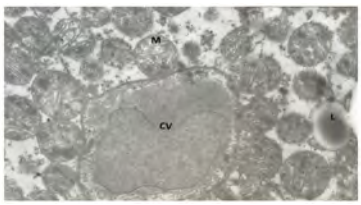

Owner
Prof. Dr. Reha Metin ALKAN
on behalf of Hitit University

Editor-in-chief
Prof. Dr. Ali Kılıçarslan

Associate Editors
Assoc. Prof. Dr. D. Ali Köse
Asst. Prof. Dr. Öncü Akyıldız

Production
Dr. Kazım Köse

Editor's Office
Tel: +90 364 227 45 33 / 12 36
Fax: +90 364 227 45 35
Email: alikilicarslan@hitit.edu.tr

Subscription Service:
Tel: +90 364 227 45 33 / 12 82
Fax: +90 364 227 45 35
Email: hjse@hitit.edu.tr

EDITORIAL BOARD

Journal Name	: HITTITE JOURNAL OF SCIENCE AND ENGINEERING
Year	: 2015
Managing Editor	: Prof. Dr. Ali KILIÇARSLAN
Managing Office	: Hitit University Graduate School of Natural and Applied Sciences
Managing Office Tel	: +90 364 219 40 00
Publication Language	: English
Publication Type	: Peer Reviewed, Open Access, International Journal
Delivery Format	: 2 times a year (semi-annually)
Print ISSN	: 2149-2123
Publisher	: Bir Medya
Publisher Address	: Yeniyol Mah. Gazi 12. Sok. No:9/13 ÇORUM
Publisher Tel	: +90 364 225 66 64

As we bid farewell to 2015 and welcome 2016, I want to take this opportunity to wish all our readers a safe and Happy New Year. This new issue of Hittite Journal of Science and Engineering contains eight manuscripts from the disciplines of biology, materials science and engineering, mechanical engineering, electrical engineering. These manuscripts were first screened by Section Editors using plagiarism prevention software and then reviewed and corrected according to the reviewer's comments. I would like to express my gratitude to all our authors and contributing reviewers of this issue.

Indexing and abstracting services facilitate the broadest dissemination of information by pointing researchers to articles that are relevant to the field. With this issue, we realize that we have already indexed by some discipline specific databases like molecularly imprinted polymers database (MIPdatabase), medical plants database (StuartxChange) as well as some multidiscipline academic databases like Google Scholar or ResearchBib. I would like to inform all our readers that we are in the evaluation period to be indexed and abstracted in TR Dizin (ULAKBIM), Scopus and Web of Science.

I would like to thank to the President of Hitit University, Prof. Dr. Reha Metin Alkan, for his constant interest in HJSE and also to the Associate Editors of HJSE, namely Dr. Dursun Ali Kose and Dr. Oncu Akyildiz, as well as our Production Editor, Dr. Kazim Kose for their invaluable efforts in making of the journal.

It's my pleasure to invite the researchers and scientists from all branches of science and engineering to join us by sending their best papers for publication in Hittite Journal of Science and Engineering.

Dr. Ali Kilicarslan

Editor-in-Chief

Director of Graduate School of Natural and Applied Sciences of Hitit University

Hittite Journal of Science and Engineering, 2015, 2 (2) 127-144
ISSN NUMBER: 2149-2123
DOI: 10.17350/HJSE19030000017

Numerical Solution of Two Phase Solidification Problem Using Dynamic Substructuring Based on Adaptive Error Estimation

Ozgur Uyar and Ata Mugan
Istanbul Technical University, Department of Mechanical Engineering, Gumussuyu, Istanbul, TURKEY

ABSTRACT

Numerical solution of solidification of metals with a sharp front, in particular solidification of lead, is investigated. Considering the fact that the associated CPU time and memory requirement may be costly for large domains, alternatives are searched. It is observed that using a substructuring technique with a local mesh refinement is promising. Following, by the use of an adaptive error estimation algorithm to find the location of solidification front and mushy zone, dynamic substructuring technique is developed to decrease the computational cost and to increase the accuracy of results. Superconvergent patch recovery technique is used to obtain the heat fluxes to evaluate the error energy norm of elements at each analysis step. Solidification front, mushy zone and elements having errors above a threshold value are captured with the error estimator. Then, elements having errors above the threshold value are refined by creating a substructure which is independent from the original global mesh. Equations of the global coarse mesh are augmented with the equations of the substructure. Employing the equations of the original coarse mesh help reduce the computational cost. Numerical solutions are presented and it is shown that the proposed approach has advantages over the alternative methods and, by the virtue of the adaptive error estimation algorithm, significantly decreases the CPU time of numerical solutions while it increases the accuracy of solutions and locates precisely the solidification front and mushy zone.

Key Words:
Solidification; Finite Element Methods; Substructuring; Stefan Problem; Error Estimation

Article History:
Received: 2015/08/09
Accepted: 2015/09/16
Online: 2015/12/30

***Correspondence to**: Ozgur Uyar, Istanbul Technical University, Faculty of Engineering, Department of Mechanical Engineering, Istanbul, Turkey*
Tel: +90 (312) 497-46 19
Fax: +90 (312) 497-43 01
E-Mail: ozuyar78@hotmail.com

INTRODUCTION

Solidification with a sharp front is a moving boundary value problem, i.e. a Stefan problem which is very important for several engineering applications. When the historical background of numerical solutions of solidification problems are examined, relevant works in literature are summarized as follows.

Lynch and O'Neill [1] developed a moving mesh technique for finite element phase change simulation. Lynch and Sullivan [2] calculated the heat flux at the phase boundary. Kuang and Atluri [3] developed another moving mesh method. Tamma and Saw [4] developed an adaptive mesh refinement for the p-version finite element method (FEM) to improve the solutions locally. Zabaras et al. [5] used front tracking FEM for calculation of temperature and stress fields in a solidfying pure metal to understand the formation of cracks due to the induced thermal stress field. Ro [6] investigated the development of heat transfer in phase change processes. Ghosh and Moorthy [7] proposed an alternative Arbitrary Lagrangian-Eulerian (ALE) approach to solidification problems. Wang et al. [8] examined a class of phase-field models for crystallization of pure substances from its melt. Gandin and Rappaz [9] developed a new algorithm based upon a 2-dimensional cellular automation technique for the simulation of dendritic grain formulation during solidification. Franca and Haghigi [10] developed a new adaptive finite element procedure for the solution of transient heat conduction problems. Juric and Tryggvason [11] presented a front-tracking method to simulate time dependent two-dimensional dendritic solidification of pure substances based on finite difference approximation of the heat equation and for explicit tracking of the liquid-solid interface. Chen et al. [12] developed a two-dimensional

finite element program which can be applied to solve the solidification of pure metals and alloys, that includes the effects of natural convection in liquid using temperature recovery scheme. Provatas et al. [13] studied the evolution of solidification microstructures using a phase-field model computed on an adaptive finite element grid. Lewis and Ravindran [14] studied the coupling of the solidification analysis based on the heat conduction equation with fluid flow and thermal analysis for metal casting where various algorithms available in literature for modeling of solidification problems are discussed. Merle and Dolbow [15] applied the eXtended finite element method (X-FEM) to thermal problems with moving heat sources and phase boundaries which provides accurate solutions to transient thermal and phase change problems on fixed finite element meshes. Chessa et al. [16] applied the X-FEM to multi-dimensional Stefan problems whose approximation represents the phase interface and associated discontinuity in temperature gradient within an element, and the phase interface can be evolved without re-meshing or the use of artificial heat capacity techniques. Ji et al. [17] presented the application of the hybrid XFEM/Level Set Method (LSM) to two dimensional solidification problems and used a new approach with the XFEM for this class of problems whereby the partition of unity is constructed with $\mathcal{C}^1(\Omega)$ polynomials and enriched with a $\mathcal{C}^0(\Omega)$ function. Zhao et al. [18] presented a two-dimensional model for simulation of the directional solidification of dendritic alloys and solved the transient energy and solute conservation equations using FEM discretizations; the energy equation was solved by a fixed mesh of bilinear elements in which the interface is tracked and the solute conservation equation is solved by an independent, variable mesh of quadratic triangular elements in the liquid phase only while the triangular mesh used in analyses is regenerated at each time step to accommodate the changes in the interface position using a Delaunay triangulation. Zang and Xu [19] developed a FEM model to compute the thermal and thermomechanical phenomena during pulsed laser induced melting and solidification where they used element removal and reactivation method in order to release and retrieve the stress and strain during melting and solidification. Takaki et al. [20] performed phase-field simulations during solidification of a binary alloy and used adaptive mesh refinement techniques during the FEM analysis in order to conduct the phase-field simulations effectively. Zabaras et al. [21] studied dendritic solidification of pure materials from an undercooled melt using the XFEM/LSM for modeling of the thermal problem and a volume averaged stabilized FEM formulation for modeling the fluid flow where they presented a dimension-independent methodology to simulate the growth of dendrites in the presence of convection. Their formulation is based on the XFEM/LSM to simulate the temperature evolution and a volume-averaged stabilized FEM formulation for the velocity evolution. Zhang et al. [22] developed an integrated meshless thermal–mechanical analysis system with a meshless solidification model based on Finite Point Method and the Meshless Local Petrov-Galerkin method based elastic–plastic analysis model where they calculated heat transfer and solidification using the finite point meshless method. Wang et al. [23] applied moving grid method for the solution of a phase-field model for dendritic growth in two- and three-dimensions where moving mesh technique is used and the mesh redistribution is realized by solving an elliptic boundary control problem together with a nonlinear multi-grid algorithm. Hu et al. [24] proposed a multi-mesh adaptive finite element method for simulating the dendritic growth in two- and three-dimensions and implemented the multi-mesh h-adaptive mesh refinement algorithm to enhance the computational efficiency. Lee and Sundararaghavan [25] studied a multi-scale analysis scheme for solidification based on two-scale computational homogenization and used a non-linear coupled macro-micro FEM model for addressing the fluid solidification problems and tracked solidifying interface using an adaptive meshing strategy. Li and Shopple [26] developed a new FEM level set approach to simulate the interface motion where they applied the method to the classical solidification problem to locate the dendrites whose key feature is the construction of an interface-fitted mesh and its unrefinement with respect to a fixed base mesh at each time step of evolution. O'Hara et al. [27] presented the application of the generalized finite element method (GFEM) with global-local enrichments to problems of transient heat transfer involving localized features where the GFEM is utilized in order to numerically construct general, specially-tailored shape functions yielding high levels of accuracy on coarse FEM meshes. Chen et al. [28] coupled the macro and micro analysis to predict the microstructure growth of magnesium alloys in directional solidification process and used the FEM to calculate undercooling temperature, by which the macro analysis results were coupled into the micro analysis where very fine mesh is used in order to calculate temperatures. Chen et al. [29] proposed a coupled Cellular Automation – FEM model to predict the grain structure formation during Gas Tungsten Arc Welding where the FEM is used to solve the heat flow problem based on an adaptive meshing. Ghoneim [30] used a new meshfree interface-finite element method for numerical modeling of isothermal solutal melting and solidification in binary systems where the implicitly represented liquid-solid interface is allowed to arbitrarily intersect the finite elements where meshfree solid-liquid interface interface nodes are generated automatically based on the distribution of the signed distance function.

When the above listed studies are examined, it is observed that computational methods used to solve the

Stefan problem can be classfied into the five classes such as the moving mesh method, adaptive remeshing method, XFEM, generalized FEM and meshless methods. Moving mesh methods update the mesh in order to conform the element edges to the solidification front; the mesh is updated totally or locally and mesh regeneration for complex interfaces is difficult. Adaptive remeshing methods use error estimators to determine the errors around solidification front and these algorithms refine the mesh by remeshing to reduce the error levels. On the other hand, the XFEM, generalized FEM and meshless methods are very popular in recent years for interface problems. These methods capture the discontinuities such as the solidification front by using LSM. Then, extra degrees of freedom (DOF) are added to the elements or extra nodes are added to the mesh in order to obtain improved solutions around the solidification front. Advantage of these methods is that the original mesh is not updated when the extra DOF or extra nodes are added to the original mesh; however, the associated matrices are to be updated at each analysis step that slows down the solution procedure.

All of the methods mentioned above require the update of associated matrices at each analysis step due to the updated mesh, refined mesh, adding extra DOF or adding nodes; as a result, the CPU time and memory requirement of these methods increase significantly.

Motivated by the drawbacks of above methods, a new technique using FEM is proposed called dynamic substructuring approach based on adaptive error estimation. In this method, the original FEM mesh is not changed during the solution steps and accurate solutions can be obtained using very coarse meshes. In particular, two phase Stefan problem of lead material is considered in this study. The computational domain is meshed with a coarse mesh and propagation of solidification front, mushy zone and elements having errors above a threshold value are captured with an error energy norm estimator at each analysis step. Then, a substructure independent from the global model is generated by refining the elements having errors above the error threshold; thus, remeshing of the entire original mesh at each analysis step is avoided that helps reduce the CPU time considerably. Substructure boundary conditions are obtained from the nodes of global model which are the neighbours to the elements used for the substructure. Following, the original global equations are augmented by the substructure equations and then the coupled equations of original and substructure equations are solved simultaneously. The mesh refinement is adaptive based on the adaptive error estimator calculations and the refined regions are removed in the substructure if their error level reduces to below the threshold value during analysis steps.

The main advantage of the proposed approach is that the substructure generation does not affect the original global matrices and a small portion of the coarse global mesh is refined automatically; thus, there is no need for remeshing the original coarse mesh at each analysis step. In sum, the original global mesh is kept unchanged during the whole analysis steps. Therefore, the proposed method does not employ any remeshing algorithm that slows down the numerical solutions that are followed in the moving mesh method, adaptive remeshing method, XFEM, generalized FEM and meshless methods in literature. Moreover, the initial global equations can be used throughout the solution procedure if associated FEM matrices are unchanged that further reduces the CPU time of the proposed approach. Numerical solutions are presented and it is shown that the proposed approach has advantages over the alternative methods and, by the virtue of the adaptive error estimation algorithm, significantly decreases the CPU time of numerical solutions while it increases the accuracy of solutions and locates precisely the solidification front and mushy zone.

Solidification and Mathematical Equations

During the solidification process, liquid metal changes its phase, conduction heat transfer occurs conduction heat transfer occurs in both solid phase and liquid phase. It also occurs between these two phases. Convective heat transfer occurs in liquid phase and at solidification front. In this study, heat convection motion of liquid metal is ignored. The mushy zone is also considered in all analyses. Solidification process is described mathematically with heat conduction and heat convection equations. Equations used in FEM analyses are presented below.

The transient heat transfer by conduction can be described by the following equation [10]

$$\rho C_p \frac{\partial T}{\partial t} = \nabla(\lambda \nabla \mathrm{T}) + Q \tag{1}$$

where ρ is the density, C_p specific heat, T temperature, t time, λ thermal conductivity and Q external heat source.

The heat transfer between solidification front and liquid metal occurs by convection associated with the release of latent heat of solidification that is represented by the following equation [31]

$$\lambda \frac{\partial T}{\partial x} = L\rho \frac{\partial \xi}{\partial t} + h\nabla \mathrm{T} \tag{2}$$

At the solidification front, temperature $\mathrm{T}(t, \xi(t))$ will satisfy the following condition [31]

$$T\left(t,\xi(t)\right)=T_c \tag{3}$$

where L is the latent heat of crystallization, ξ position of solidification front, h coefficient of heat convection at the solidification front interface, ∇T overheating and T_c crust temperature at which solidification starts.

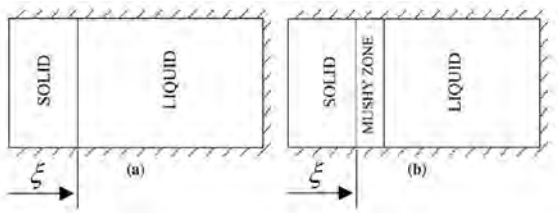

Figure 1. Solidification scheme: (a) pure metals and (b) alloys [32].

Figure 1 shows the process of solidification for pure metals and alloys schematically [32]. Solidification starts when the temperature of liquid metal (T_l) decreases to melting temperature (T_m) for pure metals. When the alloys are considered, a mushy zone starts to develop at melting temperature and solidification starts at the crust temperature. Mushy zone temperature varies between the crust temperature and melting temperature. In this zone, the liquid and solid phases are mixed. Figure 2 shows the phase change depending on temperature for alloys.

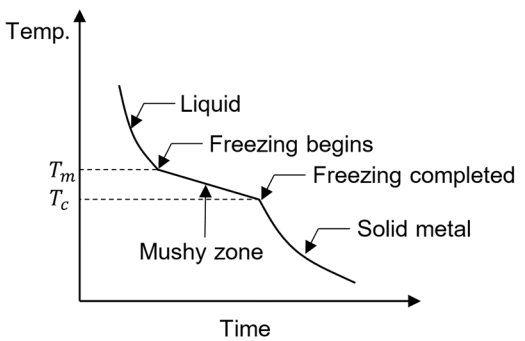

Figure 2. Phase change depending on temperature for alloys.

In this study, solidification characteristics of lead is studied with the proposed method. The experimental studies on the solidification of lead are completed using an experimental equipment by Bratu [31] where it is reported that the crust temperature of lead is 320°C and melting temperature of lead is 327°C.

Temperature dependent thermodynamic and thermophysical quantities of lead can be determined using the relationships given by Equations (4) to (6)

For $T \le 600.2\ K$

$$\lambda(T)=(-6E-8)T^3+(8E-5)T^2-0.0428T+42.89 \tag{4}$$

Equation (4) is obtained with the least squares curve fit to the tabular values given in [33]. This equation is valid from 123.2 K to 600.2 K. In addition, for $T \le 600.2\ K$, C_p and ρ are given by [34]

$$C_p=0.156391T^{-0.32702}e^{0.001089T}e^{-31.14/T} \tag{5}$$

$$\rho=11340\,kg/m^3 \tag{6}$$

Moreover, for $T > 600.2\ K$, we have [35]

$$\lambda(T)=0.011T+9.2 \tag{7}$$

$$C_p=176.2-(4.923E-2)T+(1.544E-5)T^2-(1.524E6)T^{-2} \tag{8}$$

$$\rho=11441-1.2795T \tag{9}$$

2-D Finite Element Formulation for Solidification Problem

The semi-discrete FEM equations for linear transient heat transfer problems can be cast into the following form [36]

$$[C]\{\dot{T}(t)\}+([K_c]+[K_h])\{T(t)\}=\{R_Q(T,t)\}+\{R_q(t)\}+\{R_h(t)\} \tag{10}$$

In this study, heat generation and heat flux are assumed to be zero and heat convection is considered only at the solidification front. Thus, the above formulation reduces to

$$[C]\{\dot{T}(t)\}+([K_c]+[K_h])\{T(t)\}=\{R_h(t)\} \tag{11}$$

where $[C]$ is the capacity matrix, $[K_c]$ conductivity matrix, $[K_h]$ convection matrix and $\{R_h(t)\}$ convective heat vector.

Time Integration

Equation (11) is a parabolic semi-discrete equation, and time dependent numerical solution of this equation can be obtained with the generalized trapezoidal family of methods which consists of the following equations [37]

$$C\dot{T}_{n+1}+KT_{n+1}=R_{n+1} \tag{12}$$

$$T_{n+1}=T_n+\Delta t\dot{T}_{n+\alpha} \tag{13}$$

$$\dot{T}_{n+\alpha}=\left[(1-\alpha)\dot{T}_n+\alpha\dot{T}_{n+1}\right] \tag{14}$$

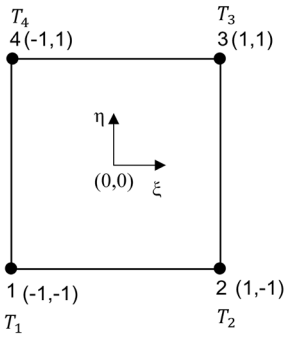

Figure 3. Four noded quadrilateral element in normal coordinates.

where T_n and $\dot{T}_n$ are respectively the FEM approximations of $T(t_n)$ and $\dot{T}(t_n)$ at discrete time steps, $R_{n+1} = R(t_{n+1})$, Δt is the time step assumed to be constant and α is a parameter in the interval [0, 1]. Note that α is chosen as 0.5 which corresponds to trapezoidal rule [37].

Finite Element Formulation

In this study, 4 noded quadrilateral elements in normal coordinates shown in Figure 3 are used for element formulations.

Bilinear shape functions of the element are given below [38]

$$N_1 = \frac{1}{4}(1-\xi)(1-\eta) \tag{15}$$

$$N_2 = \frac{1}{4}(1+\xi)(1-\eta) \tag{16}$$

$$N_3 = \frac{1}{4}(1+\xi)(1+\eta) \tag{17}$$

$$N_4 = \frac{1}{4}(1-\xi)(1+\eta) \tag{18}$$

The temperature at an arbitrary point inside an element can be approximated by

$$T(\xi,\eta) = N_1(\xi,\eta)T_1 + N_2(\xi,\eta)T_2 + N_3(\xi,\eta)T_3 + N_4(\xi,\eta)T_4 \tag{19}$$

When steady-state conditions do not prevail, temperature change in a unit volume of material is resisted by thermal mass that depends on the mass density ρ of the material and its specific heat C_p. The capacity matrix $[C]$ is built by assembling the element heat capacity matrices $[C_e]$ [39]; namely,

$$[C] = \sum_{(assemble)} [C]_e \text{ where } [C]_e = \int N^T N \rho C_p dV \tag{20}$$

In this study, lumped capacity matrix formulation is used in the developed FEM code. For a rectangular element, lumped capacity matrix is obtained by the row-sum technique [37]; namely, we simply divide the summation of heat capacity matrix $[C]_e$ components in a row by four and put the result along the diagonal of the same row of $[C]_e$. Thus, if we employ 4 noded rectangular elements, we may use the following for an internal node [40]

$$c_{ii} = \frac{\rho C_p A}{4} \tag{21}$$

in the main diagonal of the capacity matrix $[C]_e$. Thus, the lumped capacity matrix $[C]_e$ has the following diagonal form [40]

$$[C]_e = \frac{\rho c A}{4}\begin{bmatrix} 1 & 0 & 0 & 0 \\ 0 & 1 & 0 & 0 \\ 0 & 0 & 1 & 0 \\ 0 & 0 & 0 & 1 \end{bmatrix} \tag{22}$$

Such a diagonal capacity matrix provides considerable computational advantage because they are easy to store and invert. Then, element conductivity matrix $[K_c]_e$ can be evaluated as follows

$$[K_c]_e = \int_{A_e} [B]^T [\lambda][B] dA \tag{23}$$

where $[B]$ is the temperature differentiation matrix, $[\lambda]$ thermal conductivity matrix and A_e area of element as follows

$$[B] = \begin{bmatrix} \frac{\partial N_1}{\partial x} & \frac{\partial N_2}{\partial x} & \frac{\partial N_3}{\partial x} & \frac{\partial N_4}{\partial x} \\ \frac{\partial N_1}{\partial y} & \frac{\partial N_2}{\partial y} & \frac{\partial N_3}{\partial y} & \frac{\partial N_4}{\partial y} \end{bmatrix} \tag{24}$$

$$[\lambda] = \begin{bmatrix} \lambda & 0 \\ 0 & \lambda \end{bmatrix} \tag{25}$$

Following, element convection matrix can be expressed as follows [36]

$$[K_h]_e = \int_{S_e} h[N]^T [N] dS \tag{26}$$

where N is shape function matrix, h coefficient of convection and S_e length of convection edge of the element #e. The convective heat vector $\{R_h\}_e$ can be

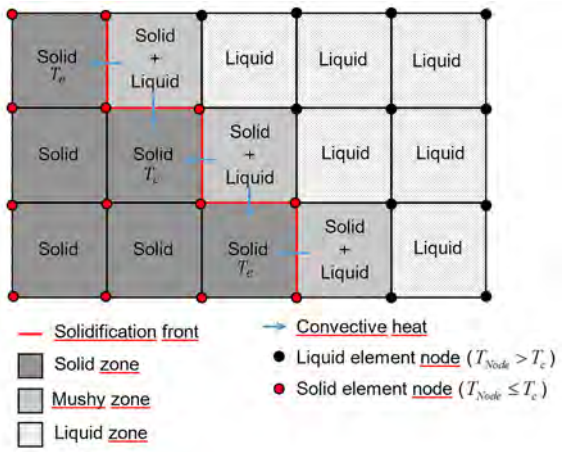

Figure 4. 2-D FEM solution scheme of two phase solidification problem.

calculated by [36]

$$\{R_h\}_e = \int_{S_e} hT_e [N]^T \, dS \tag{27}$$

where T_e is the environment temperature.

Note that heat convection equations are only considered at the solidification front. Hence, T_e value is equal to the average temperature of the neighboring solid element at the solidification front during analysis steps.

The 2-D FEM solution scheme of two phase solidification problem is shown in Figure 4. Note that all elements are liquid at the first analysis step. Temperatures of all nodes are checked after the calculations at each analysis step according to the algorithm described below and the location of solidification front can be determined by this methodology.

When the four nodes of an element are equal or below T_c that element is considered as solid. Solid elements, liquid elements and mixed phase elements are shown in Figure 4. Mixed phase elements located in the mushy zone are considered as liquid due to [31] and the location of solidification front is shown with red lines. Convective heat transfer is only considered at the solidification front (i.e., red edges of mixed phase elements) and it is shown with blue arrows in Figure 4. The environment temperature T_e for heat convection calculations is equal to the average temperature of solid element at the solidification front.

Thermodynamic and thermophsical properties (i.e., ρ, C_p and λ) of the material are temperature dependent which are calculated at the beginning of each analysis step depending on the average temperature of each element.

Adaptive Finite Element Recovery and A Posteriori Error Estimators

It is important to obtain the correct location of solidification front during the analyses due to the effect of heat flux jump at the front. The location of solidification front is assumed to be at element boundaries in this study. Therefore, refined meshes will give more accurate results than the coarse meshes.

The two phase solidification problems involve evolution of surfaces coupled with flux jump boundary conditions across the interfaces [25]. It is known that heat flux jumps cause errors during the numerical solution and these errors can be decreased to allowable levels by refining the mesh around the solidification front. To this end, adaptive finite element recovery techniques can be used. The adaptive error estimator developed by Zienkiewicz and Zhu allows the global error energy norm to be well estimated and also gives a good evaluation of local errors [41].

In an optimal mesh, it is desirable that the distribution of element error energy norm (i.e., $\|e\|_K$) should be almost constant for all elements. Thus, the total permissible error level is determined (assuming that it is found by numerical solutions) as follows [42]

$$\text{Permissible error} \equiv \bar{\eta}\|u\| \approx \bar{\eta}\left(\|q\|^2 + \|e\|^2\right)^{1/2} \tag{28}$$

Then, we could pose a requirement that the error norm in any element #*k* should satisfy

$$\|e\|_K < \bar{\eta}\left(\frac{\|q\|^2 + \|e\|^2}{m}\right)^{1/2} \equiv \bar{e}_m \tag{29}$$

where $\bar{\eta}$ is the permissible error percentage, $\|q\|$ heat flux energy norm, $\|e\|$ heat flux error energy norm and m number of elements.

Since no analytical solution is available for most of the practical problems, an estimated error is calculated based on a recovered solution. The exact error can be written as [43]

$$e_u^{ex} = u^{ex} - u^h \tag{30}$$

where u^{ex} and u^h are the exact and numerical solutions, respectively. Similarly, the heat flux error can be defined as follows

$$e = q^{ex} - q^h \tag{31}$$

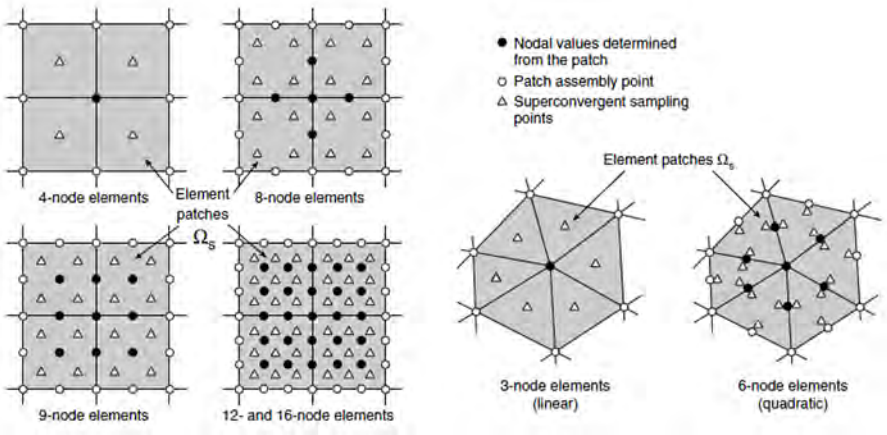

Figure 5. Interior superconvergent patches for quadrilateral elements (i.e., linear, quadratic and cubic) and triangles (i.e., linear and quadratic) [42].

where q^{ex} and q^{h} are the exact and numerical solutions of heat fluxes. Then, temperature error energy norm can be calculated by the following equation

$$\left\|e_u^{ex}\right\| = \left[\int_\Omega \left(u^{ex}-u^h\right)^T \lambda^{-1}\left(u^{ex}-u^h\right) d\Omega\right]^{1/2} \tag{32}$$

and heat flux error energy norm expression is as follows

$$\left\|e\right\| = \left[\int_\Omega \left(q^{ex}-q^h\right)^T \lambda^{-1}\left(q^{ex}-q^h\right) d\Omega\right]^{1/2} \tag{33}$$

Numerical heat fluxes at any point inside an element can be calculated by

$$q^h = \begin{Bmatrix} q_x \\ q_y \end{Bmatrix} = \begin{bmatrix} \lambda & 0 \\ 0 & \lambda \end{bmatrix} \begin{bmatrix} \frac{\partial N_1}{\partial x} & \frac{\partial N_2}{\partial x} & \frac{\partial N_3}{\partial x} & \frac{\partial N_4}{\partial x} \\ \frac{\partial N_1}{\partial y} & \frac{\partial N_2}{\partial y} & \frac{\partial N_3}{\partial y} & \frac{\partial N_4}{\partial y} \end{bmatrix} \begin{Bmatrix} T_1 \\ T_2 \\ T_3 \\ T_4 \end{Bmatrix} \tag{34}$$

Accurate heat flux values are to be calculated to determine the heat flux error. In this study, superconvergent patch recovery (SPR) technique is used for obtaining accurate heat flux values. The concept of superconvergence is that the approximate solutions at some points are more accurate, or in other words, the rate of convergence at those points is higher than those of other points [44]. The SPR technique is employed to recover the heat fluxes from Gauss integration points [37] by using element patches. On each patch, a polynomial expansion for each component of the recovered heat flux field is expressed in the following form [45].

$$\mathrm{q}_i^{ex} = \mathrm{p}(\mathrm{x},\mathrm{y})\,\mathrm{a}_i \tag{35}$$

where i denotes the axes (i.e., x or y axis), $\mathrm{p}(\mathrm{x},\mathrm{y})$ represents a polynomial basis and a_i are unknown coefficients. Usually, the polynomial basis is chosen equal to the non-extended FEM basis [37] for temperature field. A least squares approximation to the values of q^{ex} is evaluated at Gauss integration points of the elements within the patch. Detailed description of the SPR technique is given as follows [42]. Then,

$$p(x,y) = \left[1, \quad \bar{x}, \quad \bar{y}, \quad \ldots, \quad \bar{y}^p\right] \tag{36}$$

$$a_i = \left[a_1, \quad a_2, \quad a_3, \quad \ldots, \quad a_m\right]^T \tag{37}$$

with $\bar{x} = x - x_c$, $\bar{y} = x - y_c$ where x_c and y_c are the coordinates of the interior vertex node describing the patch, e.g., see Figure 5.

For each element patch, a least squares functional is minimized with n sampling points [42].

$$\Pi = \frac{1}{2}\sum_{k=1}^{n}\left[q^h(x_k,y_k) - p_k a_i\right]^2 \tag{38}$$

where

$$p_k = p(x_k,y_k) \tag{39}$$

and $[x_k,y_k]$ corresponds to the coordinates of the superconvergent sampling point k, that yields immediately the coefficients a_i as follows [42].

$$a_i = A^{-1}b_i \tag{40}$$

where

$$A = \sum_{k=1}^{n} p_k^T p_k \text{ and } b_i = \sum_{k=1}^{n} p_k^T q^h(x_k,y_k) \tag{41}$$

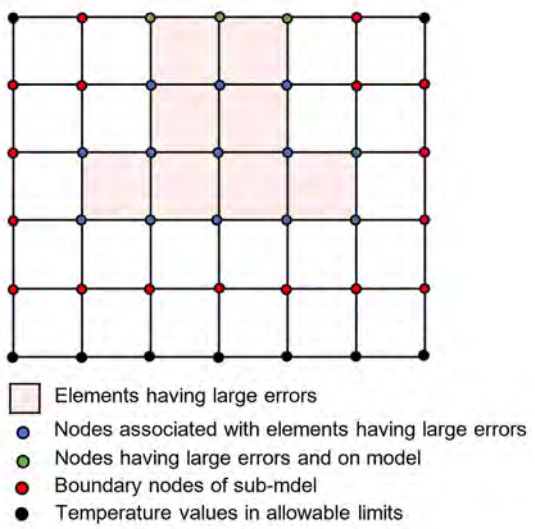

Figure 6. Global model with coarse mesh and elements having large errors.

In this study, center points of elements are selected as superconvergent sampling points and accurate heat flux values q^{ex} at nodes are determined using element patches. Numerical heat flux values q^{h} are determined via extrapolation of the heat flux values at Gauss integration points to the nodes.

Note that the value of permissible error percentage denoted by $\bar{\eta}$ is very important for adaptive finite element recovery. If $\bar{\eta}$ is selected smaller than an optimum value, more elements are captured by the error algorithm and total solution time increases. If $\bar{\eta}$ is selected larger than an optimum value, less number of elements are captured and accuracy of solution decreases.

Dynamic Substructuring Alagorithm

Approximation errors caused by the heat flux jump at the solidification front and discretization errors due to large element size can be decreased to allowable levels by mesh refinement around the solidification front. Refining all elements can be a remedy for this problem but its computational cost will be very high. In this study, only the elements having errors larger than the permissible error percentage $\bar{\eta}$ are refined to reduce the computational cost of problem. This refinement is performed by preparing a substructure and the original mesh of the global model is not affected by the mesh refinement. The original global equations are augmented with the substructure equations and this process is repeated at each analysis step. If the error level reduces to below the threshold value for certain elements at an analysis step, associated refined elements are removed in the substructure. Thus, the substructure is very effective for accurate numerical solutions.

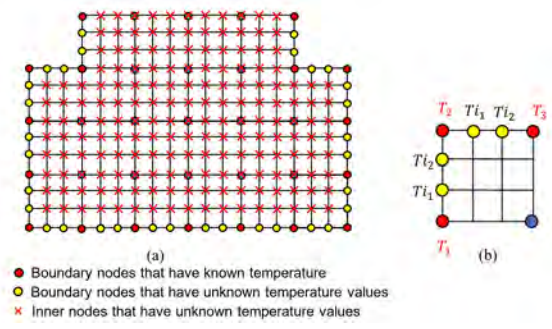

Figure 7. (a) Substructure and (b) interpolation of boundary temperatures..

Figures 6 and 7 show a representation of substructuring method. The global model with a coarse mesh is shown in Figure 6. At each solution step, errors of elements are calculated with the methodology given in Section 3.3. Elements having errors higher than permissible error percentage $\bar{\eta}$ are shown with red dotted texture in Figure 6. Nodes of these elements are shown with blue and green dots. Green dots indicate the nodes of elements having errors higher than permissible error percentage $\bar{\eta}$ on model boundary. Temperature values at blue and green nodes contain errors due to the coarse mesh and heat flux jump exists at the solidification front. Temperature values of black nodes and red nodes are in the allowable limits. Thus, red nodes which are neighboring nodes to elements having errors higher than permissible error percentage $\bar{\eta}$ are used as the boundary nodes of substructure and temperature values of these red nodes are applied to the substructure as boundary conditions. Our algorithm determines the elements having errors higher than permissible error percentage $\bar{\eta}$ and neighboring nodes to these elements at every analysis step.

The substructure given in Figure 7 (a) is created by the substructuring algoritm developed in this study. All codes are developed using Matlab environment. Number of element division in mesh refinement is selected by the user. In this example, each element is divided by 3x3 and 9 sub-elements are created inside each global element if that element has an error higher than permissible error percentage $\bar{\eta}$. Red nodes and yellow nodes represent the boundary nodes. The boundary conditions of substructure are applied to these nodes. Temperature values of red nodes are obtained from the global model. Temperature values of yellow nodes are determined by linear interpolation. Figure 7 (b) shows an element which has two shared edges with a substructure boundary. The temperatures T_1, T_2 and T_3 are obtained from the global model. Firstly, the algoritm determines the red nodes which are around yellow nodes. For example, yellow nodes on vertical edge are located between the red nodes having the temperatures of T_1 and T_2 , and yellow nodes on horizontal edge are located between

the red nodes having the temperatures of T_2 and T_3. Then, the algoritm calculates the temperatures Ti_1 and Ti_2 of the nodes located on vertical and horizontal edges with the following interpolation equations

$$Ti_i = \min(T_1, T_2) + \left[\frac{abs(T_1 - T_2)}{n}\right] * i \tag{42}$$

$$Ti_i = \min(T_2, T_3) + \left[\frac{abs(T_1 - T_2)}{n}\right] * i \quad i = 1, 2 \tag{43}$$

where n is the number of divisions on the corresponding edge of the element.

Temperature initial conditions are to be applied to the substructure nodes except the nodes lying on the boundaries before the solution process. At the first analysis step, global model initial temperatures are applied to the nodes and problem is solved. At the following steps, the algoritm checks the substructure of previous step. If there are common global elements at succeeding steps, calculated common nodal temperatures of the previous step are applied as the initial temperature to the common nodes of the current step.

Figure 9 (a) shows the global model and Figure 9 (b) shows the augmented model at the analysis step #1. Elements having errors higher than permissible error percentage $\bar{\eta}$

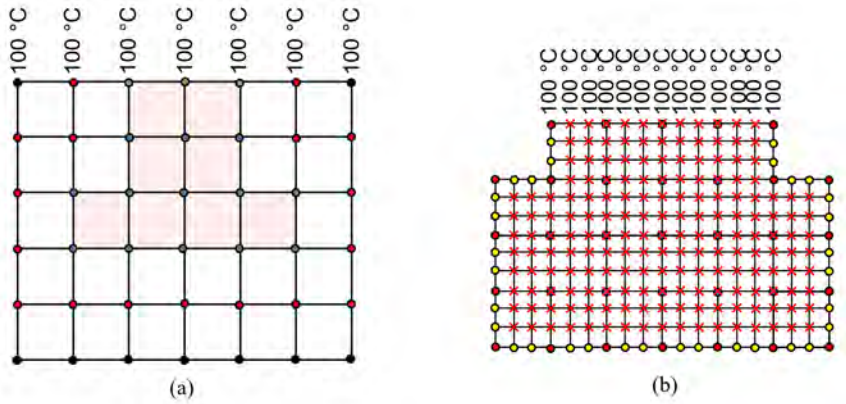

Figure 8. (a) Global model with boundary conditions and (b) substructure with global model boundary conditions.

After obtaining boundary conditions of the substructure, the capacity and stiffness matrices and heat vectors of the substructure are calculated. Following, the global model equations are augmented with substructure equations which is explained in Section 3.5.

The red cross symbols in Figure 7 (a) indicate the nodes having unknown temperature values. Temperatures of inner nodes are calculated by the generalized trapezoidal method at each analysis step. During the solution process, the location of solidification front is determined at each analysis step and heat convection is applied to elements which are neighbour to the solidification front.

Another important issue in the substructuring emerge when the substructure boundary nodes coincide with the global model boundary nodes. When such a condition occurs, the algoritm applies the global model boundary conditions to the coincident nodes of the substructure. Such a case is shown in Figure 8 where 100 °C temperature is applied to the top nodes of global model as boundary conditions. When the substructure is created, the same boundary condition is applied to the coincident nodes of the substructure.

and substructure boundary are determined with the global model solution (i.e., see Figure 9 (a)) at the end of analysis step #1. Then, the substructure is generated to reduce the error levels by following the method described above. Initial temperature of the global model is applied to internal nodes of the substructure as initial conditions because this is the first step of analyses. After the substructure is generated, the global model is augmented with it as shown in Figure 9 (b). This augmented model is solved in analysis step #1 again and unknown substructure temperature values shown by blue nodes are obtained.

After solving the first analysis step, the program increases the time step number and obtains the global model solution; then, elements having errors higher than permissible error percentage $\bar{\eta}$ and substructure boundary for the second analysis step are calculated (e.g., see Figure 10 (a)). Then, new substructure for the second analysis step is prepared. The method to obtain the initial temperatures of substructure is different for step #1 and for other steps. The program checks the existence of common elements having errors higher than permissible error percentage $\bar{\eta}$ between the current and previous analysis steps. If such elements are found, then the program automatically maps

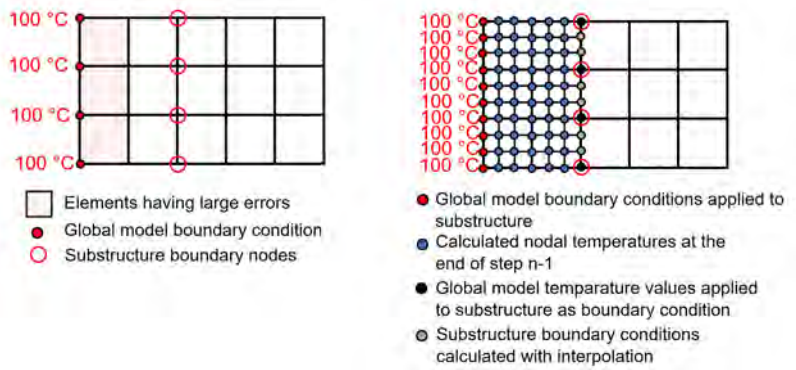

Figure 9. (a) Global model and elements having large errors at the end of step #1. (b) Substructure and calculated temperatures at the end of step #1.

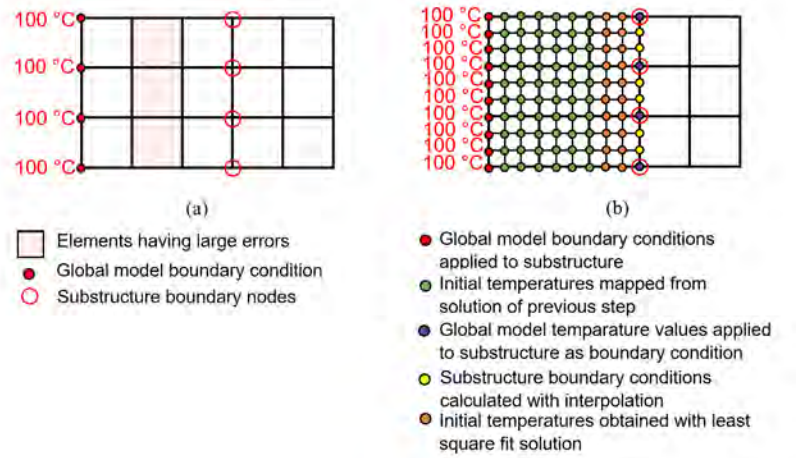

Figure 10. (a) Global model and elements having large errors at the end of step #2. (b) Substructure and initial temperatures at the beginning of step #2..

the temperatures calculated by the previous augmented model onto the common nodes of the current substructure. Figure 10 (b) shows the substructure at analysis step #2. It is seen that the green nodes in Figure 10 (b) are the common nodes with blue, black and grey nodes of the substructure in Figure 9 (b) at analysis step #1. Thus, temperature values of blue, black and grey nodes are mapped onto green nodes of the new substructure at the beginning of anaysis step #2.

Initial temperatures of orange nodes are also to be determined before the solution of augmented equation system. Temperature values of green nodes, purple nodes and yellow nodes in Figure 10 (b) are known. Subsequently, initial temperature values of orange nodes can be found by interpolation with the least square fit method given by

$$\{T\} = [P]\{\alpha\} \tag{46}$$

$$\{\alpha\} = [P]^{-1}\{T\} \tag{47}$$

where $T(x,y)$ is a polynominal curve fitting function for the temperature, the coefficients α_i are unknown, and x_i and y_i are the nodal coordinates. Equation (45) shows the matrix equation of polynominal temperature curve fitting function. The unknown coefficients α_i can be determined using Equation (47) and known temperature values which are those of the neighbouring nodes to orange nodes in Figure 10 (b) . After finding the coefficients α_i, unknown temperature values of orange nodes are calculated using Equation (44).

$$T(x,y) = \alpha_0 + \alpha_1 x + \alpha_2 y + \alpha_3 x^2 + \alpha_4 xy + \alpha_5 y^2 + \alpha_6 x^3 + \alpha_7 x^2 y + \alpha_8 xy^2 + \alpha_9 y^3 \tag{44}$$

$$\begin{Bmatrix} T_1 \\ T_1 \\ \vdots \\ T_n \end{Bmatrix} = \begin{bmatrix} 1 & x_1 & y_1 & x_1^2 & x_1y_1 & y_1^2 & x_1^3 & x_1^2y_1 & x_1y_1^2 & y_1^3 \\ 1 & x_2 & y_2 & x_2^2 & x_2y_2 & y_2^2 & x_2^3 & x_2^2y_2 & x_2y_2^2 & y_2^3 \\ \vdots & \vdots & \vdots & \vdots & \vdots & \vdots & \vdots & \vdots & \vdots & \vdots \\ 1 & x_n & y_n & x_n^2 & x_ny_n & y_n^2 & x_n^3 & x_n^2y_n & x_ny_n^2 & y_n^3 \end{bmatrix} \begin{Bmatrix} \alpha_1 \\ \alpha_1 \\ \vdots \\ \alpha_n \end{Bmatrix} \tag{45}$$

Augmentation of Substructuring Equations

Semi-discrete FEM equations of the original global model for transient two phase solidification problem can be written in the following form

$$[C]\{\dot{T}(t)\}+([K_c]+[K_h])\{T(t)\}=\{R_h(t)\} \quad (48)$$

Semi-discrete FEM equations for the substructuring can be writen in a similar fashion as follows

$$[C]_{sub}\{\dot{T}_{sub}(t)\}+([K_c]_{sub}+[K_h]_{sub})\{T_{sub}(t)\}=\{R_{hsub}(t)\} \quad (49)$$

These two matrix equations can be augmented as follows:

$$\begin{bmatrix}[C] & [0]\\ -[G] & [C]_{sub}\end{bmatrix}\begin{Bmatrix}\{\dot{T}(t)\}\\ \{\dot{T}_{sub}(t)\}\end{Bmatrix}+\begin{bmatrix}[K_c]+[K_h] & [0]\\ -[G] & [K_c]_{sub}+[K_h]_{sub}\end{bmatrix}\begin{Bmatrix}\{T(t)\}\\ \{T_{sub}(t)\}\end{Bmatrix}=\begin{Bmatrix}\{R_h(t)\}\\ \{R_{hsub}(t)\}\end{Bmatrix} \quad (50)$$

where $[C]$ is the global model capacity matrix, $[C]_{sub}$ is the substructure capacity matrix, $\{\dot{T}(t)\}$ is the global model temperature derivative vector, $\{\dot{T}_{sub}(t)\}$ is the substructure temperature derivative vector, $[K_c]$ and $[K_h]$ are the global model stiffness matrices, $[K_c]_{sub}$ and $[K_h]_{sub}$ are the substructure stiffness matrices, $\{T(t)\}$ is the global model temperature vector, $\{T_{sub}(t)\}$ is the substructure temperature vector, $\{R_h(t)\}$ is the global heat vector, $\{R_{h_{sub}}(t)\}$ is the substructure heat vector and $[G]$ is the substructure boundary condition matrix. All matrices and vectors except $[G]$ in Equation (50) can be calculated with the formulas given in Section 3.2. The matrix $[G]$ is formed considering the substructure boundaries, corresponding global model nodes and element refinement of global model elements. How to construct the matrix $[G]$ is below described for a simple domain.

Figure 11 shows the global model, substructure and augmented model for a rectangular domain where the substructure is located between the global model nodes 6, 7, 10 and 11. Then, substructure nodes 1, 4, 13 and 16 are coincident with the global model nodes 6, 7, 10 and 11. Before creating the matrix $[G]$, its size should be determined, that depends on the global model DOF and substructure DOF. Number of rows of $[G]$ is equal to the substructure DOF (m) and number of columns of $[G]$ is equal to the global model DOF (n); then, the size of $[G]$ will be mxn. It is shown in Figure 11 that total global model DOF is 16 and total substructure DOF is 16; then, the size of $[G]$ is 16x16 for this domain.

Internal nodes of the substructure have no connection with the boundary and nodes of the global model. Hence, the rows of the matrix $[G]$ which match with the internal node numbers will be zero and subsequently all matrix components which are in the rows 6, 7, 10 and 11 are zero.

The rows of the matrix $[G]$ which match with the corner node numbers will also be zero except for the columns of global model node numbers coincident with the corresponding substructure node numbers that will be equal to unity. The substructure nodes 1, 4, 13 and 16 are coincident with the global model nodes 6, 7, 10 and 11; thus, the components $G(1,6)$, $G(4,7)$, $G(13,10)$, $G(16,11)$ are equal to 1.

The rows of the matrix $[G]$ which match with the mid node numbers on the boundary will be zero except for the columns of global model node numbers coincident with the corresponding substructure corner node numbers. The substructure nodes 2 and 3 are located between the global model corner nodes 6 and 7. Thus, the components $G(2,6)$, $G(2,7)$, $G(3,6)$, $G(3,7)$ are not equal to zero. The substructure nodes 8 and 12 are located between the global model corner nodes 7 and 11. Thus, the components $G(8,7)$, $G(8,11)$, $G(12,7)$, $G(12,11)$ are not equal to zero. The

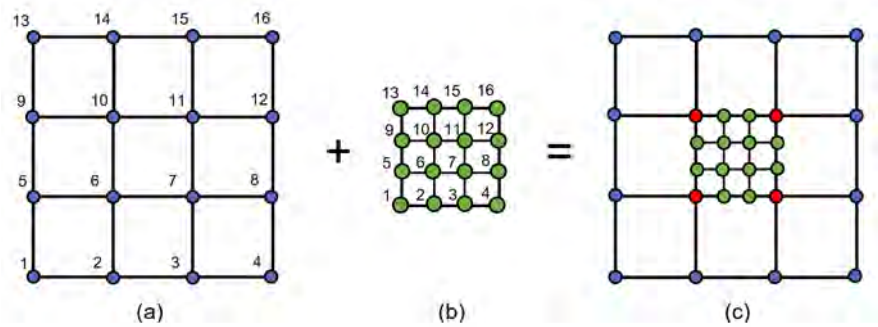

Figure 10. (a) Global model, (b) substructure and (c) augmented model.

substructure nodes 14 and 15 are located between the global model corner nodes 10 and 11. Thus, the components $G(14,10)$, $G(14,11)$, $G(15,10)$, $G(15,11)$ are not equal to zero. The substructure nodes 5 and 9 are located between the global model corner nodes 6 and 10. Thus, the components $G(5,6)$, $G(5,10)$, $G(9,6)$, $G(9,10)$ are not equal to zero. The values of non-zero components of $[G]$ are found with the following formula which is an interpolation equation

$$G(m,n)=1-\frac{distance\ of\ sub\ model\ node\ m\ to\ global\ model\ node\ n}{distance\ between\ global\ model\ corner\ nodes} \tag{51}$$

For example, the substructure node 2 is located between the global model corner nodes 6 and 7. Following, the components $G(2,6)$ and $G(2,7)$ can be calculated as follows

$$G(2,6)=1-\frac{distance\ of\ sub\ model\ node\ 2\ to\ global\ model\ node\ 6}{distance\ between\ global\ model\ corner\ nodes\ 6\ and\ 7}=1-\frac{1}{3}=\frac{2}{3} \tag{52}$$

$$G(2,7)=1-\frac{distance\ of\ sub\ model\ node\ 2\ to\ global\ model\ node\ 7}{distance\ between\ global\ model\ corner\ nodes\ 6\ and\ 7}=1-\frac{2}{3}=\frac{1}{3} \tag{53}$$

Then, the matrix $[G]$ for the sample domain shown in Figure 11 is given by

$$[G]=\begin{bmatrix}
0&0&0&0&0&1&0&0&0&0&0&0&0&0&0&0\\
0&0&0&0&0&2/3&1/3&0&0&0&0&0&0&0&0&\\
0&0&0&0&0&1/3&2/3&0&0&0&0&0&0&0&0&0\\
0&0&0&0&0&0&1&0&0&0&0&0&0&0&0&0\\
0&0&0&0&0&2/3&0&0&0&1/3&0&0&0&0&0&0\\
0&0&0&0&0&0&0&0&0&0&0&0&0&0&0&0\\
0&0&0&0&0&0&0&0&0&0&0&0&0&0&0&0\\
0&0&0&0&0&0&2/3&0&0&0&1/3&0&0&0&0&0\\
0&0&0&0&0&1/3&0&0&0&2/3&0&0&0&0&0&0\\
0&0&0&0&0&0&0&0&0&0&0&0&0&0&0&0\\
0&0&0&0&0&0&0&0&0&0&0&0&0&0&0&0\\
0&0&0&0&0&0&1/3&0&0&0&2/3&0&0&0&0&0\\
0&0&0&0&0&0&0&0&0&1&0&0&0&0&0&0\\
0&0&0&0&0&0&0&0&0&2/3&1/3&0&0&0&0&0\\
0&0&0&0&0&0&0&0&0&1/3&2/3&0&0&0&0&0\\
0&0&0&0&0&0&0&0&0&0&1&0&0&0&0&0
\end{bmatrix} \tag{54}$$

Numerical Examples

In this section, two phase solidification problem of lead is solved in 2D using the proposed approach. Firstly, it is solved using a fine mesh and a coarse mesh to be used for comparisons. Then, dynamic substructuring technique is applied to the coarse mesh along with the adaptive error estimation algorithm. All examples are solved with a developed Matlab code on a PC having an Intel Core i7-4820 @ 3.70 GHz CPU, 16 GB RAM and Windows 8 operating system. Only one core of the CPU is utilized for the computations.

The computational domain has the length of 0.5 m and width of 0.5 m. Initial temperature of liquid lead is 337°C (T_i) and computational domain is cooled by applying 300°C temperature (T_b) to the left and bottom edges of the domain. Other edges of the domain are adiabatic (e.g., see Figure 12). Temperature variations of thermal conductivity, specific heat and density of the material are given by Equations (4) to (9), respectively. These properties of the lead material are calculated depending on the element average temperature at every analysis step.

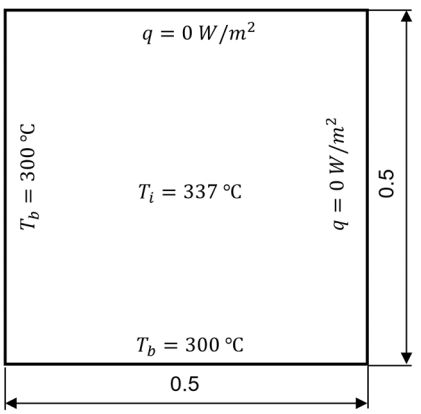

Figure 12. Geometry of 2-D computational domain with the boundary and initial conditions.

Total solution time is chosen as 2350 seconds in real time, the solution is completed at 2350 steps and constant time step of 1 second is used in numerical solutions. Figure 13 shows the temperature distribution in the coarse mesh (having the element division of 25x25) at the last analysis step and Figure 14 shows the temperature distribution in the fine mesh (having the element division of 75x75) at the last analysis step. The crust temperature of lead alloy is 320 °C and melting temperature is 327°C. Therefore, the green contours in both figures show the location of mushy zone and the boundary between the green contour and cyan contour shows the location of solidification front. If the solutions are examined, it is observed in the coarse mesh solution that almost all of the liquid metal is solidified at the time instant of 2350 seconds and the position of solidification front is not very clear. However, when the fine mesh is used, it is observed that the mushy zone is larger and position of solidification front is very clear.

Following, dynamic substructuring approach proposed in this paper is applied to the same solidification problem having the coarse mesh shown in Figure 13. Figures 15 (a) to (g) show the temperature distributions at different time instants during solidification. Each element is divided into 9 elements when generating the substructure, the error threshold $\bar{\eta}$ is selected to be 1.5 %, the density ρ is assumed to be constant for the solid phase and the coefficient of convection h is assumed to be constant at the solid-liquid interface whose value is obtained from Bratu, et al. [31] as 1600 $W/(m^2°C)$.

Note that total solution time of the fine mesh is 11,773 seconds. When dynamic substructuring approach based on adaptive error estimation is used with 1.5 % permissible error percentage $\bar{\eta}$, total solution time reduced to 9,141 s. The reduction in CPU times will be even further if the element matrices of the original global model are constant. Besides, the proposed dynamic substructuring approach requires less memory than the conventional fine mesh analysis. Moreover, the locations of solidification front and mushy zone are found very precisely by the proposed approach.

Temperature difference percentage between dynamic substructure results and fine mesh results at the time instant of 2350 seconds is given in Figure 16 in which it is observed that the maximum temperature difference percentage is 0.29 %. This accuracy level shows that the error estimation algoritm based dynamic substructuring technique works very well and this technique provides very good accuracy by decreasing the total CPU time.

The same problem is solved using different permissible error values $\bar{\eta}$ to compare the effect of this parameter on the accuracy and CPU times. To this end, selected $\bar{\eta}$ values are

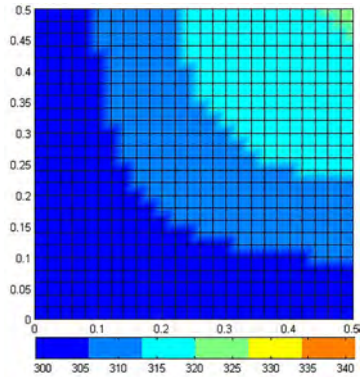

Figure 13. Coarse mesh temperature distribution at t=2350 seconds.

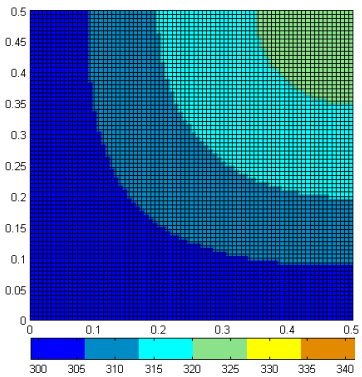

Figure 14. Fine mesh temperature distribution at t=2350 seconds.

1 %, 1.5 %, 2 % and 3 % and the corresponding CPU times are found as 13,913 sec., 9,141 sec., 7,312 sec., 5,813 sec., respectively. Figure 17 shows the temperature distributions as $\bar{\eta}$ changes at the time instant of 2350 sec. Note that the locations of solidification front and mushy zone can be found very precisely by the proposed approach for all values of $\bar{\eta}$. It is observed that permissible error percentage $\bar{\eta}$ value of 3 % yields acceptable results while the associated CPU time is almost half of that of the fine mesh.

DISCUSSION

Under the light of numerical results, it is observed that dynamic substructuring technique is more advantageous when compared with the other methods such as moving mesh method, adaptive remeshing method, XFEM method, GFEM method and meshless methods whose main drawbacks are listed below.

In moving mesh method, firstly solid liquid interface is tracked explicitly and then the mesh is deformed dynamically to align the element edges with the solidification front. Main advantage of this method is that number of nodes and elements are fixed; however, element sizes in the deformed region become larger during rearrangment of the nodes and this condition causes high element aspect ratios. New elements need to be created to decrease the element

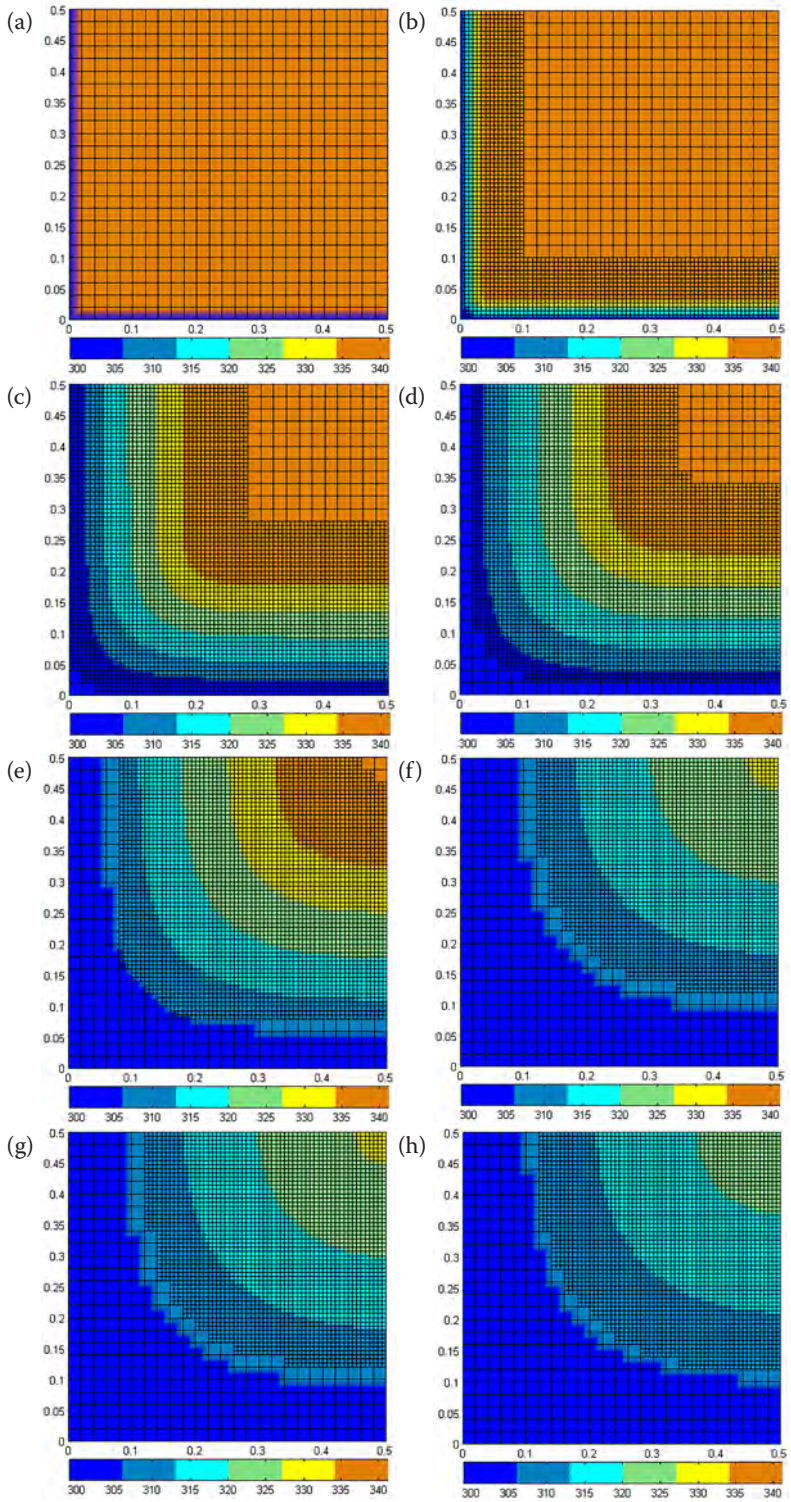

Figure 15. Temperature distributions found by dynamic substructuring approach at time instants of (a) 1 sec., (b) 10 sec., (c) 300 sec., (d) 500 sec., (e) 1000 sec., (f) 1500 sec., (g) 2000 sec., (h) 2350 sec.

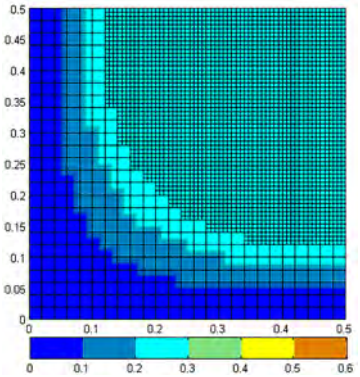

Figure 16. Temperature difference percentage (ΔT %) between dynamic substructure results and fine mesh results at the time instant of 2350 sec.

aspect ratios. During this process, global matrices are to be updated at each analysis step due to rearrangment of the node coordinates and also element sizes are to be checked at each analysis step, e.g., see [1], [2], [3], [5], [11], [12], [26]. In addition, this method is not suitable for alloys with finite freezing range and it is applicable to simple geometry and interface shapes only; appearing or disappearing phases and multiple interfaces cannot be handled by this method [16].

In adaptive remeshing method, the location of solidification front is determined with error estimators or interface tracking methods. After that the whole global domain is remeshed to align the element edges with the solidification front and a fine mesh is used at interface. During remeshing, old mesh data are to be mapped onto new mesh data for which special algorithms are required to obtain accurate solutions. In this method, global matrices are to be updated due to remeshing operation and also element numbers increase drastically because the whole domain is remeshed, e.g., see [10], [13], [18], [20], [24], [43].

The GFEM and XFEM determine the location of solidification front with interface tracking methods such as level set methods. After finding the location of solidification front, imaginary nodes are placed on interface and elements are split with these nodes. Mesh of the domain is not affected during these methods but global matrices are to be updated at each step due to imaginary nodes and extra DOF, e.g., see [15], [16], [17], [21], [27], [45].

Meshless methods determine the location of solidification front with interface tracking methods and then place points on interface to obtain accurate solutions at phase change location. Global matrices are to be updated at each analysis step due to the extra points placed on the solidification interface, e.g., see [22], [30].

All of these methods mentioned above focus on aligning the nodes to the solidification front except for error estimator based adaptive remeshing methods. Thus, very

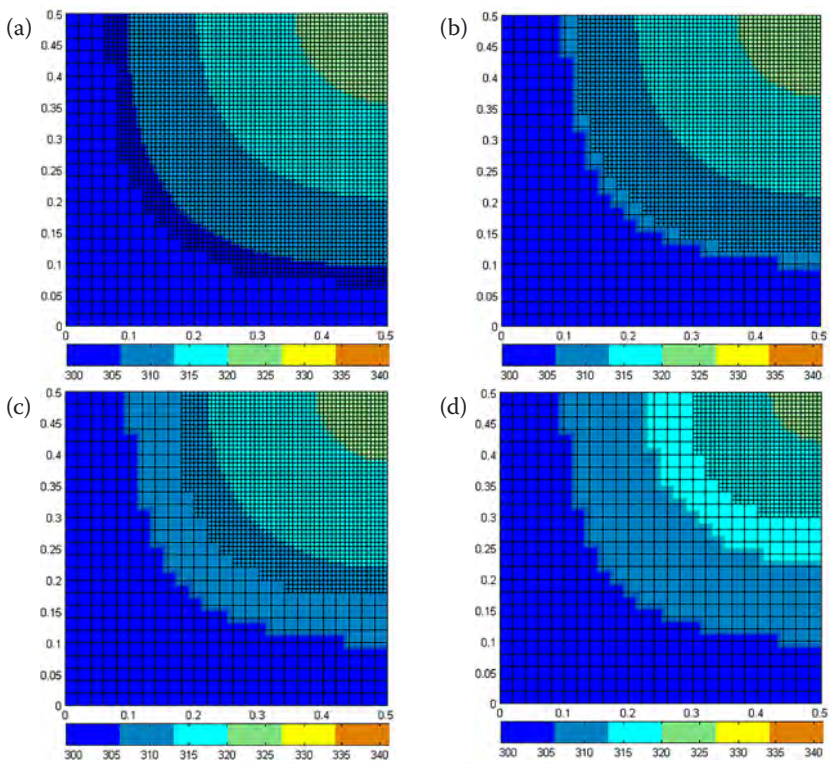

Figure 17. Temperature distributions depending on $\bar{\eta}$: (a) $\bar{\eta}$=1 %, (b) $\bar{\eta}$=1.5 %, (c) $\bar{\eta}$=2 %, (d) $\bar{\eta}$=3 %

accurate solutions around the solidification front can be obtained with these methods. However, all of these methods ignore mushy zone except for error estimator based adaptive remeshing method. One of the advantages of dynamic substructuring method arise at this point; error estimation algorithm automatically captures the solidification front and mushy zone due to high error ratios of these elements and this condition causes both the solidification front and mushy zone to be refined automatically and to get more accurate results at these zones.

On the other hand, error estimator based adaptive remeshing methods can also capture the mushy zone but their disadvantage is high CPU times because the whole domain is remeshed with refined elements in these methods. When the size of model geometry increases, the solution time also increases drastically. Another disadvantage of these methods compared with dynamic substructuring method is mesh compatibility. In these alternative methods during remeshing, old mesh data needs to be mapped onto new mesh data and special algorithms are required to obtain accurate solutions. If the local remeshing is applied to the domain, it is hard to connect the new generated refined elements to the coarse mesh of domain. This phenomenon does not occur at dynamic substructuring approach because the substructure is created explicitly and independent from the original global model. Thus, substructure domain elements can be refined freely.

There is no clear CPU time comparisions of alternative methods in literature given above except for meshless methods. Meshless methods are slower than classical FEM per reference [30]. But, when the alternative methods are considered, node numbers and element numbers of the global domain are increased to improve the accuracy and this condition causes the global matrices to be updated at each analysis step. When the computation domain gets larger, solution time will increase drastically. Another advantage of dynamic substructuring arises at this point. The original global model is not affected when dynamic substructuring approach is used. The substructure which is a smaller portion of the global model is prepared at each step. Thus, CPU times for substructure matrix preparation will be less time consuming when compared with alternative methods.

CONCLUSIONS

We presented a dynamic substructuring technique based on adaptive error estimation applied to solution of two phase solidification problems. The key feature of this method is the construction of a substructure using a locally refined mesh in the computational domain by the virtue of error estimates and augmentation of the governing equations by the equations of this substructure. One of the advantages of using such a dynamic substructuring technique is that high accuracy in solutions can be achieved while determining the location of solidification front and mushy zone with coarse meshes and calculating temperature distribution of computational domain. Another advantage of the proposed method is to reduce the CPU times significantly while obtaining very accurate results. The reduction in CPU times will be even further if the element matrices of the original global model are constant. To this end, the parameter of permissible error percentage $\bar{\eta}$ should be selected appropriately.

The proposed technique is applied to simulate the solidification of lead in a 2-dimensional domain. The same problem is also solved with the fine and coarse meshes for comparisons. Numerical results show that the error estimator accurately captures the numerical errors with the coarse meshes and the same accuracy of fine mesh can be achieved with the dynamic substructuring technique.

In comparison with the numerical results of fine mesh, dynamic substructuring technique has the advantage of fast computation as well as obtaining the same accuracy when solving the solidification problems, in particular in detection of solidification front and mushy zone. It is concluded that the proposed dynamic substructuring method based on adaptive error estimation is a potential numerical analysis tool for the analysis of solidification problems.

REFERENCES

1. O'Neill K and Lynch DR. A finite element solution for freezing problems, using a continuously deforming coordinate system. Numerical Methods in Heat Transfer. (1981) 215–231.

2. Lynch DR and Sullivan JM. Heat conversation in deforming element change simulation. Journal of Computational Physics. 57 (1985) 303–317.
3. Kuang Z and Atluri S. Temperature fields due to a moving heat source: A moving mesh finite element analysis. J. Appl. Mech. 52(2) (1985) 274-280.
4. Tamma K and Saw K. Hierarchical p–version finite elements and adaptive a posteriori computational formulations for two–dimensional thermal analysis. Comp. Struct. 32(5) (1989) 1183-1194.
5. Zabaras N, Ruan Y, Richmond O. Front tracking thermomechanical model for hypoelastic–viscoplastic behaviour in a solidifying body. Computer Methods in Applied Mechanics and Engineering. 81 (1990) 333–364.
6. Ro ST. Recent progress in heat transfer during melting and solidification processes. Transport Phenomena in Heat and Mass Transfer. (1992) 587–604.
7. Ghosh S and Moorthy S. An arbitrary Lagrangian–Eulerian finite element model for heat transfer analysis of solidification processes. Numer. Heat Trans. Part B. 23 (1993) 327-350.
8. Wang SL, Sekerka RF, Wheeler AA, Murray BT, Coriell SR, Braun RJ and McFadden GB. Thermodynamically–consistent phase–field models for solidification. Physica D 69 (1993) 189–200.
9. Gandin ChA and Rappaz M. A coupled finite element cellular automaton model for the prediction of dendritic grain structures in solidification processes. Acta Metall. Mater. 42 (1994) 2233–2246.
10. Franca AS and Haghigi K. Adaptive finite element analysis of transient thermal problems. Numerical Heat Transfer Part B. 26 (1994) 273–292.
11. Juric D and Tryggvason G. A front–tracking method for dendritic solidification. Journal of Computational Physics. 123 (1996) 127–148.
12. Chen Y, Im Y–T, Yoo J. Finite element analysis of solidification of aluminum with natural convection. Journal of Materials Processing Technology 52 (1995) 592–609.
13. Provatas N, Goldenfeld N and Dantzig J. Adaptive mesh refinement computation of solidification microstructures using dynamic data structures. Journal of Computational Physics. 148 (1999) 265–290.
14. Lewis RW and Ravindran K. Finite element simulation of metal casting. International Journal for Numerical Methods in Engineering. 47 (2000) 29–59.
15. Merle R and Dolbow J. Solving thermal and phase change problems with the extended finite element method. Computational Mechanics 28 (2002) 339–350.
16. Chessa J, Smolinski P and Belytschko T. The extended finite element method (xfem) for solidification problems. International Journal for Numerical Methods in Engineering. 53 (2002) 1959–1977.
17. Ji H, Chopp D and Dolbow JE. A hybrid extended finite element/level set method for modeling phase transformations. International Journal For Numerical Methods in Engineering. 54 (2002) 1209–1233.
18. Zhao P, Venere M, Heinrich JC, Poirier DR. Modeling dendritic growth of a binary alloy. Journal of Computational Physics. 188 (2003) 434–461.
19. Zhang XR and Xu X. Finite element analysis of pulsed laser bending: the effect of melting and solidification. Journal of Applied Mechanics 71 (2004) 321–326.
20. Takaki T, Fukuoka T, Tomita Y. Directional solidification of a binary alloy using adaptive finite element method. Journal of Crystal Growth. 283 (2005) 263–278.
21. Zabaras N, Ganapathysubramanian B, Tan L. Modelling dendritic solidification with melt convection using the extended finite element method. Journal of Computational Physics. 218 (2006) 200–227.
22. Zhang L, Shen H–F, Rong Y, Huang T–Y. Numerical simulation on solidification and thermal stress of continuous casting billet in mold based on meshless methods. Materials and Science Engineering. A466 (2007) 71–78.
23. Wang H, Li R, Tang T. Efficient computation of dendritic growth with r–adaptive finite element methods. Journal of Computational Physics. 227 (2008) 5984–6000.
24. Hu X, Li R and Tang T. A multi–mesh adaptive finite element approximation to phase field models. Communications in Computational Physics. 5 (2009) 1012–1029.
25. Lee S and Sundararaghavan V. Multi–scale homogenization of moving ınterface problems with flux jumps: Application to solidification. Comput Mech. 44 (2009) 297–307.
26. Bo Li and John Shopple. An Interface–Fitted Finite Element Level Set Method With Application to Solidification and Solvation. Commun. Comput. Phys. 10 (2011) 32–56.
27. P. O'Hara CA and Eason DT. Transient analysis of sharp thermal gradients using coarse finite element meshes. Comput. Methods Appl. Mech. Engrg. 200 (2011) 812–829.
28. Chen M, Hu X–D, Ju D–Y, Zhao H–Y. The microstructure prediction of magnesium alloy crystal growth in directional solidification. Computational Materials Science. 79 (2013) 684–690.
29. Chen S, Guillemot G and Gandin C–A. 3D coupled cellular automaton (ca) – finite element (fe) modeling for solidification grain structures in gas tungsten arc welding (GTAW). ISIJ International. 54 (2014) 401–407.
30. Ghoneim A. A meshfree ınterface–finite element method for modelling ısothermal solutal melting and solidification in binary systems. Finite Elements in Analysis and Design. 95 (2015) 20–41.
31. Bratu V, Mortici C, Oros C, Ghiban N. Mathematical model of solidification process in steel continuous casting into account the convective heat transfer at liquid–solid ınterface. Computational Materials Science. 94 (2014) 2–7.
32. Skrzypczak T, Wegrzyn–Skrzypczak E. Mathematical and numarical model of solidification process of pure metals. International Journal of Heat and Mass Transfer. 55 (2012) 4276–4284.
33. Ho CY, Powell RW andLiley PE. Thermal conductivity of the elements. J. Phys. Chem. Ref. Data 1 No. 2 (1972) 279–421.
34. Abu–Eishah SI, Haddad Y, Solieman A and Bajbouj A. A new correlation for the specific heat of metals, metal oxides and metal fluorides as a function of temperature. Latin American Applied Research. 34 (2004) 257–265.
35. Sobolev V. Database of thermophysical properties of liquid metal coolants for GEN–IV. Scientific Report of the Belgian Nuclear Research Centre. (2011).
36. Nikishkov G. Programming finite elements in java. Springer–Verlag, London. (2010).

37. Hughes TJR. The finite element method linear static and dynamic finite element analysis. Prentice–Hall. (1987).
38. Liu GR and Quek SS. The finite element method a practical course. Butterworth–Heinemann. (2003).
39. Cook RD. Finite element modeling for stress analysis, John Wiley and Sons. (1995). Rudolph Szilard. Theories and Applications of Plate Analysis. John Wiley and Sons. (2004).
40. Zienkiewicz OC and Zhu JZ. A simple error estimator and adaptive procedure for practical engineering analysis. International Journal For Numerical Methods in Engineering. 24 (1987) 337–357.Thomas J. R. Hughes. The Finite Element Method Linear Static and Dynamic Finite Element analysis, Prentice–Hall, 1987.
41. Zienkiewicz OC, Taylor RL and Zhu JZ. The finite element method: its basis and fundamentals, seventh ed. Butterworth–Heinemann is an imprint of Elsevier. (2013).
42. Rabizadeh E, Bagherzadeh AS, Rabczuk T. Adaptive thermo–mechanical finite element formulation based on goal–oriented error estimation. Computational Materials Science. 102 (2015) 27–44.
43. Khoei AR, Gharehbaghi SA. Three–dimensional data transfer operators in large plasticity deformations using modified–spr technique. Applied Mathematical Modelling. 33 (2009) 3269–3285.
44. Gonzales–Estrada OA, Rodenas JJ, Bordas SPA, Nadal E, Kerfriden P, Fuenmayor FJ. Locally equilibrated stress recovery for goal oriented error estimation in the extended finite element method. Computers and Structures. 152 (2015) 1–10.

Hittite Journal of Science and Engineering, 2015, 2 (2) 145-150
ISSN NUMBER: 2149-2123
DOI: 10.17350/HJSE19030000018

Energy Analysis of A Building Based on Outdoor Air Temperature and Insulation Thickness

Burcin Tunay[1] and Ali Kilicarslan[2]
[1] Corum Municipality, Corum, TURKEY
[2] Hitit University, Department of Mechanical Engineering, Corum-TURKEY

ABSTRACT

The thermal performance of buildings is of great importance to the world because we have limited sources of fossil fuels. Thermal performance should be investigated with respect to parameters such as outdoor air temperature, insulation thickness, building materials, types of combustor and fuel. In this study, the effects of the outdoor air temperature and insulation thickness on the total radiator length, the annual fuel consumption and CO_2 emission were investigated for a three floor building, fueled by natural gas, located in Corum, Turkey. In order to do that, a computer code was developed by using of EES (Engineering Equation Solver) which is commonly used in the analysis of thermal systems.

The outside air temperature and the insulation thickness were varied from -15 to 4°C and 2 to 18 cm, respectively. It was observed that the total length of the radiator and the annual fuel consumption and CO_2 emission decreased with the increase of outdoor air temperature and insulation thickness. As the outside air temperature was varied, the total radiator length, the annual fuel consumption and CO_2 emission decreased by 33%, 30% and 30%, respectively. Increasing the amount of the insulation thickness resulted in an approximate decrease of 49% in the total radiator length, the annual fuel consumption and CO_2 emission.

Key Words: Heating; Outdoor Air Temperature; Insulation Thickness; CO_2 Emission.

Article History:
Received: 2015/11/09
Accepted: 2015/11/27
Online: 2015/12/30

***Correspondence to**: Ali Kilicarslan, Hitit University, Faculty of Engineering, Department of Mechanical Engineering, Corum, Turkey*
Tel: +90 (364) 227-4533 (1236)
Fax: +90 (364) 227-4535
E-Mail: alikilicarslan@gmail.com

NOMENCLATURE

a	Air leakage coefficient, m^3/mh
A	Heat transfer area, m^2
B_y	Fuel consumption per year, m^3/year
FSEG	CO_2 emission conversion factor based on the type of fuel, kg equivalent of CO_2/kWh
H	Building coefficient, Wh /m^3K
H_u	Lower heating value of fuel, kj/m^3
L	Length of opening side of window or door, m
R	Room coefficient
$SEGM_y$	Annual amount of CO_2 emission, kg equivalent of CO_2
Q_T	Total heat loss, W
Q_{inc}	Increased heat loss from building elements, W
Q_{inf}	Infiltration heat loss, W
Q_0	Heat loss from building elements, W
T	Temperature, °C
U	Heat transfer coefficient, W/m^2 K
Z_d	Working hours per day, h/day
Z_e	Infiltration coefficient
Z_y	Working days per year, day/year
Z_D	Combined incremental coefficient
Z_H	Floor incremental coefficient
Z_W	Direction incremental coefficient

Greek Symbols

η	efficiency

Subscripts

b	boiler	f	floor
d	door	o	outer
r	roof	w	window

INTRODUCTION

The consumption of underground resources, by means of the industrial revolution, rapid urbanization and population growth, have detrimental effect on the environment as the greenhouse gases. As a result, theoretical and experimental studies related to the energy saving and the usage of alternative energy sources such as solar, wind, geothermal, etc. have started to spread from Europe to the rest of the world.

Noteworthy amount of CO_2 emission is caused by the residential and commercial heating systems. Therefore, energy saving of buildings is currently one of the important issues. The studies related to the energy performance of the buildings in the literature are generally based on the design variables such as building shape, insulation level and materials, construction materials, height of floor, windows type, area, CO_2 emission, type of heating systems, type of fuel and application of renewable energy sources to the building[1].

Most of the studies in the literature are based on determining the optimum insulation thickness and the type of insulation. Natural gas and polystyrene were used as a fuel and insulation material, respectively, the thicknesses of insulation materials for outer walls were observed by means of "degree-day method". It was found that insulation thicknesses of the outer walls of the building in Turkey range from 2.8 to 9.6 cm [2]. In order to increase the thermal performance of the buildings, the insulation material must be mounted in the shape of a bundle. Detailed thermal energy and economic analyses are required for selecting an optimum thickness of insulation material. The optimum insulation thicknesses were calculated for three different walls in Athens by using hourly weather data and it was found that the optimum insulation thickness ranges from 7.1 to 10.1 cm for these walls [3]. It was pointed out that the window-to-floor area ratio, type and thickness of insulation material are very important from an energy point of view. A computer code was developed based on TS (Turkish standard) 825. By means of this code, the graphics for "fourth climatic zone of Turkey" were formed for selecting optimum insulation thickness with respect to the window-to-floor area ratio, type and thickness of the material. It was shown that the insulation thickness increases as the window-to-floor area ratio increases [4]. The effect of insulation thickness on CO_2 emission was investigated by using styropor as an insulation material and fuel oil as fuel. In a study based on degree-day method was carried out in Erzurum, that is one of the coldest cities of Turkey, it was found that CO_2 emission was reduced 27% by optimizing the insulation thickness. In a similar study in which expanded polystyrene and coal were used as an insulation material and fuel, the effect of optimum insulation thickness on the energy consumption and emissions of CO_2 and SO_2 was observed in Denizli, Turkey. It resulted that energy consumption and emissions of CO_2 and SO_2 were reduced 46.6% and 41.53%, respectively [5]. There are several studies in order to observe the insulation thickness and fuel type on energy saving and payback period [6-8]. A theoretical study aiming to investigate the insulation thickness and fuel type on the heating and cooling loads of outer walls, payback period and energy saving was carried out for four cities of Turkey, namely Mersin, Elazığ, Şanlıurfa, and Bitlis and for various types of fuel such as coal, natural gas, fuel-oil, liquefied petroleum gasoline and electricity. It was observed that the energy saving varied from 4.2\$/m^2 to 9.5\$/m^2 for optimum insulation thickness [6].

A few studies in the literature are related to the effect of outdoor air temperature on the building energy performance. A control algorithm was developed by Byun et al. for minimizing the heat transfer loss in building hot water distribution pipes as a function of outdoor air temperature and the variation of heat transfer was determined with respect to the outdoor air temperature, and the heat loss in the distribution lines was reduced by 11.5% [9]. Computer simulations were carried out in order to predict the heat and moisture transfer in the buildings with the experimentally measured values. Temperature and moisture content of the indoor air depending on the outdoor air temperature, relative humidity, wind speed and solar radiation were determined [10]. The effect of outdoor air conditions such as temperature and velocity on the building energy performance and fuel economy was investigated by means of various automatic control systems [11]. The capacity of an outdoor air controlled boiler of a central heating system was observed and it was resulted that the indoor air temperature increased beyond the comfort conditions as the boiler was controlled with respect to the outdoor air temperature. Later, the outer wall was insulated and the heating system was equipped with "on-off control system" and as a results of these changes, the fuel requirement of the system decreased [12].

In this study, for a three floor apartment, having nine dwellings, located in Corum, Turkey and using natural gas as a fuel, the effects of the outdoor air temperature and insulation thickness on the total radiator length, the annual fuel consumption and CO_2 emission were investigated by a computer code developed by means of EES [13] that is commonly used in the analysis of thermal systems.

MATERIAL AND METHOD

There are several steps to carry out this theoretical study. The first step is to calculate the heat transfer with respect to the selected building elements and construction

materials details of which are given in M.Sc. thesis [14]. The second step is to investigate the effects of outdoor air temperature and insulation thickness on the total radiator length, fuel consumption, CO_2 emission and annual heat requirement, and thereby contributing the energy saving in the buildings and investigating to decrease CO_2 emission caused by heating in the buildings. In order to perform the methodology in this work, a detailed computer code, consisting of all of the information about the thermal conductivities of building materials, solar data, fuel properties, physical properties of the building, etc., was developed by means of EES. EES has a library including thermo-physical properties of fluids and it has a capability of solving simultaneous equations, and forming graphics.

In this theoretical study, a three floor apartment, having nine dwellings and a base area of 264 m^2, located in Corum-Turkey, was selected. Natural gas is used as a fuel in the boiler. The following chapters will consist of the subsections of this work.

Heat Transfer Calculations

Heat loss calculations are performed with respect to Turkish Standards (TS) 2164. Total heat loss, Q_T, can be expressed by the following equation,

$$Q_T = Q_{inc} + Q_{inf} \quad (1)$$

Where;
Q_{inc} : Increased heat loss from building elements
Q_{inf} : Infiltration heat loss
Increased heat loss can be written as

$$Q_{inc} = Q_0(1+\%Z_D+\%Z_W+\%Z_H) \quad (2)$$

By using the following equation, nonincremental heat loss can be calculated

$$Q_0 = \Sigma AU\Delta T \quad (3)$$

$$\Sigma AU = U_oA_o + U_wA_w + U_dA_d + 0.8U_rA_r + 0.5U_fA_f \quad (4)$$

Infiltration heat loss, caused by the leakages in doors and windows, can be expressed as [15],

$$Q_{inf} = \Sigma\, aLRH\Delta T Z_e \quad (5)$$

Total Radiator Length

Total radiator length is determined with respect to the panel radiators. The manufacturer catalogs give the heating capacity of a radiator per unit length for different room temperatures.

As the total incremental heat loss is divided by the heating capacity of a radiator per unit length, the total radiator length is obtained. In this study, the tables used for determining the total radiator length are taken from the M.Sc. thesis [14].

Fuel consumption

Fuel consumption per year, B_y, can be calculated by the following equation [15].

$$By=3600\ (Q_TZ_dZ_y)/(2H_u\eta_b) \quad (6)$$

CO_2 Emission

Natural gas is used as a fuel in this study. The boiler efficiency and lower heating value of the natural gas are 0.9 and 34485 kj/kg, respectively. Flue gas emissions from a heating system consist of 85% CO_2, 15% other gases, namely, SO_2, CO, particulate matter (PM10 and PM2.5) and NO_x. But, CO_2 emission is only taken into consideration in the calculations. CO_2 emission can be expressed with respect to the type of fuel, lower heating value of fuel and fuel consumption [16],

$$SEGM_y=0{,}001163x\ B_y\ x\ H_u\ x\ FSEG \quad (7)$$

RESULTS AND DISCUSSIONS

Figure 1 shows the variation of total radiator length as a function of outdoor air temperature for insulated and uninsulated walls. As the outdoor air temperature increases, total radiator length decreases for both insulated and uninsulated walls. At the outdoor temperatures between -15°C and +4°C, total radiator length changes from 43.1 to 69 m for uninsulated wall and 32.4 to 46.2 m for insulated wall. The decrease in total radiator length is 60% for uninsulated wall and 48% for insulated wall. At the lower outdoor temperatures, the total radiator length is much more dominant as shown in Figure 1.

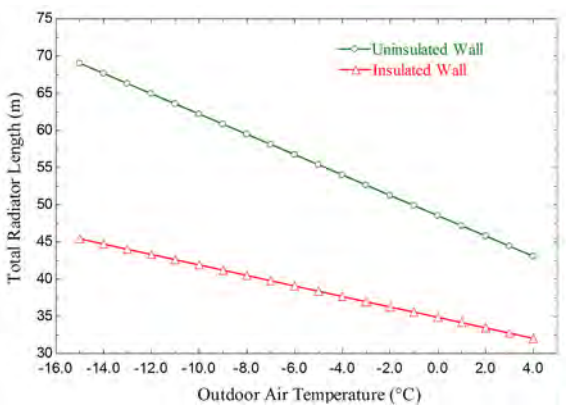

Figure 1. Total radiator length versus outdoor air temperature for insulated and uninsulated walls.

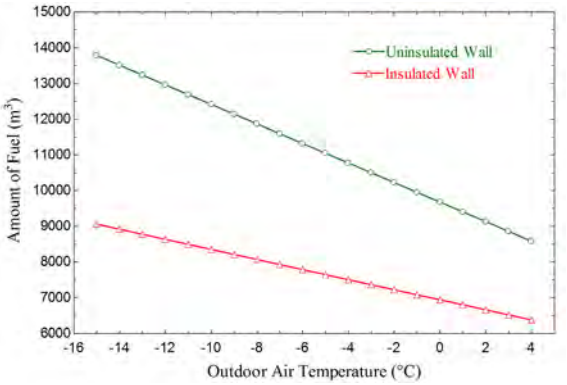

Figure 2. Fuel consumption versus outdoor air temperature for insulated and uninsulated walls.

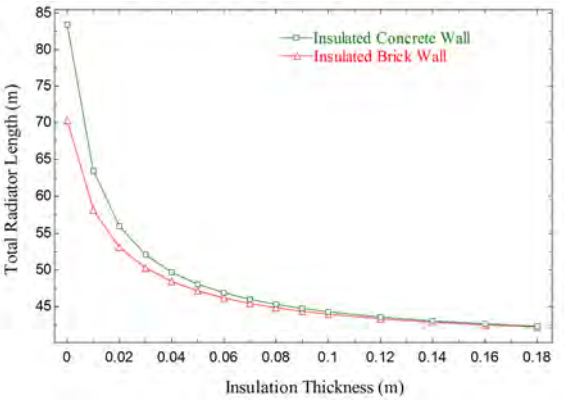

Figure 4. Total radiator length versus insulation thickness for insulated concrete and brick walls.

Figure 2 shows the variation of fuel consumption as a function of outdoor air temperature for insulated and uninsulated walls. Natural gas is used as a fuel and insulation thickness is 6 cm. The effect of outdoor temperature on the fuel consumption is similar to that on the total radiator length. It is clear from Figure 2 that the consumption fuel decreases as the outdoor temperature increases. The fuel consumption changes between 13786 m^3 and 8585 m^3 for uninsulated wall at the outdoor temperatures of -15°C and +4°C and the decrease in the fuel consumption is 37% while changing between 9210 m^3 and 6447 m^3 for insulated wall and the decrease in the fuel consumption is 30%. As the outdoor temperature goes down, the saving from the fuel consumption increases more for insulated wall. At an outdoor temperature of -15°C, the saving is 66% as it is compared to the uninsulated wall.

Figure 3 depicts the change of CO_2 emission as a function of outdoor air temperature for insulated and uninsulated walls in the case of natural gas. As the outdoor air temperature increases, CO_2 emission decreases. This is because the fuel consumption decreases, and thereby decreasing the firing rate as the outdoor temperature increases. CO_2 emission is directly related to the fuel consumption, so Figures 2 and 3 show similar trends. CO_2 emission decreased from 30952 kg equivalent CO_2 to 19274 kg equivalent CO_2 for uninsulated wall at the outdoor air temperatures of -15°C and +4°C. In other words, it is decreased by 37%. CO_2 emission decreased from 206782 kg equivalent CO_2 to 14474 kg equivalent CO_2 for insulated wall. In other words, it is decreased by 30% for insulated wall. CO_2 emission is directly related to the fuel consumption.

Figure 4 shows the change of total radiator length as a function of insulation thickness for insulated concrete and brick walls. As it is shown in Figure 4 that, total radiator length decreases for both insulated concrete and brick walls as the insulated thickness increases. Total radiator length changes between 70.4 m and 42.2 m for insulated brick wall at the insulated thicknesses of 0 and 18 cm and the decrease in the total radiator length is 67%. It changes between 83.4 m and 42.5 m for insulated concrete wall and the decrease in the total radiator length is 96%. As the minimum insulation thickness of 6 cm is taken into consideration for the heat transfer requirement of the building in this study, the difference in the total radiator length for insulated concrete and brick walls is only 1.5%. Above the insulated thicknesses of 6 cm, the difference in the total radiator length can be

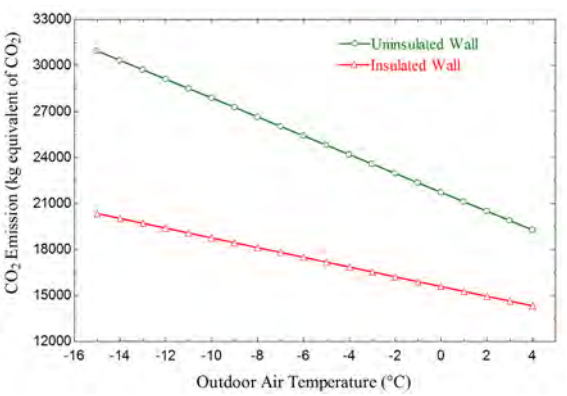

Figure 3. CO_2 emission versus outdoor air temperature for insulated and uninsulated walls

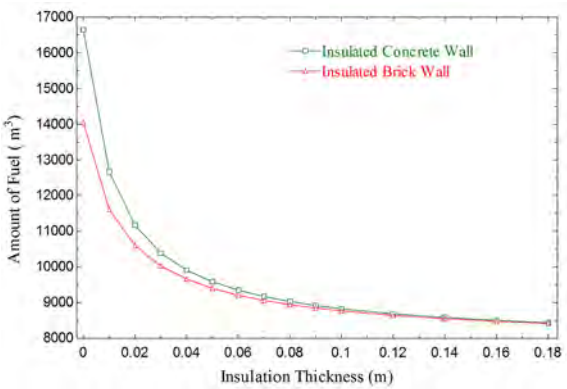

Figure 5. Fuel consumption versus insulation thickness for insulated concrete and brick walls

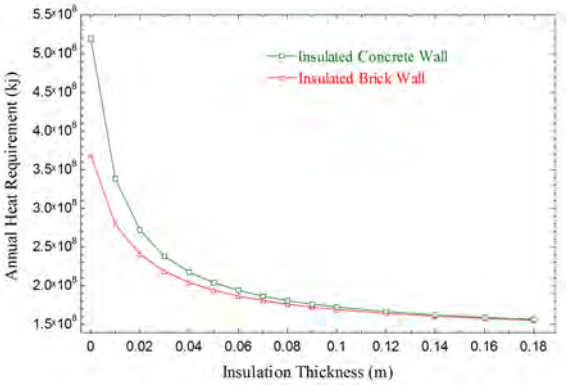

Figure 6. Annual heat requirement versus insulation thickness for insulated concrete and brick walls.

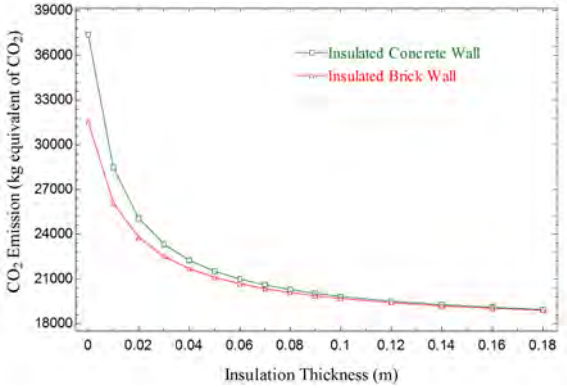

Figure 7. CO_2 emission versus insulated thickness outdoor air temperature for insulated concrete and brick walls.

ignored for both walls. It is also clear from Figure 4 that it is advantages to select brick wall for energy saving below the insulation thicknesses of 6 cm.

Figure 5 depicts the variation of fuel consumption as a function of insulation thickness for insulated concrete and brick walls. Fuel consumption and total radiator length are related to each other. As the total radiator length decreases, fuel consumption also decreases for the increasing values of insulation thicknesses. Therefore, Figure 5 depicts the same trend with Figure 4. Fuel consumption decreases from 14049 m^3 to 8418 m^3 for the insulated brick wall while it decreases from 16650 m^3 to 8440 m^3 for the insulated concrete wall between the insulation thicknesses of 0 and 18 cm. The percent decrease at the insulation thickness for the insulated brick and concrete walls are 67% and 97%, respectively. At the selected insulation thickness of 6 cm, the fuel saving is 140 m^3 if the insulated brick wall is selected for the building material.

Figure 6 shows the variation of annual heat requirement with respect to the insulation thickness for the insulated concrete and brick walls. As the annual heat requirement increases, this causes the fuel consumption to increase, similar results can be concluded as in Figure 5. Annual heat requirement decreases as the insulation thickness increases for both insulated concrete and brick walls. The annual heat transfer requirement decreases from $3{,}69x10^8$ kj to $1{,}55x10^8$ kj, 58% decrease, for the insulated brick wall and it decreases from $5{,}19x10^8$ kj to $1{,}56x10^8$ kj, 70% decrease, for the insulated concrete wall at the insulated thicknesses of 0 and 18 cm. Below the insulation thicknesses of 6 cm, the gap between the insulated brick wall and insulated concrete wall increases as shown in Figure 6. Figure 7 depicts the variation of CO_2 emission with respect to the insulation thickness for the insulated concrete and brick walls. As the insulation thickness increases, the heat transfer rate decreases. This causes the fuel consumption to increase, and thereby decreasing CO_2 emission as shown in Figure 7. CO_2 emission decreases from 31543 kg equivalent CO_2 to 18900 kg equivalent CO_2 for the insulated brick wall at the insulation thicknesses of 0 and 18 cm while decreasing from 37382 kg equivalent CO_2 to 14474 kg equivalent CO_2 for insulated wall. At the insulation thicknesses larger than 6 cm, the difference in CO_2 emission for both types of walls can be neglected, but the difference under the values of 6 cm becomes larger.

CONCLUSIONS

The effects of outdoor air temperature and insulation thickness on the total radiator length, the fuel consumption and CO_2 emission were observed by a computer program. The effect of the insulation thickness on the annual heat requirement was also studied. At the outdoor air temperatures ranging from -15°C to 4°C, it was concluded that the fuel consumption and CO_2 emission were decreased by 30 % in the case of insulated brick wall while they were decreased by 37% in the case of uninsulated brick wall. It was also observed that 50% of fuel was saved as the insulated brick wall was used instead of uninsulated brick wall at the outdoor air temperature of -15°C. It was observed that the decrease in the total radiator length, fuel consumption and CO_2 emission is 96% for the insulated brick wall at the insulated thicknesses between 0 and 18 cm while it was 67% for the insulated concrete wall. For the insulation thickness of 6 cm, the annual heat requirement was decreased by 4% for the insulated brick wall as it is compared to the insulated concrete wall.

REFERENCES

1. Boeck LD, Verbeke S, Audenaert A, Mesmaeker LD. Improving the energy performance of residential buildings: A literature review. Renewable and Sustainable Energy Reviews. 52 (2015) 960–975.
2. Kaynaklı Ö, Yamankaradeniz R. Isıtma Süreci ve Optimum Yalıtım Kalınlığı Hesabı. VIII. Ulusal Tesisat Mühendisliği Kongresi, İzmir, pp. 187–195, 2007.
3. Gelegenis J, Axaopoulos I, Axaopoulos P. Optimum insulation thickness for external walls on different orientations considering the speed and direction of the wind. Applied Energy 117 (2014) 167-175.
4. Özkan DB, Onan C, Erdem S. Effect of Insulation Materıal Thıckness on Thermal Insulation. Journal of Engineering and Natural Sciences 27 (2009) 190–196.
5. Dombaycı ÖA. The environmental impact of optimum insulation thickness for external walls of buildings. Building and Environment 42 (11) (2007) 3855–3859.
6. Uçar A, Balo F. Determination of the energy savings and the optimum insulation thickness in the four different insulated exterior walls. Renewable Energy 35 (1) (2010) 88–94.
7. Bolattürk A. Determination of optimum insulation thickness for building walls with respect to various fuels and climate zones in Turkey. Applied Thermal Engineering 26(11–12) (2006) 1301–1309.
8. Dombaycı ÖA, Gölcü M, Pancar Y. Optimization of insulation thickness for external walls using different energy–sources. Applied Energy 83(9) (2006) 921–928.
9. Byun SJ , Park HS, Yi SJ, Song CH , Choi YD , Lee SH, Shin JK. Study on the optimal heat supply control algorithm for district heating distribution network in response to outdoor air temperature. Energy 86 (2015) 247–256.
10. Lü X. Modelling of heat and moisture transfer in buildings: I. Model program. Energy and Buildings 34(10) (2002) 1033–1043.
11. Ogonowski S. Modeling of The Heating System in Small Building for Control. Energy and Buildings 42(9) (2010) 1510–1516.
12. Kim MS, Kim Y, Chung K. Improvement of intermittent central heating system of university building. Energy and Buildings 42(1) (2010) 83–89.
13. Klein SA. Engineering Equation Solver (EES). Professional version V9.723–3D F–Chart Software, 2010.
14. Tunay B. Merkezi ısıtma sisteminde etkili olan parametrelerin araştırılması, MSc. Thesis Hitit University Graduate School of Natural and Applied Sciences, Çorum, 2014.
15. Genceli OF, Parmaksızoğlu C. Kalorifer Tesisatı, MMO, Ankara, 2003.
16. Yazıcı H, Akçay M, Özer S. Fuel cost and CO_2 emission quantity determination with different fuel types for a building in Denizli. SDU International Technologic Sciences 4(2) (2012) 59–69.

Hittite Journal of Science and Engineering, 2015, 2 (2) 151-157
ISSN NUMBER: 2149-2123
DOI: 10.17350/HJSE19030000019

Design of A Specific MatLab Code for Processing of Standard Tensile Test Data for Sheet Metal Forming Simulations

Baris Cetin, Murat Kasikci and Askin Hayat Uslu
FNSS Defense Systems Co. Inc., Dept of Engineering and Research, Ankara, TURKEY

ABSTRACT

In order to obtain proper and sufficiently precise results from metal forming simulations, accurate material data should be input to the simulation software. One of the most important input for the simulation software is the flow curve (yield curve) of the material. Although there are many tests which could be performed in order to construct the flow curve such as standard tensile test, hydraulic bulge test, frictionless dome test, etc., standard tensile test is the simplest and cheapest technique despite of its technical restrictions.

In this article, the studies regarding to the creation of a specific MatLab code for processing of tensile test data are presented. This specific MatLab code is capable of determining the constants of Hollomon's, Ludwig's, Swift's and Voce's hardening equations with their regression results, as well. By means of this code, the proper flow curve of any material and also the Lankford parameters could be obtained and the hardening equations which fits best to the experimental data could be determined.

Key Words:
Tensile Test; Flow Curve; Hardening Equation; Sheet Metal Forming Simulation.

Article History:
Received: 2015/10/14
Accepted: 2015/12/07
Online: 2015/12/30

***Correspondence to**: Baris Cetin,*
FNSS Defense Systems Co. Inc.,
Department of Engineering and Research
Ankara, TURKEY
Tel: +90 (312) 497 46 19
Fax: +90 (312) 497 43 01
E-Mail: cetin.baris@fnss.com.tr

INTRODUCTION

In sheet metal forming operations the mechanical properties of the sheet material (i.e. flow stress or stress–strain curve) greatly influence metal flow and product quality. Therefore, accurate determination of the flow stress is of paramount importance in process simulation via finite element method (FEM) [1]. There are several possible methods or test options for determining the flow curve of the materials. It could be stated that apart from standard tensile test, the other methods necessitates some more complicated set-ups and computations. Even some digital image correlation (DIC) applications may also be compulsory for some cases which dominantly affects the cost of the experiment. Conventionally, tensile test is used to determine flow stress curves. However, tensile test data is limited to small amount of strain, due to uniaxial instability (necking) [2]. Despite of its limitation on maximum obtainable strain values, standard tensile test is commonly used because of its low cost and ease of accessibility. For instance a standard tensile test machine may be found in any mechanical characterization lab in Turkey, but the total quantity of hydraulic bulge test machine is less than five all around the country. There is another important point that well-defined testing standards and technical recommendations exist for many years for standard tensile test such as EN ISO 6892-1 [3]. However it is not valid for bulge test. Although the hydraulic bulge test was used for a long time, especially in sheet metal forming, the standard ISO 16808:2014 is recently published for determination of biaxial stress-strain curve by means of bulge test with optical measuring system [4].

By means of proper data processing and curve-fitting techniques, it is possible to obtain the flow curves with a reasonable amount of uncertainty. In other words, the amount of precision could be sufficient enough for most cases under the condition that standard tensile test data is processed by convenient techniques.

LIMITATIONS of STANDARD TENSILE TEST

Generally in industrial solutions, a standard tensile test machine (Zwick Roell, Instron, MTS, etc.) is used

for mechanical testing with their specific software. The embedded software usually is capable of computing the ultimate tensile strength (UTS), yield strength ($R_{p0,2}$), the Young's modulus (E), the maximum percent elongation, and Lankford parameter (r). In some applications they may also determine the strength coefficient (K) and exponent of strain hardening (n). A sample test result is illustrated in Figure 1.

However standard tensile test has limitations for sheet metals because it only provides the stress–strain behavior of the sheet material under uniaxial deformation conditions. In contrast, during stamping operations the material deforms under biaxial conditions of deformation. Under the biaxial tensile this state of stress, the true strain level may reach a magnitude of about 0.7 or more. With the standard tensile test, however, the true strain level can hardly reach 0.3 [1]. The basic reason of that limited max. true strain value is the instability in the form of early necking encountered during the tension test. This phenomenon hinders the post-diffuse-necking computation of stresses and strains based on the elementary measurements of force and extension in the axial direction [5]. Therefore, in process simulations via

Nr	L0 mm	S0 mm²	Rp 0.2 N/mm²	E-Modulus kN/mm²	ReH N/mm²	Tensile strength N/mm²	ε Fmax. %	Elongation %
1	110,00	130,1	925,84	34,36	-	1108,11	4,95	4,95
2	110,00	131,3	916,58	33,71	-	1007,68	3,71	3,71

Series graph:

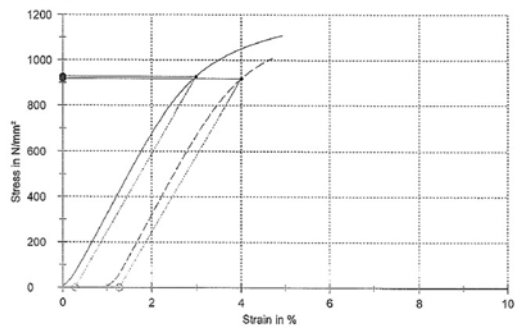

Figure 1. A standard tensile test result obtained from Zwick-Roell machine.

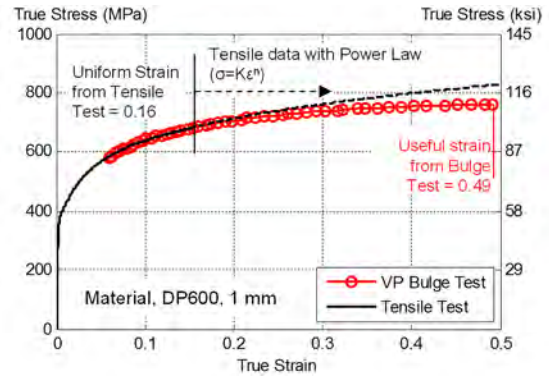

Figure 2. A comparison of standard tensile test and hydraulic bulge test for DP 600 steel [2].

finite element method (FEM), the flow curve obtained from tensile test must be extrapolated. This may cause significant errors in process simulations using FE codes [1]. The result of a case study on determination of the uncertainty introduced by the extrapolation of tensile test data is shown in Figure 2.

ADVANTAGES of DATA PROCESSING

In scientific research studies, the obtained force-displacement data from tensile test machine is processed separately by special techniques. The embedded software makes the computation with some basic assumptions. However by means of a special MatLab code which is dedicated to this task, more realistic and precise results could be obtained. In this article created new MatLab code is used for processing of tensile test data of TBF-1050 (TRIP Aided Bainitic Ferrite) steel [6]. The tensile test is performed at Zwick/Roell Z300 machine. The software is Text Expert which is embedded to the tensile test machine. The details of special data processing is explained in coming sections.

Pre-Load Correction in Data Processing

In tensile testing in order to eliminate the slip/stick affect at the beginning of the test, a pre-load is generally applied. As a common application, the extensometers are clamped (prepared for the data record) after the application of pre-load to the tensile specimen. Therefore there is an elastic elongation at the beginning of the tensile test and generally this elongation is neglected by the embedded software. However by means of data processing with MatLab, a pre-load correction can be easily applied to the experimental data. For the pre-load correction, it is sufficient to modify the formulations of true strain and true stress values as below:

$$\Delta = \frac{P * G}{P + A_0 * E} \tag{1}$$

$$\sigma_{true} = \left(\frac{F}{A_0}\right)\left(\frac{G + \Delta L}{G - \Delta}\right) \tag{2}$$

$$\varepsilon_{true\,plastic} = \ln\left(\frac{G + \Delta L}{G - \Delta}\right) - \left(\frac{\sigma_{true}}{E}\right) \tag{3}$$

where Δ is the elongation that corresponds to the pre-load, P is the pre-load, *G* is the initial gage length which is a default value of extensometer, *F* is the force, A_0 is the initial cross-sectional area, E is the Young's modulus and *ΔL* is the longitudinal elongation recorded by the extensometer [7].

This pre-load correction may also be done to calculate Lankford parameters which is also neglected by the

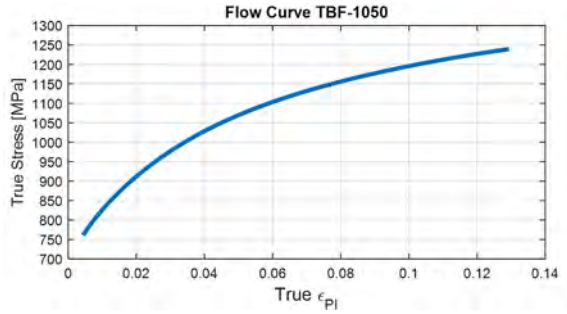

Figure 3. Flow Curve of TBF-1050 Steel.

embedded software of tensile test machine.

$$r = \frac{-\ln\left(\frac{w_0 - \Delta w}{w_0}\right)}{\ln\left(\frac{G + \Delta L}{G - \Delta}\right) + \ln\left(\frac{w_0 - \Delta w}{w_0}\right)} \quad (4)$$

where w_0 is the initial width, and Δw is the change in width recorded by the extensometer. If the pre-load is omitted then it is possible to use the conventional true stress, true strain formulations as specified in standards [8]. Contrast to this fact, in created MatLab code, these proposed calculations (Eq. 1-4) are engaged related to pre-load correction. The flow curve obtained from created MatLab code with preload correction is shown in Figure 3.

Furthermore, the specimens should be controlled visually after the test for their clamping marks. In some of the tests, slippage may observed as shown in Figure 4.b even if a pre-load is applied. For these specific cases, the tensile tests have to be re-done until proper results were obtained as in Figure 4.a [7].

Computation of Yield Strength by Extrapolation of Flow Curve

Determination of yield strength (or yield stress) is not an easy task. There is always some ambiguity in computing the yield strength.

As it is stated in the literature, the yield strength is not unique in recognition that the plastic deformation in metals due to dislocation flow is not a singular event but a diffuse process [9]. In order to avoid ambiguities in determination of the yield strength, the most commonly used convention is to define the yield strength as the stress required to produce a small previously specified amount of permanent strain or plastic deformation. For most metallic materials, the commonly specified offset strain is 0.002 (or 0.2%) [10]. The embedded software of tensile test machines generally uses $R_{p0.2}$ method. However in this $R_{p0.2}$ approach, the calculated stress is the engineering stress which does not actually a physical meaning in continuum mechanics point of view and also discontinues yielding phenomena is commonly faced with in sheet metals. Thus some more sophisticated and precise approaches exist in sheet metal forming applications in determination of the yield strength. For instance, yield strengths of the tensile specimens could be calculated from the extrapolation of the flow curve (true plastic strain vs. true stress curve) to the zero true plastic strain value. For this extrapolation, high order polynomial curve-fitting might be applied to the flow curve. In this study, 4th order polynomial fit is used because it is observed that this fit operation has sufficient amount of success ($R^2 > 0.99$). This more scientific and precise method is used in the created MatLab code. MatLab code is capable of performing the curve-fitting coefficients and store the last term which is actually the yield strength and display it in the command window. An example of the extrapolation operation is illustrated in Figure 5. An example of command window representation is also shown in Figure 6.

Determination of the Hardening Equations Coefficients

There are several possible hardening equations which could be used to describe the flow curve. Generally four of them is most commonly treated. These are Hollomon's, Swift's, Ludwig's and Voce's hardening equations which are illustrated below:

$$\sigma = K * \varepsilon^n \quad \text{(Hollomon)}$$

Figure 4. a) Clamping marks, no slippage observed.

Figure 4. b) Clamping marks, slippage observed.

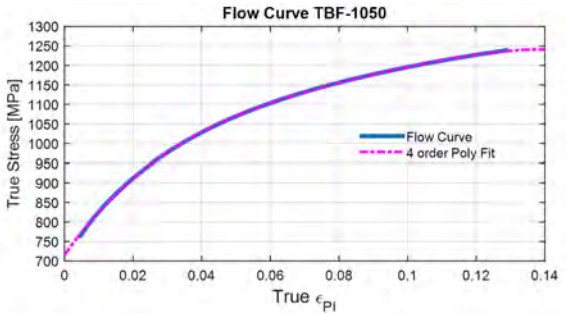

Figure 5. Determination of yield strength by extrapolation of flow curve.

machines give only the *K* and the *n* values. In contrast, the created MatLab code is capable of performing curve fitting operation with respect to all four basic hardening equations. The regression analysis is also written in the command window by means of which the user could select the most convenient hardening equation for the tested material, i.e. the fit result which has the biggest R^2 value. After selecting the best-fitted hardening equation it can easily be imported to the metal forming simulation software like Ls Dyna, PamStamp and etc. The results of curve fitting operations performed by the MatLab code for TBF-1050 steel is shown in Figure 7.

```
The coefficients and fit performance data of Poly fit to flow curve of TBF 1050 are as below:
     Linear model Poly4:
     fitresult(x) = p1*x^4 + p2*x^3 + p3*x^2 + p4*x + p5
     Coefficients (with 95% confidence bounds):
       p1 =  -2.647e+06  (-2.689e+06, -2.605e+06)
       p2 =   9.853e+05  (9.741e+05, 9.965e+05)
       p3 =  -1.473e+05  (-1.483e+05, -1.463e+05)
       p4 =   1.233e+04  (1.229e+04, 1.236e+04)
       p5 =       715.7  (715.4, 716.1)
          sse: 1.4170e+03
       rsquare: 0.9999
           dfe: 1537
    adjrsquare: 0.9999
         rmse: 0.9602

The Yield Strength of TBF 1050 is below:
  715.7264
  MPa
```

Figure 6. Command window representation of the created MatLab code.

$$\sigma = K*(\varepsilon_0 + \varepsilon)^n \quad \text{(Swift)}$$

$$\sigma = \sigma_0 + K*\varepsilon^n \quad \text{(Ludwig)}$$

$$\sigma = B - (B - A)*\exp(-n*\varepsilon) \quad \text{(Voce)}$$

where σ is the true stress, ε is the true plastic strain and the others are equation constants [11]. The most basic hardening equation is the Hollomon's which is named as *"Power Law"* in some scientific papers. Because of that fact, some embedded software of tensile test

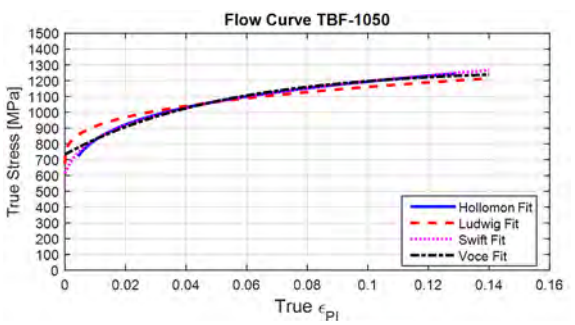

Figure 7. Curve fitting results of four hardening equations for TBF-1050 steel.

Determination of the Lankford Parameter

In microstructural scale, the mechanical properties of all single crystals differ with respect to the orientation. In other words, it could easily be stated that single crystals are anisotropic. On the other hand, the polycrystalline structures, under the condition that there is sufficient amount of grains that are randomly oriented exhibit isotropic behavior. However it is not the case for sheet metals. Since they are always processed by rolling operations, they usually gain a textured microstructure which leads to anisotropy [12]. In other words the cold or hot deformation history of sheet metals in production chain causes anisotropy. Therefore it is a well-accepted assumption that sheet metals are anisotropic.

The variation of plastic behavior of sheet metals with direction is assessed by a quantity called Lankford parameter or anisotropy coefficient. The anisotropy coefficient *"r"* is defined by:

$$r = \frac{\varepsilon_2}{\varepsilon_3} \quad (5)$$

where ε_2 and ε_3 are the strains in the width and the thickness directions respectively [13]. By using the

```
for i=1:length(TPStrain)
        R0(i) = -log((W-TD1.data(i,3))/W)/(log((G+TD1.data(i,1))/(G-D))+ log((W-TD1.data(i,3))/W));
end;
FigH = figure('Units','Inches','Position', [1, 1, 6, 3],'PaperPositionMode','Auto');
plot(TPStrain,R0,'LineWidth',2);

[x4,button]=ginput(1);
[x5,button]=ginput(1);

% R0Av and TStrainAv are the averaging values

TPStrainAv = TPStrain;
R0Av = R0;

% This loop deletes the data which are out of avareqinq range ,i.e. out of
% user cursor click

for i=length(TPStrain):-1:1
    if TPStrain(i)<x4 || TPStrain(i)>x5
        TPStrainAv(:,i) = [];
        R0Av(:,i) = [];
    end;
end;
```

Figure 8. An example MatLab code for deleting the unstable regions of "r vs. ε_{pl}" curve.

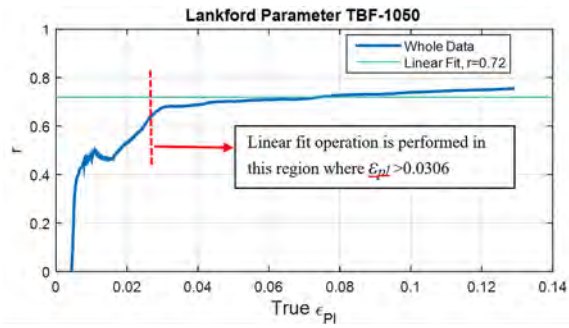

Figure 9. Computation of the Lankford parameter by linear fit to stable region of "r vs. ε_{pl}" curve.

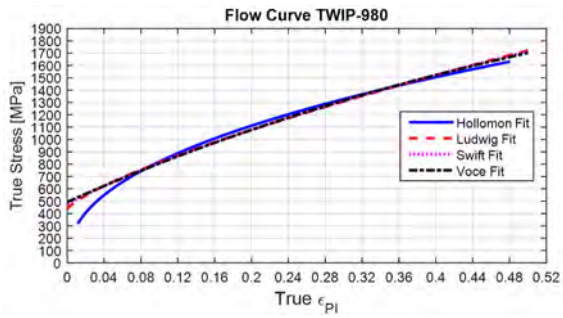

Figure 10. Curve fitting results of four hardening equations for TWIP-980 steel.

volume constancy (Eq. 6) the Lankford parameter can also be calculated as:

$$\varepsilon_1 + \varepsilon_2 + \varepsilon_3 = 0 \tag{6}$$

$$r = \frac{-\varepsilon_2}{\varepsilon_1 + \varepsilon_2} \tag{7}$$

In tensile test, the elongations from longitudinal and transversal extensometers are recorded instantaneously. By

Table 1. Comparison of the MatLab code and the embedded software computations.

	Yield Strength (MPa)	*Lankford Parameter*
Embedded Software	*722.50*	*0.77*
MatLab Code	*715.70*	*0.72*

Table 2. Analysis of Curve Fits for Four Hardening Equations (TBF-1050)

Equations	*K(MPa)*	*n*	*σ_o(MPa)*	*ε_o*	*B (MPa)*	*A (MPa)*	*R^2*
Hollomon	*1733*	*0.1615*					*0.9979*
Ludwig	*1000*	*0.3105*	*671.6*				*0.9002*
Swift	*1768*	*0.1712*		*0.001889*			*0.9986*
Voce		*19.4*			*1275*	*733.4*	*0.9990*

Table 3. Analysis of Curve Fits for Four Hardening Equations (TWIP-980)

Equations	*K(MPa)*	*n*	*σ_o(MPa)*	*ε_o*	*B (MPa)*	*A (MPa)*	*R^2*
Hollomon	*2249*	*0.4379*					*0.9835*
Ludwig	*2178*	*0.7564*	*433*				*0.9987*
Swift	*2432*	*0.6305*		*0.07532*			*0.9991*
Voce		*1.389*			*2908*	*493.2*	*0.9996*

means of this fact, the Lankford parameter might also be computed in each time step. Therefore it is possible to plot *"r vs. ε_{pl}"* curve and perform a linear fit operation by a created MatLab code. When this curve is plotted some unstable regions could be detected which are caused by yield drop, discontinuous yielding, elastic effects and etc. Therefore it is a general application to compute the Lankford parameter by making a line fit to the stable region after deleting the unstable portion. For this purpose *"ginput"* function can be used in MatLab. By using this command the user may enter the strain values between which the Lankford parameter is wanted to be calculated. And a simple *"for loop"* can be engaged in order to eliminate the unstable region in linear fitting operation. The command lines of the MatLab code which is used for this computation approach is shown in Figure 8.

With using the MatLab code, this sophisticated computation approach for Lankford parameter is possible whereas embedded software generally use overall averaging approach which creates significant amount of deviations between computed values. The result of MatLab computation is shown in Figure 9.

RESULTS AND DISCUSSION

The expressed computation methods are applied to the tensile test data of TBF-1050 steel by created MatLab code. The comparison of the results from MatLab and embedded software and the analysis of four different hardening equation fits are shown in Table 1 and Table 2.

As could be seen in Table 2, the most appropriate hardening equation is Voce's equation for the processed data (TBF-1050 steel in rolling direction). On the other hand, it should not be neglected that this result may likely alter material to material. This is actually the powerful point of the code that users could easily detect the best hardening equation which will be used for sheet metal simulations regarding to the regression analysis. In Table.3, the results of the TWIP-980 steel is illustrated as a second example.

Lastly, as it is discussed previously, yield strength and Lankford parameter of any material could easily be computed by means of the created MatLab code. If the tensile specimens are prepared with respect to the rolling direction and 90 degree direction, then Hill-48 Yield Criterion parameters could automatically be determined. Hill-48 model is not highly complex yield surface definition compared to Hill-89, Barlat-2000 or Karafillis-Boyce and etc.; however, it is widely-used in sheet metal simulations due to its simplicity. It exhibits sufficiently well performance especially in monotonic loading cases. With a simple supplementary study on the MatLab code, Hill-48 yield surface could be obtained for TBF-1050 as illustrated in

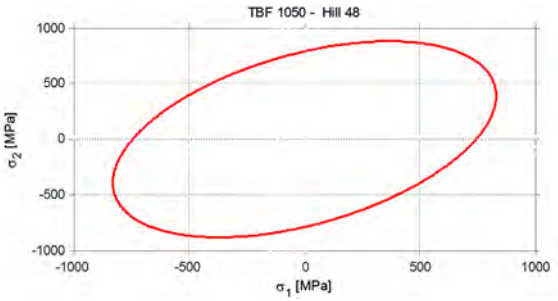

Figure 11. Hill-48 Yield Surface of TBF-1050

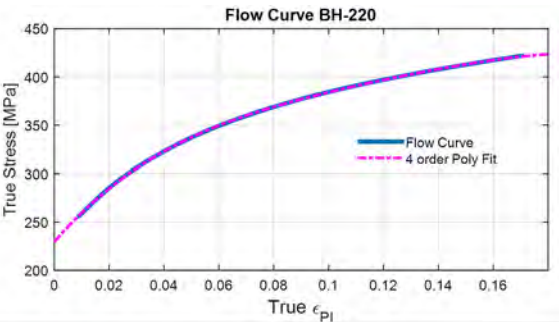

Figure 12. Determination of yield strength by extrapolation of flow curve for BH-220 steel.

Figure.11 if the rolling direction and 90 degree direction tensile tests are performed.

Hill-48 yield surface definition can be expressed as follows:

$$\sigma_1^2 - \left(\frac{2*r_0}{1+r_0}\right)\sigma_1\sigma_2 + \frac{r_0(1+r_{90})}{r_{90}(1+r_0)}\sigma_2^2 = \sigma_0^2 \qquad (8)$$

where r_0 and r_{90} are the Lankford parameters in rolling and 90 degree direction respectively, σ_0 is the yield strength in rolling direction and σ_1, σ_2 are the principal stresses [13].

CONCLUSIONS

In this study, a specific MatLab code which is consists of approximately three hundred command lines is designed in order to process the force and displacement data obtained by a standard tensile test. This MatLab code is capable of performing some corrections and more complex computations compared to the embedded software of the tensile test machine. Therefore, there are some differences between the two computations. By means of this specific MatLab code, more realistic and precise values could be obtained which increases the precision of the sheet metal forming simulations. Furthermore it is possible to determine the most realistic best hardening behavior of the material by comparing the

regression analysis. For instancte, in this specific case of TBF-1050 steel, Voce's hardening equations exhibits the best regression result.

Moreover, the MatLab code is designed flexibly, so that it can be used for any other material than TBF-1050 steel by just modifying the imported force-displacement data. This data can be imported in *.txt, *.tra or *.csv formats. Then, it takes just few seconds for MatLab code to make the whole computation.

One of the other advantage of this specific MatLab code is that it enables a standardization of material characterization by tensile test at FNSS Defense Systems Co. Inc. It is used for various other materials so far. An example which is the outcome of processing of BH-220 steel data with the MatLab code is illustrated in Figure 10.

As future work, new MatLab codes are being designed for processing of hydraulic bulge test data and also the high temperature, high strain rate characterization of metals at FNSS Defense Systems Co. Inc.

REFERENCES

1. Gutscher G, Wu HC, Ngaile G, Altan T. Determination of Flow Stress for Sheet Metal Forming Using the Viscous Pressure Bulge (VPB) Test. Journal of Materials Processing Technology 146 (2004) 1-7.
2. Billur E, Demiralp Y, Groseclose AR, Wadman B Altan T. Factors Affecting the Accuracy of Flow Stress Determined by the Bulge Test. International Conference on Technology of Plasticity, Aachen, Germany, September 2011
3. Aydemir B. Metalik Malzemelerin Çekme Deney Standardı EN ISO 6892–1'in Getirdiği Değişiklikler. Makine Teknolojileri Elektronik Dergisi 10 (2003) 61–70
4. ISO 16808:2014
5. Coruk E, Karadoğan C. Flow Curve Evaluation by Optic Strain Measurements and Force Balance at the Most Critical Section in the Neck Region of a Tensile Specimen. Steel Research International special edition (2011) 714–719
6. ArcelorMittal, Steels for cold stamping – Fortiform ®, 10/09/2014.
7. Billur E, Çetin B, Yılmaz MM, Oğuz AG, Atay A, Ersoy K, Uğuz RO, Kaftanoğlu B. Forming of New Generation AHSS Using Servo Presses. International Conference on Accuracy in Forming Technologies, Chemnitz, Germany, November 2015.ASTM E8/E8M–15a
8. Hull D, Bacon DJ. Introduction to Dislocations. Butterword Hinmann, Oxford. 2001
9. Shetty MN. Dislocations and Mechanical Behaviour of Materials. PHI Learning, Delhi, 2013
10. Kleemola HJ, Nieminen MA. On The Strain–Hardening Parameters of Metals. Metallurgical Transactions 5 (1974) 1863–1866 Tordache M, Teaca M, Charpentier I, Martiny M, Ferron G. Identification of Sheet Metal Plastic Anisotropy and Optimization of Initial Blank Shape in Deep Drawing. The Annals of Dunarea de Jos University og Galati 5 (2009) 149–154
11. Banabic D. Sheet Metal Forming Process, Springer–Verlag, Berlin, 2010.

Hittite Journal of Science and Engineering, 2015, 2 (2) 159-164
ISSN NUMBER: 2149-2123
DOI: 10.17350/HJSE19030000020

AC Servo Motor Speed and Position Control Using Particle Swarm Optimization (PSO)

Mehmet Fatih Isık[1], Erhan Cetin[2], Halil Aykul[2] and Husamettin Bayram[3]
[1] Hitit University, Department of Electrical and Electronics Engineering, Corum, TURKEY
[2] Hitit University, Department of Mechanical Engineering, Corum, TURKEY
[3] Hitit University, Department of Industrial Engineering, Corum, TURKEY

ABSTRACT

In this article, a new design method, called Particle Swarm Optimization (PSO), is used for the determination of PID control parameters; this is designated for the controlling of the speed and the position of the AC servomotor. For the determination of the decision parameters AC servomotors are mathematically modelled. Rise time, settling time, and overshoot are taken into consideration, during the optimization process. Controller's performance is determined based on different criteria, such as, ITAE (Integral of Time Weighted Absolute Error), IAE (Integral of Absolute Error), ISE (Integral of Squared Error) and ITSE (Integral of Time Weighted Squared Error). Superiority and accuracy of the proposed technique was verified by simulation results. In addition, considering the quality of the obtained results, proposed technique is found effective and strong in reduction of the error of motion control systems.

Key Words:
Particle Swarm Optimization; PSO, Servomotors; Motion Control.

Article History:
Received: 2015/09/30
Accepted: 2015/12/11
Online: 2015/12/30

***Correspondence to**: Erhan Çetin,*
Hitit University, Faculty of Engineering,
Department of Mechanical Engineering,
Corum, Turkey
Tel: +90 (364) 227 45 33 (12 42)
Fax: +90 (364) 227 45 35
E-mail: erhancetin@hitit.edu.tr

INTRODUCTION

Without specific design and application difficulties, servomotors, which are regarded as sequenced systems, are preferred in non-linear and dynamic working conditions [1-10]. AC servomotors are also widely used in various control applications such as: numerical control, precise robot applications, and CNC machinery [11-14]. Along with its electrical and mechanical dynamics, one of the most important reasons these motors are so popular is their high efficiency. Ac servomotors need an accurate feedback response for the reference position. The feedback signals are important for servomotor to quickly respond to on-off operations and to maintain its steady state in sudden load changes. In automation applications, where feedback signals are used, such as speed, position and torque, even if a mathematical model is correctly constructed, using this mathematical model may cause complex problems and higher costs. Therefore, implementation of some control algorithms to uncertain, inaccurate, not well defined time-variable and complex systems may be impossible. Some of the leading problems of the complex systems are as follows: non-linearity of system, unknown mathematical model, difficulties in measurement, substantial time-variability of model parameters etc. Therefore, instead of mathematical statements, intelligent techniques are needed.

Nowadays several methods can be used to solve complex computational problems inspired by nature. One of these methods is the particle swarm optimization (PSO) technique [15-21]. PSO, which is a population-based stochastic optimization technique and is developed by Kennedy and Eberhart in 1995, is inspired by bird flocks' social behaviors.

In the algorithm, particles are defined as points in an N dimensional space, where each dimension represents a decision variable. Every particle determines its flying direction based on both its and the swarm's directions. Namely, unlike the evolution based techniques, particles benefit from their and the swarm's previous experience in reaching to the solution.

The main aim of the research was to specify optimal K_p, K_i and K_d (PID) parameters, which are needed for a better movement control; and particle

swarm optimization (PSO) was used to determine the optimum PID parameters.

MATERIAL AND METHODE

Servo Control Unit

Control signal applied to the servomotor is limited by the signal voltage, which is generated by the modulator. In addition, the control voltage for the formation of the magnetic rotary field, the reference voltage must be the same frequency.

Technical specifications of the servomotor of the control system are given in Table 1.

Table 1. AC Servomotor parameters.

Model		*K40030H*
Rated Power		*400W*
Rated Torque		*1.3 Nm*
Rated Speed		*3000 r/min*
Maximum Rotation Speed		*6000 r/min*
Maximum Torque		*3.8 Nm*
Rated Current		*2.4 A(rms)*
Maximum Current		*10.2 (0-p)*
Rotor Inertia	*Without Brake*	*0.26 × 10⁻⁴ kgm²*
	With Brake	*0.28 × 10⁻⁴ kgm²*
Mechanical Time Constant	*Without Brake*	*0.43 ms*
	With Brake	*0.46 ms*
Electrical time constant		*3.4 ms*

Particle Swarm Optimization (PSOa)

PSO algorithm starts with a population of random solutions and updates the population in each iteration until it reaches optimum solution. Every particle in a population represents a solution and it produces an answer for every unknown. These answers show a particle's position in the solution space. Every particle kept the memory of its best solution until the current iteration. This solution is called p_{best}. G_{best} and is the best solution ever reached during the search of solution. In other words, g_{best} is the best of the p_{best}s. The g_{best} in the final iteration is the best solution reached by the swarm.

Velocities (V) and positions (X) of M particles in an N dimensional search space is represented as follows:

$$X=\begin{pmatrix} X_{11} & X_{12} & \dots & X_{1N} \\ X_{21} & X_{11} & \dots & X_{2N} \\ \dots & \dots & \dots & \dots \\ X_{M1} & X_{M2} & \dots & X_{MN} \end{pmatrix} V=\begin{pmatrix} V_{11} & V_{12} & \dots & V_{1N} \\ V_{21} & V_{11} & \dots & V_{2N} \\ \dots & \dots & \dots & \dots \\ V_{M1} & V_{M2} & \dots & V_{MN} \end{pmatrix} \quad (1)$$

In the above given matrix i^{th} particle is denoted as:

$$X_i=\begin{bmatrix} X_{i1} & X_{i2} & \dots & X_{iN} \end{bmatrix} \quad (2)$$

Particles' best positions (p_{best}) are represented as follows:

$$Pbest=\begin{pmatrix} Pbest_{11} & Pbest_{12} & \dots & Pbest_{1N} \\ Pbest_{21} & Pbest_{22} & \dots & Pbest_{2N} \\ \dots & \dots & \dots & \dots \\ Pbest_{M1} & Pbest_{M2} & \dots & Pbest_{MN} \end{pmatrix} \quad (3)$$

Every row in this matrix is an individual particle's best position in an N dimensional search space. Global best solution (g_{best}) is the best position among p_{best}s and given as a vector.

$$Gbest=\begin{bmatrix} gbest_1 & gbest_2 & \dots & gbest_N \end{bmatrix} \quad (4)$$

Conceptually, PSO is based on the determination of particles' velocities in a given iteration considering their previous best positions and the swarm's best position. During the search process a particle's velocity and position are updated by using the following equations [15].

$$v_{i,d}^{(t+1)}=wv_{i,d}^{(t)}+c_1r_1(pbest_{i,d}-x_{i,d}^{(t)})+c_2r_2(gbest_d-x_{i,d}^{(t)}) \quad (5)$$

$$x_{i,d}^{(t+1)}=x_{i,d}^{(t)}+v_{i,d}^{(t+1)} \quad (6)$$

$$i=1,2,\dots,m\ ;\quad d=1,2,\dots,\mathrm{n} \quad (7)$$

Social effect coefficients, c_1 and c_2 are positive numerals and they reflect the effects of the p_{best} and the g_{best} on a particle, respectively. Values of these coefficients are generally between 0.2 and 2. R_1 and r_2 are random coefficients and they provide stochastic to the technique. R_1 and r_2 values are randomly drawn between 0 and 1 [22-25]. W is the inertia coefficient and is selected mostly between 0 and 1. Inertia is used in order to balance global and local search capabilities. While higher inertia coefficients are good for global searches, a lower inertia coefficient increases local searches. Thus, the inertia balance the weights of global and local searches and aims at reaching the best solution with the minimum possible number of iterations. Particles benefit not only from the experience of the best particle but also the experiences of all other particles. W is linearly reduced throughout the PSO iterations by using the equation [15].

$$w=w_{maks.}-iter\frac{w_{maks.}-w_{\min.}}{iter_{maks.}} \quad (8)$$

Where *iter* is iteration number.

In PSO, particles change their positions until the maximum number of iterations is reached. The changes in the positions of the particles is given in Figure 1.
Where;

X^k : current position
X^{k+1} : position in the following iteration
V^k : current velocity
V^{k+1} : velocity in the following iteration
V^{Pbest} : p_{best} based velocity
V^{Gbest} : g_{best} based velocity

The algorithm, which is developed for movement control, is given in Figure 2. In this algorithm, initial positions and velocities of particles are randomly determined. Iteratively, new positions and speeds of particles are found and compared to their previous best positions. If the new position of a given particle is better than the previous best position of the particle, then the new position is recorded as the best position. But, if the new position is worse than the best position, the best position data is not updated. In addition, the best position of every particle is checked, and if the best of the best particle positions is better than the global best, then the global best is updated. These steps are repeated until the termination condition is met. The global best value reached at the last iteration of the algorithm is the best position reached by the algorithm.

Control Design

For the optimization of PID parameters of a movement control system PSO algorithm is used. Firstly, AC servomotor of the movement control system is mathematically modeled. Then, PID based control is applied to the system. According to this, general statement of PID controls as follows:

$$U(t) = K_p e(t) + \frac{1}{T_i}\int e(t)dt + T_d \frac{de(t)}{dt} \quad (9)$$

Where K_p, T_i, T_d, e(t) are proportional gain, integral time, derivative time and error between the input value and the output, respectively.

PSO-PID controller is shown in Fig. 3. Here, plant represents the system to be controlled, namely the transfer function. Transfer function is obtained by using Omron K40030H servomotor's specifications.

$$U(s) = K_p + \frac{K_i}{s} + K_d s \quad (10)$$

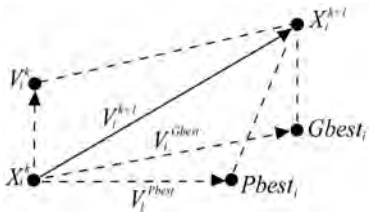

Figure 1. Illustration of PSO parameters as vectors.

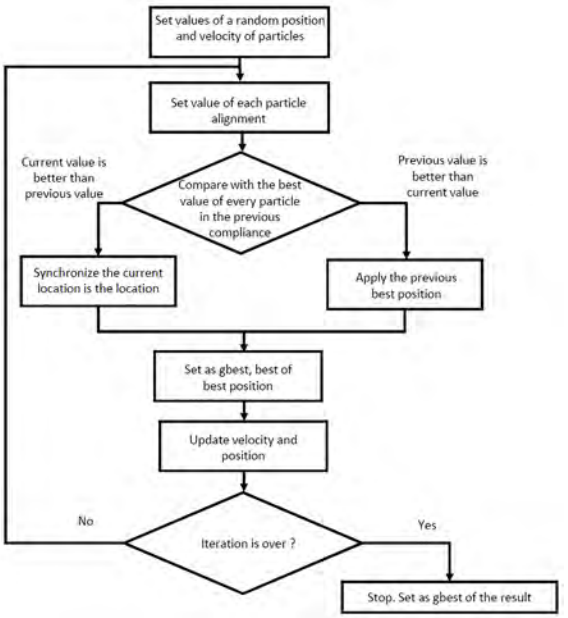

Figure 2. PSO flow diagram for motion control.

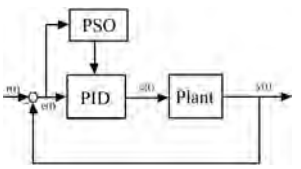

Figure 3. PSO-PID Controller.

PSO is used as an algorithm that will provide K_p, K_i and K_d values using the optimal output, thus creating the desired values.

Fitness Function

There are many methods in the literature for the determination of the performance of the controller. Some of these criteria are integral of absolute error (IAE), integral of time weighted absolute error (ITAE), integral of squared error (ISE) and integral of time weighted squared error (ITSE). These performance criteria have their disadvantages as well as their advantages. For example, one of the disadvantages of IAE and ISE are the solutions obtained by using them have longer settling time because, ISE performance criterion is totally independent of the time of the errors. Although ITSE performance criterion overcomes this disadvantage of ISE, derivative of its analytical expression is time-consuming.

Mathematical expressions of IAE, ISE, ITAE and ITSE criteria are as follows:

$$IAE = \int_0^\infty |r(t) - y(t)|dt = \int_0^\infty |e(t)|dt \quad (11)$$

$$ISE = \int_0^\infty e^2(t)dt \quad (12)$$

$$ITAE = \int_0^\infty t|e(t)|dt \quad (13)$$

$$ITSE = \int_0^\infty te^2(t)dt \quad (14)$$

Ziegler-Nichols Method

One of the methods of PID parameter (K_p, K_i, K_d) tuning is Ziegler-Nichols method. This method is used in two ways:

1. Referring to open system response and PID parameters are determined like Table 2.

T, K and L signal wave period, system response slope and dead time, respectively.

Table 2. Ziegler-Nichols open loop adjustment parameters

Controller	K_p	$T_i=K_p/K_i$	$T_d=K_d/K_p$
P	T/L	-	0
PI	0.9 (T/L)	L/0.3	0
PID	1.2 (T/L)	2L	0.5L

2. Initially, according to the closed loop response given in Figure 4. K_i and K_d values are assumed to be 0. K_p value is increased until system starts oscillating. K_p value at this moment is named as K_u and the parameters are calculated as given in Table 3.

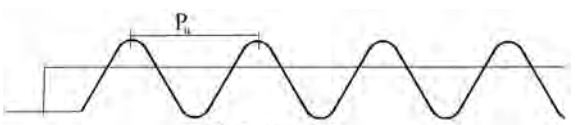

Figure 4. Closed loop system response of Ziegler –Nichols method.

Numerical Examples and Results

Transfer function for AC servomotor is obtained as given below:

$$\frac{Q_{(s)}}{E_{c(s)}} = \frac{K_1}{J_m s^2 + (B_m + K_2)s} \quad (15)$$

Table 3. Ziegler-Nichols Closed loop adjustment parameters

Controller	K_p	T_i	T_d
P	$K_u/2$	-	0
PI	K_u 2.2	$P_u/1.2$	0
PID	$K_u/1.7$	$P_u/2$	$P_u/8$

Table 4. K_p, K_i and K_d values obtained by using different criteria.

Tuning Method	K_p	K_i	K_d
Z-N PID	2.9400	0.0327	0.0081
PSO-PID1 (IAE)	4.9986	0.3359	0.9881
PSO-PID2 (ITAE)	4.8988	0.3966	0.9979
PSO-PID3 (ISE)	4.9352	0.8713	0.9932
PSO-PID4 (ITSE)	4.9975	0.0879	0.9992

Table 5. Settling time, rise time, overshoot obtained by using different criteria.

Tuning Method	Over-shoot (%)	Rise Time (s)	Settling Time (s)	SSE
Z-N PID	15.4	0.02040	0.09700	-
PSO-PID1 (IAE)	-	0.00128	0.06520	-
PSO-PID2 (ITAE)	$2.62x10^{-9}$	0.00080	0.00098	-
PSO-PID3 (ISE)	-	0.00127	0.06530	-
PSO-PID4 (ITSE)	-	0.00126	0.06410	-

In the above given transfer function some parameters are:

Transfer function above;

$K_1 = 0.54167\,(Nm)/\mathrm{A}$

$J_m = 0.26 * 10^{-4}\, kgm^2\,(\text{no brake})$

$B_m = 4.13802852 * 10^{-3}\,(\mathrm{Nm})/(\mathrm{rad/s})$

$K_2 = 0.012273318\, Nm/(rad/s)$

Following PSO parameters are used and results are obtained under various performance criteria (IAE, ITAE, ISE, ITSE).

Population size = 100
$w_{maks.} = 0.9$
$w_{min.} = 0.4$
$C_1 = 2$
$C_2 = 2$
K_p = [0-5]
K_i = [0-1]
K_d = [0-1]

K_p, K_i and K_d values obtained by five different criteria are given in Table 4. Settling time, rise time, overshoot are shown in Table 5.

CONCLUSIONS

In this study, in order to determine the optimal K_p, K_i and K_d parameters (which are needed for a better movement control) PSO was used. Ziegler-Nichols, IAE, ISE, ITAE and ITSE were used as evaluation criteria within the algorithm. The difference between reference value and the system response was tried to be minimized. Different optimal PID values were compared to each other. Maximum overshoot value, rise time, settling time and steady-state error values have shown that different evaluation criteria caused the algorithm to respond differently for each of the five criteria. Among five criteria, the most acceptable values (minimum overshoot, the best rise time, and the best settling time) were obtained by using ITAE in a shorter time and without causing steady state error. With this study, it could be inferred that ITAE criterion within PSO is more appropriate for using in movement control applications.

In this research, PID parameters are determined using particle swarm optimization. This algorithm can apply not only in motor applications, but also other fields. In the future works comparison of PSO and other artificial intelligence (AI) techniques are planned in any subject such as optimum adhesive thickness for maximum strength. For this reason, the study can constitute the fundamentals of future works.

ACKNOWLEDGMENTS

We are grateful to Hitit University Scientific Research Projects Unit for supporting this project numbered (MUH01.12.004).

REFERENCES

1. Lee TF, Huang AC. Vibration suppression in belt–driven servo systems containing uncertain nonlinear dynamics. Journal of Sound and Vibration 330 (2011) 17–26.
2. Kayacan E, Oniz Y, Aras AC, Kaynak O, Abiyev R. A servo system control with time–varying and nonlinear load conditions using type–2 TSK fuzzy neural system. Applied Soft Computing 11 (2011) 5735–5744.
3. Kaddisi C, Kenne JP, Saad M. Indirect adaptive control of an electrohydraulic servo system based on nonlinear backstepping. Transactions on Mechatronics 16 (2011) 1171–1177.
4. Liu H, Li S. Speed control for PMSM servo system using predictive functional control and extended state observer. Transactions on Industrial Electronics 59 (2012) 1171–1183.
5. Partal S, Şenol İ, Bakan AF, Bekiroğlu KN. Online speed control of a brushless AC servomotor based on artificial neural networks. Turk J Elec Eng & Comp Sci 19 (2011) 373–383.
6. Zhang Y, Gong Y, Zhou K, Chen L. Design for AC servo position loop based on RBF neural network predictive control. International Conference on Mechatronics, Electronic, Industrial and Control Engineering (MEIC 2015), Shenyang, China, 1–3 June. pp. 784–787, 2015.
7. Narayanareddygari MR, Nagabhushan RK, Chandra MC, Devanna CR. ARM cortex processor based closed loop servo motor position control system. Sensors & Transducers Journal 141 (2012) 45–51.
8. Korayem MH, Imanian A, Tourajizadeh H, Khayatzadeh S, Maddah SME, Tajik A, Manteghi S. A method for simultaneous control of speed and torque of the motors of a cable suspended robot for tracking procedure. Scientia Iranica B 20 (2013) 1550–1565.
9. Li L, Wang T, Wu LL. Linear servo motor operating mechanism and control technique for high–voltage circuit breaker. Applied Mechanics and Materials 390 (2013) 429–433.
10. Zhang L, Zuo J, Yao X, Zhang X, Shuai L. A robot visual servo–based approach to the determination of next best views. Proceedings of 2015 IEEE International Conference on Mechatronics and Automation, Beijing, China, 2–5 August. pp. 2654–2659, 2015.
11. Gu J, Wang H, Pan Y, Wu Q. Neural network based visual servo control for CNC load/unload manipülatör. Optik 126 (2015) 4489–4492.
12. Wang ZH, Liu ZH. Application of Active Disturbance Rejection Controller in Wheeled Mobile Robot Servo System. Proceedings of 2014 IEEE Chinese Guidance, Navigation and Control Conference, Yantai, China, 8–10 August. pp. 324–329, 2014.
13. Zhu ZP, Du AM, Ma ZX, Zhang WY, Fan CG. Vehicle robot driver research and development based on servo motor control. Applied Mechanics and Materials 709 (2014) 272–275.
14. Nhon PNQ, Elamvazuthi I, Fayek HM, Parasuraman S, Ahamed Khan MKA. Intelligent control of rehabilitation robot: auto tuning pıd controller with interval type 2 fuzzy for dc servomotor. Procedia Computer Science 42 (2014) 183–190.
15. Kennedy J, Eberhart R. Particle swarm optimization. International Conference on Neural Networks Proceedings, Perth, USA, 27 November–01 December. pp. 1942–1948, 1995.
16. Steffy SA, Mangaiyarkarasi B, Jasper SS, Priyanka K, Soorya K. Analysis & reduction of THD in multilevel ınverter using PSO algorithm. International Journal of Advanced Research in Computer and Communication Engineering 3 (2014) 5417–5422.
17. Bahrami S, Hooshmand RA, Parastegari M. Short term electric load forecasting by wavelet transform and grey model improved by PSO (particle swarm optimization) algorithm. Energy 72 (2014) 434–442.
18. Sharafi M, Elmekkawy TY. Multi–objective optimal design of hybrid renewable energy systems using PSO–simulation based approach. Renewable Energy 68 (2014) 67–79.
19. Khansary MA, Sani AH. Using genetic algorithm (GA) and particle swarm optimization (PSO) methods for determination of interaction parameters in multicomponent systems of liquid–liquid equilibria. Fluid Phase Equilibria 365 (2014) 141–145.

20. Samet H, Hashemi F, Ghanbari T. Minimum non detection zone for islanding detection using an optimal Artificial Neural Network algorithm based on PSO. Renewable and Sustainable Energy Reviews 52 (2015) 1–18.
21. Ghanad NK, Ahmadi S. Combination of PSO Algorithm and Naive Bayesian Classification for Parkinson Disease Diagnosis. Advances in Computer Science: an International Journal 4 (2015) 119–125.
22. Yang Q, Zour HY, Zhang Y, Tang LJ, Shen GL, Jiang JH, Yu RQ. Multiplex protein pattern unmixing using a non–linear variable–weighted support vector machine as optimized by a particle swarm optimization algorithm. Talanta 147 (2016) 609–614.
23. Lin MY, Chin KS, Tsui KL, Wong TC. Genetic based discrete particle swarm optimization for Elderly Day Care Center timetabling. Computers & Operations Research 65 (2016) 125–138.
24. Shadmand S, Mashoufi B. A new personalized ecg signal classification algorithm using block–based neural network and particle swarm optimization. Biomedical Signal Processing and Control 25 (2016) 12–23.
25. Taherkhani M, Safabakhsh R. A novel stability–based adaptive inertia weight for particle swarm optimization. Applied Soft Computing 38 (2016) 281–295.

Hittite Journal of Science and Engineering, 2015, 2 (2) 165-171
ISSN NUMBER: 2149-2123
DOI: 10.17350/HJSE19030000021

Potential Evaluation of PVA-Based Hydrogels for Biomedical Applications

Emel Tamahkar[1] and Bengi Ozkahraman[2]
[1] Hitit University, Department of Chemical Engineering, Corum, TURKEY
[2] Hitit University, Department of Polymer Engineering, Corum, TURKEY

ABSTRACT

Poly vinyl alcohol (PVA)-based hydrogels prepared using freeze/thawing treatment have become increasingly important biomaterials for biomedical applications having great properties such as biocompatibility, biodegradability and high water absorbency. In this study, PVA-based physically cross-linked hydrogels were prepared with and without the presence of poly ethylene glycol (PEG) freezing at -16 °C for 16 h and thawing at room temperature for 8 h. The focus of this work was to address the effect of the addition of PEG (Mw: 2000 or 5000) and the effect of the number of freezing/thawing cycles on swelling behaviour. The Scanning Electron Microscopy (SEM) measurements demonstrated the morphological characteristics of PVA-based hydrogels indicating the formation of the macroporosity fabricated during freeze/thawing process. From the swelling tests undertaken it w as apparent that all the hydrogels exhibited unique swelling characteristics having high swelling degree at all pH values such as pH 2.1, 5.5 and 7.4 representing the pH values of stomach, blood and dermis. Thus, the hydrogels synthesized in this study present important potential for biomedical applications.

Key Words:
Physically Cross-Linked Hydrogels; PVA-Based Hydrogels; Freeze/Thawing Treatment; PVA-PEG Hydrogels; Swelling Behavior.

Article History:
Received: 2015/11/10
Accepted: 2015/11/18
Online: 2015/12/30

***Correspondence to**: Bengi Ozkahraman, Hitit University, Faculty of Engineering, Department of Polymer Engineering, Corum, Turkey*
Tel: +90 (364) 227-4533 (1227)
Fax: +90 (364) 227-4535
E-Mail: bengiozkahraman@hitit.edu.tr

INTRODUCTION

The hydrogels used, as crosslinked polymeric networks are prevalent in biomedical applications such as drug release systems, wound dressing materials, implants and dental applications since they have tunable chemical and morphological structures, high water uptake capacity and good chemical stability [1-5]. The hydrogels generally demonstrate good biocompatibility when used in contact with blood, body fluids and tissues [6, 7]. In order to prepare hydrogels, many techniques have been developed using physical methods, chemical methods in the presence of cross-linkers and radiation methods with electron beams or ultraviolet [8]. One of the useful methods for the preparation of physical hydrogel is low temperature gelation in aqueous solutions via freeze thawing [9-11]. The main benefit of the freeze/thawing method is the lack of necessity of the cross-linking agents and initiators in the synthesis of biomaterials. Thus the physically cross-linked hydrogels using freeze/thawing cycles attract a great deal of attention since they are biocompatible, non-toxic and non-carcinogenic biomaterials [12-15]. Poly vinyl alcohol (PVA) is one of the widely used polymers for the preparation of hydrogels. PVA based hydrogels have gained great importance as a biomaterial due to their permeability, high biocompatibility, high biodegradability and low toxicity [16-19]. Poly ethylene glycol (PEG) is a common hydrophilic and non-toxic biomaterial that is extensively utilized in food and pharmaceutics [20-22]. Therefore we have chosen PVA and PEG that are FDA-approved biodegradable polymers to prepare biocompatible hydrogels for biomedical applications.

In this study, we prepared PVA/PEG hydrogels via the freeze/thawing method using two different freeze-thawing cycles. The morphological structures of the hydrogels were introduced. The swelling behaviors of these hydrogels were investigated to evaluate the potential use of the hydrogels for biomedical applications. The swelling kinetic modeling of the hydrogels was also discussed in detail. The biodegradability of the resultant

hydrogels was investigated by calculating the weight loss after 15 days.

MATERIALS AND METHODS

Materials

Poly vinyl alcohol (PVA) (M_w: 145000) was purchased from Merck and poly ethylene glycol (PEG) (M_w: 2000 and M_w: 5000) were obtained from Sigma Chemical Co. Potassium chloride, sodium hydroxide, hydrochloric acid, potassium dihydrogen phosphate and sodium chloride were used for the preparation of buffer solutions and all were obtained from Merck Chemicals Ltd. The water used in the experiments was purified using a osmosis unit with a high-flow cellulose acetate membrane followed by organic/colloid removal and ion-exchange packed-bed system. The resulting purified water (deionized water) had a specific conductivity of 18 mS/cm. Buffer and sample solutions were filtered through 0.2-μm membrane.

Preparation of PVA-based hydrogels

The PVA-based hydrogels were produced without the addition of the cross-linker agents by the freeze/thawing process. At first, PVA was dissolved in aqueous solution to prepare 5 % PVA solutions by using a magnetic stirrer for 2 h at 90 °C and then the solution was slowly cooled to room temperature. 0.5 % PEG solution was prepared using two different molecular weights of 2000 and 5000. The polymer feed ratios shown in Table 1. The two polymer solutions were mixed by a magnetic stirrer at room temperature for 2 h. The mixture was placed on the petri dish. The blend solution was directly kept frozen at -16 °C for 16 hours. Afterwards, the frozen hydrogels were thawed room temperature for 8 hours. This process of freezing/thawing was repeated for 2 and 4 times. The products were immersed in an excess amount of deionized water for one week to remove the residual unreacted monomers and then were dried in air during 4 days.

Equilibrium swelling experiments

The swelling behaviors of the dried hydrogels were observed at pH 7.4 (Phosphate Buffer Solution), pH 5.5 and pH 2.1 (KCI/HCl Buffer Solution) into 20 mL solution at room temperature for five days. The values of pHs of 2.1, 5.5 and 7.4 were chosen since they present the pH of the stomach, blood and dermis. The hydrogels were periodically weighed after removing the excess water on the surface with a filter paper. The swelling degree (SD) was calculated from the following equation:

$$\% SD = (W_t - W_i / W_i) \times 100 \quad (1)$$

Where W_t and W_i represent the weights of swollen and dried state of the samples, respectively.

Characterization Studies

The gels were characterized by Fourier Transform Infrared Spectrum (FTIR) between the range of 1000-3700 cm^{-1} by a Thermo Scientific/Nicolet 6700. The SEM images of hydrogels were taken by a JEOL JSM-7001F Scanning electron microscope. The samples were dried at room temperature before being analyzed. The samples were then sputtered with a thin layer of gold before SEM measurements.

RESULTS AND DISCUSSION

PVA-based hydrogels were synthesized via freeze/thawing treatment to obtain biocompatible, biodegradable and non-toxic biomaterials. PVA and PEG was selected due to their unique properties such as biodegradability and hydrophilicity. The polymer solutions were prepared and mixed to have blend polymer solution. After the freeze/thawing process, PVA-based hydrogels were fabricated with physically cross-linking method between the polymer chains (Figure 1).

Characterization of the hydrogels

The broad hydroxyl band typical for PVA appears at 3500 cm^{-1}. Also PVA showed the characteristic bands at 2942 cm^{-1} and 1907 cm^{-1} indicating C-H stretching and C-O stretching respectively. FTIR spectra analysis of PEG showed many typical peaks at 1096, 1146, 1287, 1349, 1556, 1772 and 2886 cm^{-1}. The FTIR spectra of the

Table 1. The feed compositions and the number of the freeze/thawing cycles for the preparation of the hydrogels.

Hydrogel	*PVA (%)*	*PEG 2000 (%)*	*PEG 5000 (%)*	*Number of Freeze/Thawing Cycles*
P-2	*5*			*2*
PP2-2	*5*		*0.5*	*2*
PP5-2	*5*	*0.5*		*2*
P-4	*5*			*4*
PP2-4	*5*	*0.5*		*4*
PP5-4	*5*		*0.5*	*4*

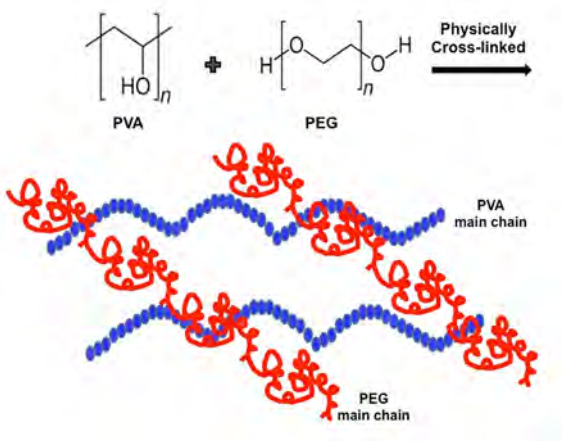

Figure 1. Schematic representation of synthesis of PVA/PEG hydrogels.

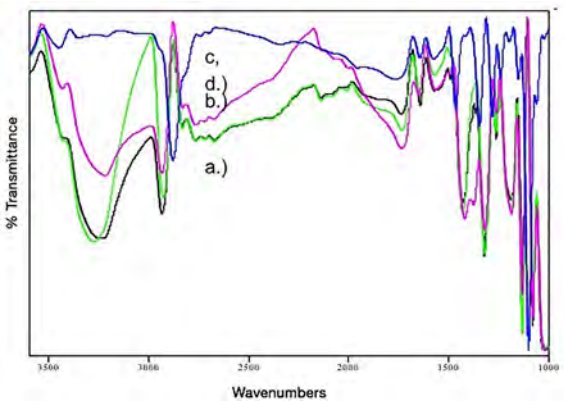

Figure 2. FTIR spectra of a.) PEG, b.)P-4, c.) PP2-4 and d.) PP5-4.

hydrogels of P-4, PP2-4, PP5-4 and PEG were shown in Figure 2. The O-H stretching band in the IR spectra of the all hydrogels which is the most characteristic peak of alcohols appears at 3355 cm^{-1} indicating hydroxyl groups. The band that was shifted to the higher wave number clearly indicates the presence of the formation of hydrogen bonds between the polymer chains. The sharp peaks at 1080 cm^{-1} which are due to ether groups of PEG appear in the FTIR spectra of all the hydrogels having PEG content.

Figure 3 shows SEM images of the hydrogels prepared in this study having different contents of PEG and two different freeze/thawing cycles. All the hydrogels introduced a porous structure indicating the formation of gelation during freeze/thawing cycles. The macroporosity of the biomaterials enable the swelling of the hydrogels facilitating the transport of the water molecules by decreasing the

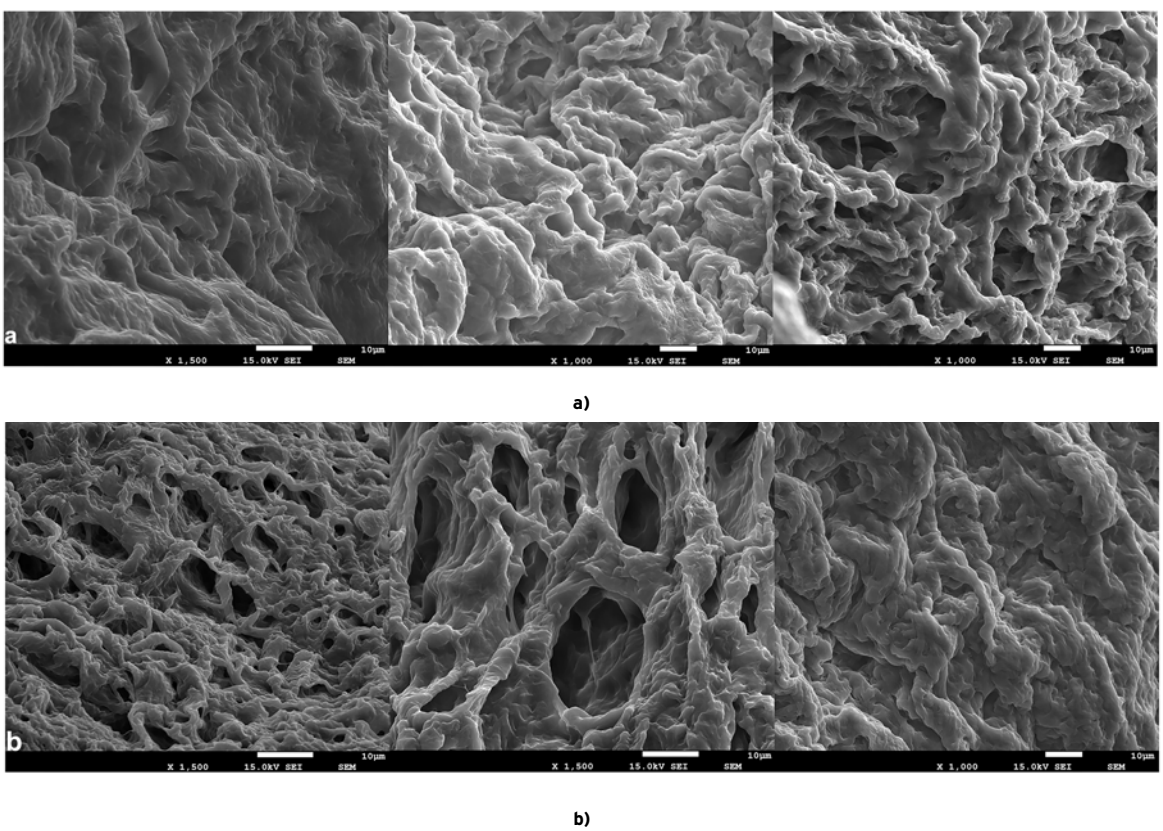

Figure 3. SEM images of the hydrogels; a) SEM images of P2, PP2-2, PP5-2 hydrogels and b) SEM images of P4, PP2-4, PP5-4 hydrogels

diffusion resistances at all of the pH values studied.

Equilibrium swelling experiments

In order to evaluate the swelling behavior of the hydrogels prepared with PEG and using two different freeze/thawing cycles, equilibrium swelling tests were performed at different pH values. In general, the swelling degrees of all the hydrogels increased with time and reached a saturation value within five days. In Figure 4, 5 and 6, the results of swelling degrees of the hydrogels were obtained at pH 2.1, 5.5 and 7.4 respectively. The increasing order of swelling degrees of the hydrogels were PP5-2>PP5-4>PP2-2>P-2>PP2-4>P-4 for all the pH values. The highest swelling degree was achieved with PP5-2 hydrogels having PEG (Mn: 5000) and after 5 days it reached the maximum value at 430 % at pH 2.1, 407 % at pH 5.5 and around 320 % at pH 7.4. The swelling properties of PP5-4 were similar to PP5-2. PP2-2 hydrogels demonstrate similar swelling behavior with PP5-2 hydrogels. This may be explained with the dominant effect of PEG on swelling capacity. The swelling degree of PP2-2 was higher than that of P-2 since the presence of PEG results in a more hydrophilic structure [23, 24]. PP2-4 exhibited less swelling degree than the swelling degrees of the other hydrogels except P-4 which has no PEG content since more physical cross linking occur with higher number of freeze/thawing cycles thus resulting a more rigid structure [20, 25, 26]. Increased freezing/thawing cycles cause high cross-linked gel due to the more crystal formation. The results herein indicated that the highest swelling degrees of all the hydrogels were achieved at pH 2.1 (431%) and the lowest swelling degrees of all the hydrogels were obtained at pH 7.4 (337%). These results indicated quite comparable manner with the hydrogels reported in the literaure [27-29].

Modeling of the swelling kinetics

To evaluate the mechanism of the swelling characteristics of the hydrogels, Fick diffusion model (2) was used.

$$M_t/M_{eq}=kt^n \quad (2)$$

where M_t and M_{eq} are the amount of the swollen weight at time t and at equilibium respectively, k is the Fick constant and n is the number indicative of the type of diffusion. For Fickian diffusion, n is reported close to 0.5 or over 0.5 in many research articles [30-33]. When the water molecules penetration is less than the penetration rate of the polymer chains, n is generally below 0.5. This situation is named as Pseudo-Fickian (or Less-Fickian). All the results demonstrate that swelling of the hydrogels was in conformity with pseudo-fickian diffusion model.

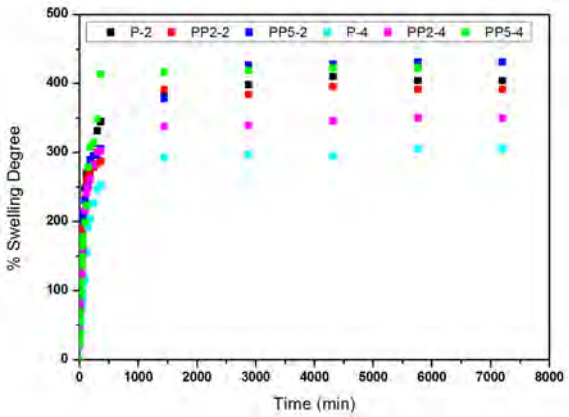

Figure 4. Swelling kinetics of PVA-based hydrogels in pH 2.1.

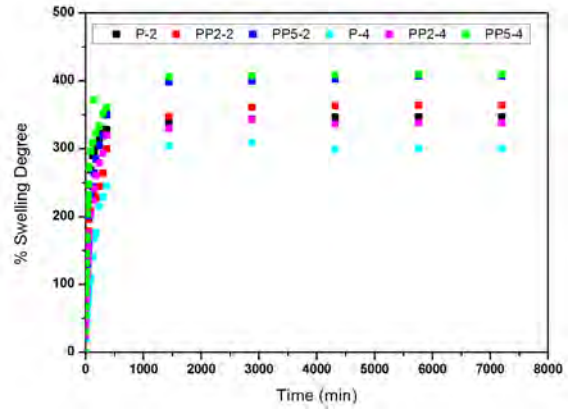

Figure 5. Swelling kinetics of PVA-based hydrogels in pH 5.5.

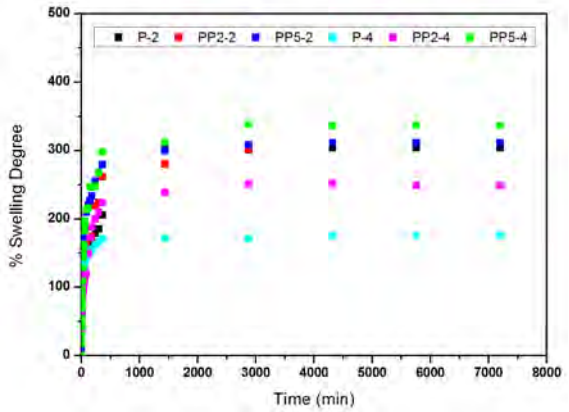

Figure 6. Swelling kinetics of PVA-based hydrogels in pH 7.4.

It was reported that n value is linearly dependent with the affinity of the polymer chains and the water molecules [34]. At all pH values, n values of the hydrogels having PEG (Mn: 5000) namely, PP5-2 and PP5-4 were higher than that of the other hydrogels (Table 2). Thus it was determined that the presence of PEG resulted in high n values.

Table 2. Swelling kinetic parameters of PVA-based hydrogels at different pHs.

Hydrogel	pH 7.4		pH 5.5		pH 2.1	
	n	k	n	k	n	k
P-2	0.170	0.286	0.152	0.357	0.142	0.321
PP2-2	0.190	0.250	0.166	0.291	0.146	0.311
PP5-2	0.193	0.231	0.186	0.270	0.181	0.278
P-4	0.178	0.252	0.175	0.253	0.50	0.498
PP2-4	0.183	0.261	0.172	0.288	0.130	0.373
PP5-4	0.199	0.223	0.170	0.308	0.176	0.283

Stability of the hydrogels

All the hydrogels were placed in aqueous solutions at different pHs for 15 days to determine the stability of the prepared hydrogels [35]. The samples were weighed every day for the first five days and fifteenth day. Table 3 shows the percantage of the weight losses for the hydrogels for the duration of the study. It was clearly seen that the least stable hydrogels were determined as hydrogels having PEG (M_w: 5000) and independent from the number of freeze/thawing cycle for all pHs providing more biodegradable biomaterial. The addition of PEG having higher molecular weight results in an increased biodegradability. The most stable hydrogels were determined as the hydrogels having PEG (M_w: 2000) at four cycles of freeze/thawing for all pHs possesing the higher cross-linked hydrogels [36].

Table 3. Stability of the hydrogels at different pHs.

pH 7.4			
Hydrogels	Initial dry weight (g)	Highest swollen weight (g)	Weight loss (%)
P-2	0.070	0.35	10.00
PP2-2	0.074	0.35	13.50
PP5-2	0.090	0.48	60.00
P-4	0.074	0.29	4.60
PP2-4	0.11	0.15	4.20
PP5-4	0.084	0.43	66.00
pH 5.5			
Hydrogels	Initial dry weight (g)	Highest swollen weight (g)	Weight loss (%)
P-2	0.084	0.37	2.30
PP2-2	0.088	0.36	11.30
PP5-2	0.099	0.41	51.80
P-4	0.090	0.36	0.00
PP2-4	0.105	0.46	6.50
PP5-4	0.098	0.40	63.50
pH 2.1			
Hydrogels	Initial dry weight (g)	Highest swollen weight (g)	Weight loss (%)
P-2	0.082	0.33	28.70
PP2-2	0.097	0.40	31.20
PP5-2	0.10	0.41	53.20
P-4	0.091	0.25	7.60
PP2-4	0.91	0.32	3.50
PP5-4	0.092	0.40	63.80

CONCLUSIONS

PVA-based physically cross-linked hydrogels were successfully produced at different number of freeze/thawing cycles and using different PEGs (M_w: 2000 and M_w: 5000). The results of the study show that:

1. The swelling properties of the hydrogels were evaluated and the highest swelling degree was achieved with PP5-2 hydrogels having PEG (M_w: 5000) and after 7 days it reached the maximum value at 430 % at pH 2.1, 407 % at pH 5.5 and around 320 % at pH 7.4.
2. All the hydrogels exhibited approximately the same swelling capacities at all pH values due to the presence of the weak ionized groups of the PVA-based hydrogels.
3. The swelling of all of the hydrogels was in conformity with pseudo-fickian diffusion model.
4. It was determined that biomaterials having better biodegradability were obtained with the addition of PEG (M_w: 5000).
5. The hydrogels prepared with four freeze/thawing cycles exhibited higher stability at all pHs.

Based on the data of this study, all the hydrogels produced in this study present significant potential having high macroporosity, high swelling capacity and biodegradability for biomedical applications such as wound dressing, drug delivery and implants.

REFERENCES

1. Hoffman AS. Hydrogels for biomedical applications. Adv. Drug Del.Rev. 64, Supplement (2012) 18–23.
2. Arica MY, şenel S, Alaeddinoğlu NG, Patir S, Denizli A. Invertase immobilized on spacer–arm attached poly(hydroxyethyl methacrylate) membrane: Preparation and properties. J. Appl. Polym. Sci. 75 (2000) 1685–1692.
3. Van Tomme SR, Storm G, Hennink WE. In situ gelling hydrogels for pharmaceutical and biomedical applications. Int.J.Pharma. 355 (2008) 1–18.
4. Berger J, Reist M, Mayer JM, Felt O, Peppas NA, Gurny R. Structure and interactions in covalently and ionically crosslinked chitosan hydrogels for biomedical applications. Eur.J.Pharma.Biopharma. 57 (2004) 19–34.
5. Chen S–C, Wu Y–C, Mi F–L, Lin Y–H, Yu L–C, Sung H–W. A novel pH–sensitive hydrogel composed of N,O–carboxymethyl chitosan and alginate cross–linked by genipin for protein drug delivery. J Controlled Release. 96 (2004) 285–300.
6. Burczak K, Gamian E, Kochman A. Long–term in vivo performance and biocompatibility of poly(vinyl alcohol) hydrogel macrocapsules for hybrid–type artificial pancreas. Biomaterials. 17 (1996) 2351–2356.
7. Singh B, Pal L. Sterculia crosslinked PVA and PVA–poly(AAm) hydrogel wound dressings for slow drug delivery: Mechanical, mucoadhesive, biocompatible and permeability properties. J.Mech.Behav.Biomed.Mater. 9 (2012) 9–21.
8. Hennink WE, van Nostrum CF. Novel crosslinking methods to design hydrogels. Adv.Drug Del.Rev. 54 (2002) 13–36.
9. [9]Nho Y–C, Lim Y–M, Gwon H–J, Choi E–K. Preparation and characterization of PVA/PVP/glycerin/antibacterial agent hydrogels using γ–irradiation followed by freeze–thawing. Korean J. Chem. Eng. 26 (2009) 1675–1678.
10. Kenawy E–R, Kamoun EA, Mohy Eldin MS, El–Meligy MA. Physically crosslinked poly(vinyl alcohol)–hydroxyethyl starch blend hydrogel membranes: Synthesis and characterization for biomedical applications. Arabian J.Chem. 7 (2014) 372–380.
11. Hassan C, Peppas N, Structure and Applications of Poly(vinyl alcohol) Hydrogels Produced by Conventional Crosslinking or by Freezing/Thawing Methods, Biopolymers PVA Hydrogels, Anionic Polymerisation Nanocomposites, Springer Berlin Heidelbergpp. 37–65, 2000.
12. Smith TJ, Kennedy JE, Higginbotham CL. The rheological and thermal characteristics of freeze–thawed hydrogels containing hydrogen peroxide for potential wound healing applications. J.Mech.Behav.Biomed.Mater. 2 (2009) 264–271.
13. Hua S, Ma H, Li X, Yang H, Wang A. pH–sensitive sodium alginate/poly(vinyl alcohol) hydrogel beads prepared by combined Ca2+ crosslinking and freeze–thawing cycles for controlled release of diclofenac sodium. Int J Biol Macromol. 46 (2010) 517–523.
14. Xiao C, Yang M. Controlled preparation of physical cross–linked starch–g–PVA hydrogel. Carohydr.Polym. 64 (2006) 37–40.
15. Kim JO, Park JK, Kim JH, Jin SG, Yong CS, Li DX, Choi JY, Woo JS, Yoo BK, Lyoo WS, Kim J–A, Choi H–G. Development of polyvinyl alcohol–sodium alginate gel–matrix–based wound dressing system containing nitrofurazone. Int.J.Pharma. 359 (2008) 79–86.
16. Gonzalez JS, Alvarez VA. Mechanical properties of polyvinylalcohol/hydroxyapatite cryogel as potential artificial cartilage. J.Mech.Behav.Biomed.Mater. 34 (2014) 47–56.
17. Kamoun EA, Chen X, Mohy Eldin MS, Kenawy E–RS. Crosslinked poly(vinyl alcohol) hydrogels for wound dressing applications: A review of remarkably blended polymers. Arabian J.Chem. 8 (2015) 1–14.
18. Oun R, Plumb JA, Wheate NJ. A cisplatin slow–release hydrogel drug delivery system based on a formulation of the macrocycle cucurbit[7]uril, gelatin and polyvinyl alcohol. J.Inorg.Biochem. 134 (2014) 100–105.
19. Baker MI, Walsh SP, Schwartz Z, Boyan BD. A review of polyvinyl alcohol and its uses in cartilage and orthopedic applications. J.Biomed.Mater.Res.Part B Appl.Biomater. 100B (2012) 1451–1457.
20. Mandal TK. Swelling–controlled release system for the vaginal delivery of miconazole. Eur.J.Pharma.Biopharma. 50 (2000) 337–343.
21. Sawhney AS, Pathak CP, Hubbell JA. Interfacial photopolymerization of poly(ethylene glycol)–based hydrogels upon alginate–poly(l–lysine) microcapsules for enhanced biocompatibility. Biomaterials. 14 (1993) 1008–1016.

22. Smith T, Kennedy J, Higginbotham C. Development of a novel porous cryo–foam for potential wound healing applications. J.Mater.Sci: Mater.Med. 20 (2009) 1193–1199.
23. Khoee S, Kardani M. Preparation of PCL/PEG superporous hydrogel containing drug–loaded nanoparticles: The effect of hydrophobic-hydrophilic interface on the physical properties. Eur.Polym.J. 58 (2014) 180–190.
24. Mansur HS, Oréfice RL, Mansur AAP. Characterization of poly(vinyl alcohol)/poly(ethylene glycol) hydrogels and PVA–derived hybrids by small–angle X–ray scattering and FTIR spectroscopy. Polymer. 45 (2004) 7193–7202.
25. Hassan CM, Peppas NA. Structure and Morphology of Freeze/Thawed PVA Hydrogels. Macromol. 33 (2000) 2472–2479.
26. Park KR, Nho YC. Synthesis of PVA/PVP hydrogels having two–layer by radiation and their physical properties. Radiat. Phys.Chem. 67 (2003) 361–365.
27. Özkahraman B, Acar I, Emik S. Removal of cationic dyes from aqueous solutions with poly (N–isopropylacrylamide–co–itaconic acid) hydrogels. Polymer Bulletin. 66 (2011) 551–570.
28. Srivastava A, Jain E, Kumar A. The physical characterization of supermacroporous poly(N–isopropylacrylamide) cryogel: Mechanical strength and swelling/de–swelling kinetics. Materials Science and Engineering: A. 464 (2007) 93–100.
29. Kathuria N, Tripathi A, Kar KK, Kumar A. Synthesis and characterization of elastic and macroporous chitosan-gelatin cryogels for tissue engineering. Acta Biomaterialia. 5 (2009) 406–418.
30. Dalaran M, Emik S, Güçlü G, İyim TB, Özgümüş S. Study on a novel polyampholyte nanocomposite superabsorbent hydrogels: Synthesis, characterization and investigation of removal of indigo carmine from aqueous solution. Desalination. 279 (2011) 170–182.
31. Wang J, Wu W, Lin Z. Kinetics and thermodynamics of the water sorption of 2–hydroxyethyl methacrylate/styrene copolymer hydrogels. J. Appl. Polym. Sci. 109 (2008) 3018–3023.
32. [32]Deen GR, Chua V, Ilyas U. Synthesis, swelling properties, and network structure of new stimuli–responsive poly(N–acryloyl–N'–ethyl piperazine–co–N–isopropylacrylamide) hydrogels. J.Polym.Sci.PartA:Polym.Chem. 50 (2012) 3363–3372.
33. Ganji F, Vasheghani–Farahani S, Vasheghani–Farahani E. Theoretical description of hydrogel swelling: a review. Iran Polym J. 19 (2010) 375–398.
34. [34]Ostrowska–Czubenko J, Gierszewska M, Pieróg M. pH–responsive hydrogel membranes based on modified chitosan: water transport and kinetics of swelling. J Polym Res. 22 (2015) 1–12.
35. Peppas NA, Tennenhouse D. Semicrystalline poly(vinyl alcohol) films and their blends with poly(acrylic acid) and poly(ethylene glycol) for drug delivery applications. Journal of Drug Delivery Science and Technology. 14 (2004) 291–297.
36. Ricciardi R, Auriemma F, De Rosa C, Lauprêtre F. X–ray Diffraction Analysis of Poly(vinyl alcohol) Hydrogels, Obtained by Freezing and Thawing Techniques. Macromol. 37 (2004) 1921–1927.

Hittite Journal of Science and Engineering, 2015, 2 (2) 173-180
ISSN NUMBER: 2149-2123
DOI: 10.17350/HJSE19030000022

Synthesis and Characterization of Poly (HEMA-co-AAc)/Diatomite Hydrogel Composites: Their Application for Heavy Metal Removal from The Aqueous Solution

Filiz Boran and Filiz Akti
Hitit University, Department of Chemical Engineering, Corum, TURKEY

ABSTRACT

Poly (2-hydroxyethyl methacrylate-co-acrylic acid)/diatomite hydrogel composite (DHC) materials were synthesized using in situ free radical addition polymerization technique. The effects of particle size and amount of diatomite were investigated on swelling properties such as the swelling degree (SD), equilibrium swelling degree (ESD) and water retention (WR) of DHC. The particle size and amount of diatomite were not affected clearly in the swelling properties. The synthesized DHC with the particle size of -45μm and the amount of 5 wt % of diatomite showed the highest swelling properties. The SD (g/g), WR (%) and ESD (%) values of hydrogel were increased up to 29.2, 45.5 and 96.7 from 1.1, 41.3 and 89.3 by adding diatomite into the structure of hydrogel, respectively. The hydrogel and DHC were characterized using Fourier transform infrared spectrometer (FTIR) and an optical microscope. Also, their thermal behavior was analyzed by differential scanning calorimeter (DSC). The FTIR spectrums showed that diatomite incorporated into the hydrogel matrix at the high amount of diatomite. The DSC results indicated that the glass transition temperature (Tg) and melting temperature (Tm) of hydrogel increased with the addition of 2 wt % diatomite. The adsorption studies were performed using the hydrogel composite including 5 wt % of diatomite.

Key Words:
Hydrogel Composite; Swelling Properties; Adsorption; Heavy Metal

Article History:
Received: 2015/10/12
Accepted: 2015/09/16
Online: 2015/12/21

***Correspondence to**: Filiz Boran,*
Hitit University, Faculty of Engineering,
Department of Chemical Engineering,
Corum, Turkey
Tel: +90 (364) 227-45 33 (13 13)
Fax: +90 (364) 227-45 35
E-Mail: filizbektas@hitit.edu.tr

INTRODUCTION

Heavy metal pollution is a serious environmental problem and it threats human health and ecosystem due to toxic and carcinogenic effects even at low concentrations. Many methods have been employed for the removal of heavy metals from water such as chemical precipitation, ion change, membrane separation and adsorption. Among the methods, adsorption is regarded as the most reliable choice due to technically and economically applicability [1- 4].

The hydrogels having three-dimensional networks of polymer chains have attracted great interests due to their high absorb, swell and water uptake capacities [5-8]. Many polymers such as polyacrylic acid (PAAc), poly (2-hydroxyethyl methacrylate, PHEMA), polyvinyl alcohol (PVA) are used in the synthesis of hydrogels. The hydrogels based on PHEMA and PAAc have been widely investigated because of their unique properties (synthetic and biocompatible) and pH and temperature sensitivities, respectively [9-11]. Inorganic minerals such as montmorillonite, sepiolite, halloysit, hydroxyapatite, attapulgite, kaolin and zeolite etc. have been loaded into the hydrogel matrix in order to increase gel strength and stability of the pure polymeric hydrogels [12-15].

In recent years, diatomite having hydrated octahedral layered magnesium aluminum silicate minerals used in the preparation of polymer composite materials due to its low density, highly porous structure, high surface area, absorption capability, active hydroxyl groups, chemical stability and low cost [13, 16-18]. The physical properties of the hydrogels can be improved by diatomite incorporating into the hydrogel structure.

In the present study, poly (HEMA-co-AAc)/diatomite hydrogel composites were synthesized using in situ free radical addition polymerization technique at different particle sizes and the amounts of diatomite. The samples were evaluated by swelling properties and were characterized using FTIR (Fourier transform infrared spectrometer), DSC (differential scanning calorimeter) and optical microscope analyses. The hydrogel composite material with 5 wt % diatomite was used for the removal of Fe^{3+}, Fe^{2+}, Cd^{2+} and Zn^{2+} metal ions from aqueous solutions.

MATERIALS AND METHODS

Materials

In the synthesis of hydrogel, 2-hydroxyethyl methacrylate (HEMA, Merck), acrylic acid (AAc, Merck) and divinyl benzene (DVB, Merck) were used as monomer pair and cross linking, respectively. Potassium per sulfate (PPS, Sigma Aldrich) and potassium meta bi sulfide (PMBS, Sigma Aldrich) chosen as initiator and accelerator pair.

$Fe(NO_3)_3.9H_2O$, $Zn(NO_3)_2.6H_2O$, $FeCl_2.4H_2O$ and $Cd(NO_3)_2.4H_2O$ (Sigma Aldrich) metal salts were used as metal ion sources in the adsorption studies.

Natural diatomite was provided from the Karaman Mining Co., Ltd., and was used at different particle size of -45, -63, -90, -125 and -180 μm. The chemical composition of diatomite is listed in Table 1.

Table 1. Chemical composition of diatomite (%, by mass)

SiO_2	Al_2O_3	CaO	Fe_2O_3	MgO
83.4	5.6	1.0	1.0	0.7

Sample Preparation

The poly (HEMA-co-AAc) hydrogels were synthesized using in situ free radical addition polymerization technique [19, 20] at room temperature and atmospheric pressure. In the synthesis of hydrogel, 80% HEMA, 20% AAc (the total monomer concentration taken as 2 mol/L) and DVB (1% molar ratio of the total monomer concentration) were dissolved in deionized water in a sealed plastic cap (4.5 x 2.5 cm; length x diameter) and then the mixture was mixed for 30 min. In another place, PPS and PMBS (0.5% molar ratio of the total monomer concentration and equal in weight) were dissolved in deionized water and then added to previously prepared monomer solution, the mixture was stirred for a further 10 min. For the formation of polymerization reaction, the mixture waited in a sealed plastic cap at room temperature for 24 h. When the polymerization reaction finished, the resulting gel product was treated with 4 M NaOH solution for 4 h in order to reach the pH value of 7. The swollen hydrogel was dehydrated several times using ethanol and dried at room temperature (Fig.1).

The DHC materials were synthesized similar to the hydrogel synthesis at different particle size (-45, -63, -90, -125 and -180 μm) and amount (2, 5, 10, and 20 wt%) of diatomite. Diatomite was added to the synthesis solution after initiator and accelerator pair.

Swelling Properties

The swelling properties of hydrogel and DHC were determined by the swelling degree (SD), equilibrium swelling degree (ESD) and water retention (WR) capacity. All the experiments were carried out using 0.2 g amount of the hydrogel.

The measurement of SD was performed by dried hydrogel which immersed in excess distilled water and kept undisturbed until it reached the equilibrium swelling [13,

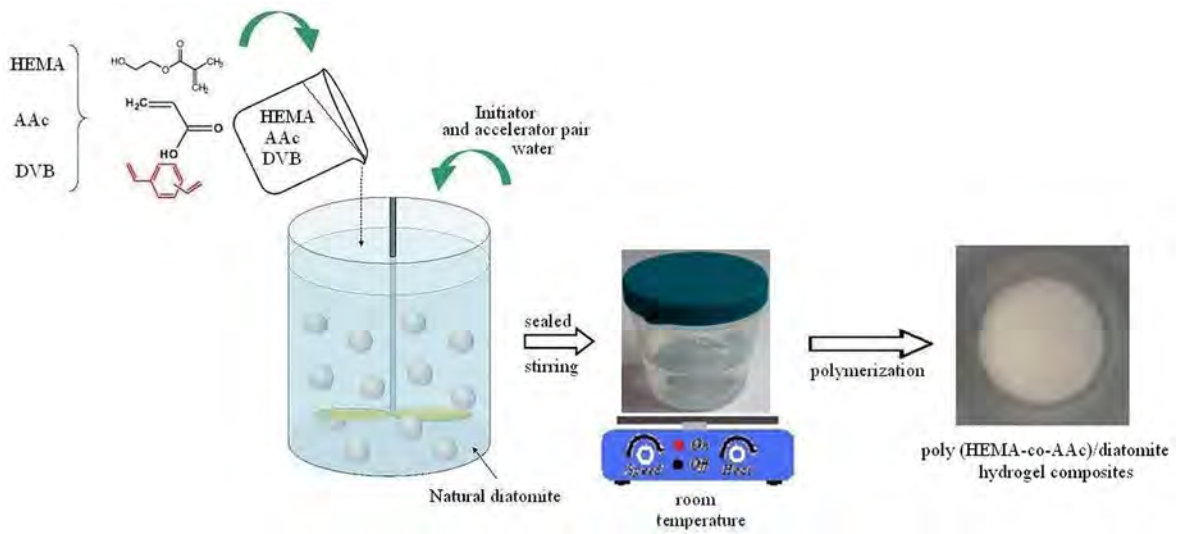

Figure 1. Schematic diagram for **the** hydrogel composite synthesis

21]. The swollen samples were dried slightly for removing the excess water of surface with paper and weighted. After weighing, the swelling capacity of hydrogel at a certain time interval was calculated according to Eq. (1).

$$SD(g/g) = (m_s - m_d)/m_d \quad (1)$$

where m_s and m_d represent the weights of swollen and dried hydrogel at room temperature, respectively.

For the equilibrium swelling degree (ESD) study, the swollen samples were dried until they reached the equilibrium at 100°C in the oven and were measured gravimetrically [15]. ESD value was calculated from Eq. (2).

$$ESD\% = [(m_s - m_{100°C})/m_s] \times 100 \quad (2)$$

where m_s and $m_{100°C}$ are the weights of swollen and dried hydrogel at 100°C, respectively.

The water retention (WR) experiments were performed after the swollen samples waited in the 0.9 wt% NaCl solution [13, 21]. The percentage of water retention was calculated using the Eq. (3).

$$WR\ \% = (m_s/m_{ds}) \times 100 \quad (3)$$

where m_s and m_{ds} are the weights of swollen hydrogel and deswollen hydrogel in 0.9 wt% NaCl solution.

Sample Characterization

Surface functional groups of the samples were investigated using a Fourier transform infrared spectrometer equipped with an ATR (Attenuated Total Reflectance) (Thermo Scientific, Nicholet IS10) in the range of 4000 to 650 cm^{-1}. The surface morphology of samples was determined by an optical microscope of 10x magnifications (Nikon eclipse LV150N, NIS-Elements 4.20). Thermal properties of the samples were performed using a differential scanning calorimetry (DSC60 Calorimeter from Shimadzu TA-60WS Instruments). The DSC thermograms of all samples were recorded in the temperature range of room temperature to 250°C at a heating rate of 10 °C/min under nitrogen atmosphere.

Adsorption Studies

The hydrogel composite having 5 wt % diatomite was used in the metal ion adsorption studies. Solutions of Fe^{3+}, Fe^{2+}, Cd^{2+} and Zn^{2+} metal ions were prepared from $Fe(NO_3)_3.9H_2O$, $FeCl_2.4H_2O$, $Cd(NO_3)_2.4H_2O$ and $Zn(NO_3)_2.6H_2O$. Adsorption experiments were performed at the metal ion concentration of 100 mg/L at natural pH and room temperature in the batch system. Firstly, approximately 0.05 g sample was added in 50 mL of metal ion solution and the mixture was stirred with a magnetic stirrer. The concentration of residual metal ions in the solution was followed by an inductively coupled plasma optical emission spectrometry (ICP-OES, Spectro Arcos) up to 24 h. The amount of metal ion adsorbed per unit mass of the hydrogel, q (mg/g) was calculated using the following Eq.(4);

$$q\ (mg/g) = [(C_o - C_e)\ V] / W \quad (4)$$

where C_o is the initial metal ion concentration (mg/L), C_e is the remaining metal ion concentration (mg/L), V is the volume of metal ion solutions (L), and W is the hydrogel mass (g) [1, 2, 4].

RESULT AND DISCUSION

The Effect of Diatomite Particle Size on the Swelling Properties of DHC

The effect of particle size of diatomite on the swelling properties of DHC was performed at particle size of -45, -63, -90, -125 and -180 µm using loading of 2 wt% diatomite which was dispersed in distilled water and added to the synthesis solution. The SD and WR properties of hydrogel composites are given in Fig. 2a and 2b, respectively.

The SD value of DHC was reached to equilibrium after 2529 min for all particle sizes. The highest values of SD, ESD and WR were obtained for particle size of -45µm as 17.2, 99.0 and 53.0, respectively (Table 2). The SD value of DHC was increased rapidly within 180 min and the water absorption capacity was increased when the particle size was reduced from -180 µm to -45 µm.

The Effect of Diatomite Amount on the Swelling Properties of DHC

The effect of the amount of diatomite was investigated using the amount of diatomite 2, 5, 10 and 20 wt% at particle size of -45µm (Fig.3). It was seen that, the SD and WR values of hydrogel composites were reached to equilibrium after 1050 min and 150 min, respectively. The synthesized hydrogel composite using diatomite loading of 5 wt% was showed the highest SD as 29.2. The highest WR value was obtained as 56.4 at the loading of

Table 2. The effect of particle size of diatomite on the swelling properties of DHC

Swelling properties	Diatomite particle size (µm)				
	-45	-63	-90	-125	-180
SD (g/g)	17.2	11.4	15.2	12.7	16.4
WR (%)	53.0	53.9	47.6	45.9	48.5
ESD (%)	99.0	98.5	98.2	97.8	98.3

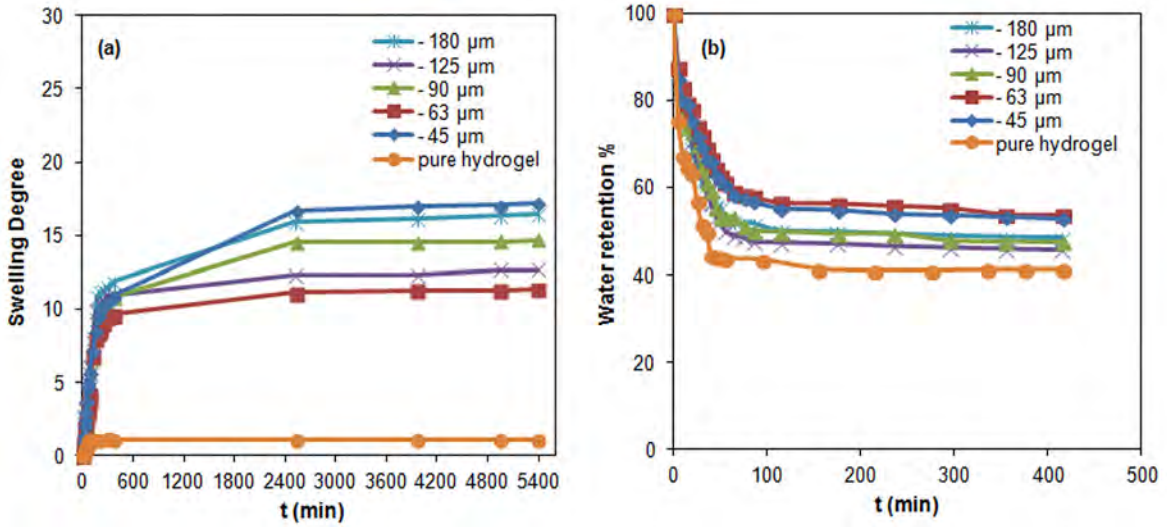

Figure 2. The effect of particle size of diatomite on (a) swelling degree and (b) water retention % of the DHC

diatomite 10 wt% (Table 3). As the hydrogel composites were compared with the pure hydrogel, it was seen that the swelling degree of composites were obtained 29 times higher than that of the pure hydrogel.

Table 3. The effect of the amount of diatomite on the swelling properties of DHC

Swelling properties	*-45µm Diatomite (wt %)*				
	0	*2*	*5*	*10*	*20*
SD (g/g)	*1.1*	*16.4*	*29.2*	*24.1*	*26.2*
WR (%)	*41.3*	*48.5*	*45.5*	*56.4*	*44.3*
ESD (%)	*89.3*	*98.3*	*96.7*	*94.9*	*97.1*

FTIR Spectrums of Samples

FTIR spectra of the pure hydrogel and DHC are given in Fig. 4. The broad band at 3000–3500 cm^{-1} is attributed to the stretching of –OH groups [21, 22-24]. The absorption bands at 2941 cm^{-1} are resulting from the C-H stretching vibrations of belong to $-CH_3$ and $-CH_2$ groups [25]. The observed peaks at 1406 cm^{-1} and 1714 cm^{-1} are due to the C-O stretching vibration of acrylic acid. The determined peak at 1406 cm^{-1} was shifted slightly to left by the increasing of amount of diatomite and the intensity of peak was decreased [12, 21]. The C=O stretching and –COOH bending of acrylic acid were observed at 1557 cm^{-1} wavenumber [15, 26].

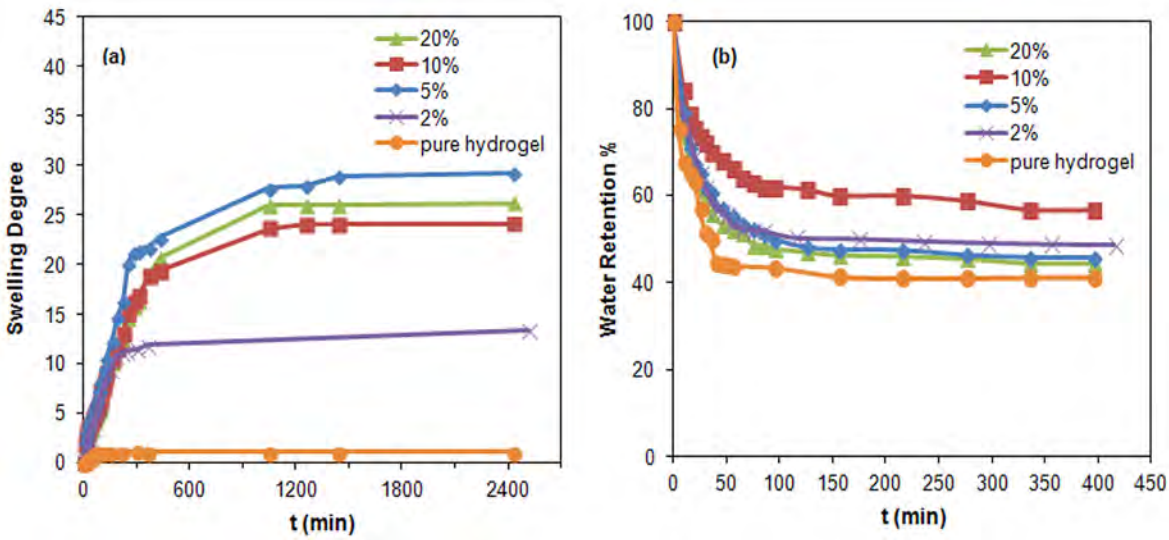

Figure 3. The effect of the amount of diatomite on (a) swelling degree and (b) water retention % of the DHC.

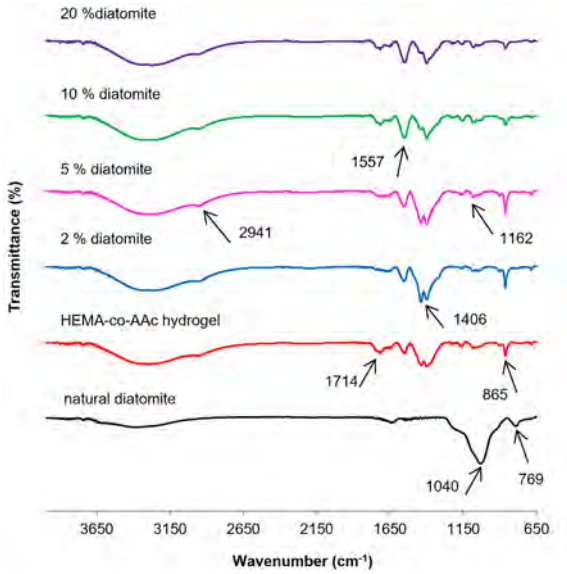

Figure 4. FTIR spectra of the natural diatomite, poly (HEMA-co-AAc) hydrogel and DHC.

Table 4. Thermal properties of the poly (HEMA-co-AAc) hydrogel and DHC.

Sample	*T_g (°C)*	*T_{m1} (°C)*	*T_{m2} (°C)*
P(HEMA-co-AAc) hydrogel	*48.89*	*110.97*	
2% diatomite	*69.79*	*124.80-135.86*	
5% diatomite	*43.59*	*74.96*	
10% diatomite	*39.57*	*91.04*	*121.31-126.55*
20% diatomite	*45.36*	*74.04*	

The absorption peak at 1162 (C–O–C) cm^{-1} was attributed to the ester group in HEMA [27]. The peaks at 769 (symmetric Si-O and Al-O) and 1040 cm^{-1} (asymmetric stretching mode of tetrahedral SiO_4, AlO_4) were resulted from silica and alumina structure of diatomite [14, 28]. These peaks disappeared in the FTIR spectra of DHC. This may be the formation of crosslinking at these bands region [22].

Analysis of Differential Scanning Calorimetry of Samples

The heating curves of the natural diatomite, poly (HEMA-co-AAc) hydrogel and DHC are presented in Fig. 5. The glass transition temperature (T_g) and melting point temperature (T_{m1} and T_{m2}) of hydrogel samples were determined from the first heating runs and results are listed in Table 4 [29]. A broad endothermic peak observed at 94.18 °C for the diatomite sample is probably due to the lost water absorbed on the diatomite structure (Fig.5) [30].

The glass transition (Tg) of P(HEMA-co-AAc) hydrogel was obtained 48.89°C. The Tg of DHC were increased from 48.89°C to 69.79°C with a loading amount of diatomite 2 wt%. The increase in the Tg arose from more regular hard domains with the incorporation of diatomite [31]. However, the Tg of the hydrogel composites with diatomite content more than 5 wt% was lowered by the addition of diatomite (Table 4). The DHC with the load of 5 and 20 wt% diatomite exhibited showed a single endothermic peak at 74.96 °C and 74.04 °C while the T_{m1} was decreased from 124.80 °C to 91.04 °C for 2 and 10 wt% diatomite loading, respectively. However,

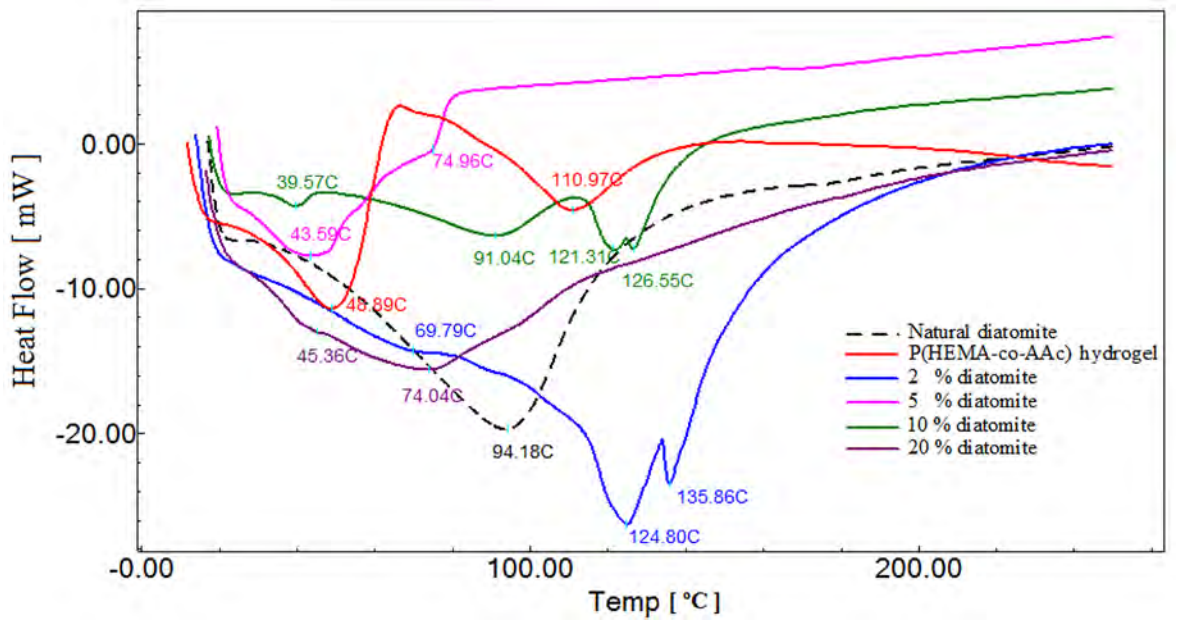

Figure 5. DSC thermograms of the natural diatomite, poly (HEMA-co-AAc) hydrogel and DHC.

the DSC curve for the DHC having content of 2 and 10 wt% diatomite showed a sharp endothermic peak at 124.80 °C (T_{m1}) and 121.31 °C (T_{m2}) followed by a small endothermic peak at 135.86 °C (T_m) and 126.55 °C (T_m), respectively. Two different endothermic melting temperature may be suggested because of recrystallization [32].

Surface Morphology of Samples

The morphology of hydrogel and DHC are given in Fig. 6. As the figure shows, macroporous structures containing interconnected crosslinked network structures were obtained. The small white particles in the optical microscope image are diatomite powders. There are many macro convex bodies in the image which are diatomite particles coated by the HEMA substrate.

Adsorption of different metal ions on the DHC

The adsorption results of Fe^{3+}, Fe^{2+}, Cd^{2+} and Zn^{2+} metal ions onto the hydrogel composite are given in Fig.7. All the metal ion adsorption experiments were done batchwise with 0.05 g hydrogel composite. As can be seen from the graph, the adsorption capacities of metal ions of Fe^{3+}, Fe^{2+}, Cd^{2+} and Zn^{2+} were found as 10.09, 3.57, 17.36 and 11.46 mg/g respectively. The shortest time to reach

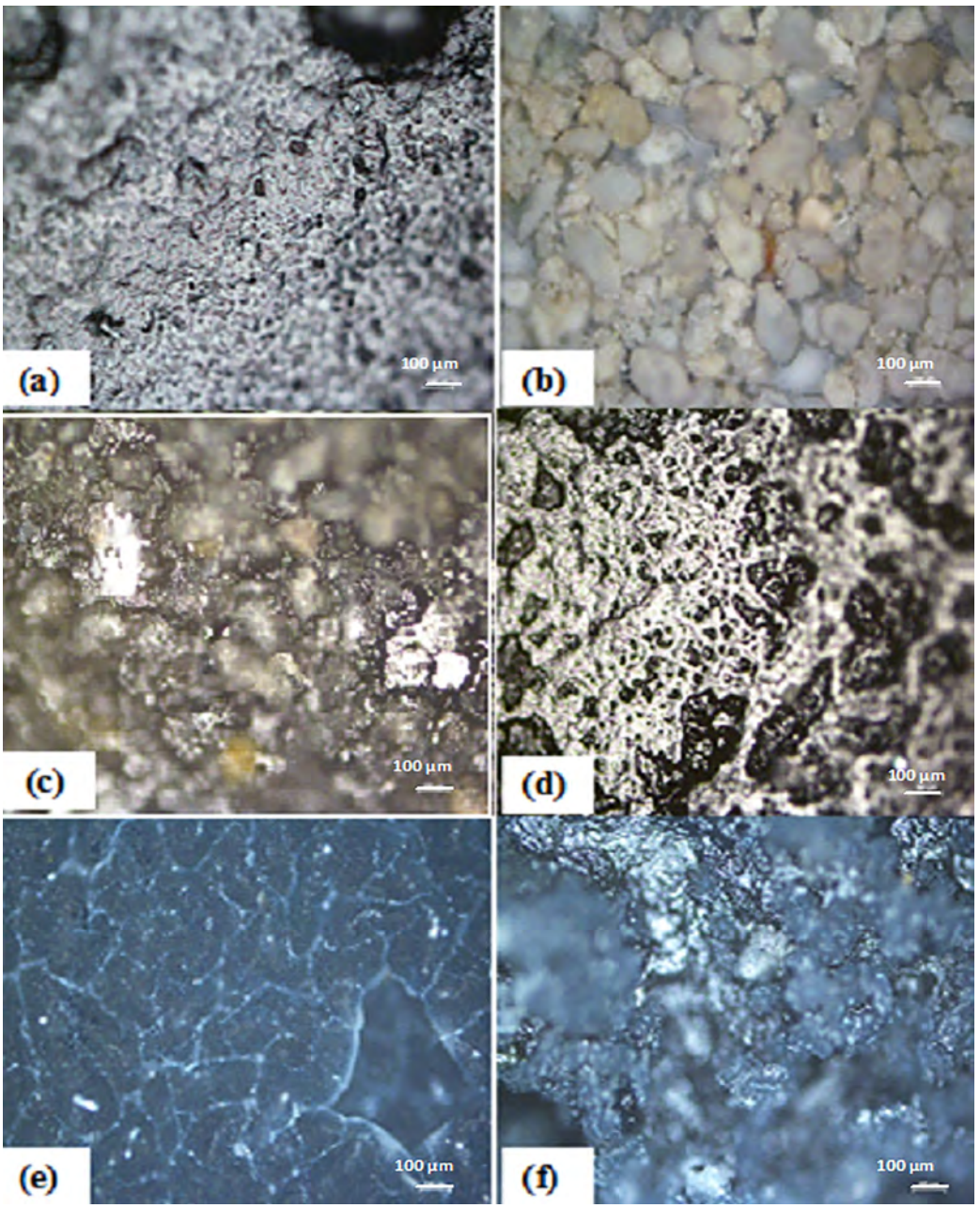

Figure 6. The images of samples (a) poly (HEMA-co-AAc) hydrogel; (b) diatomite (c-f) DHC with 2, 5, 10 and 20 wt% diatomite, respectively [Scala bar: 100 µm].

the equilibrium was achieved as 100 minutes when using Zn^{2+} solution that is quite comparable with the results reported in the literature [33-37]. These results show that the prepared hydrogel composites present great potential for Zn2+ removal having high adsorption capacity and short equilibrium time.

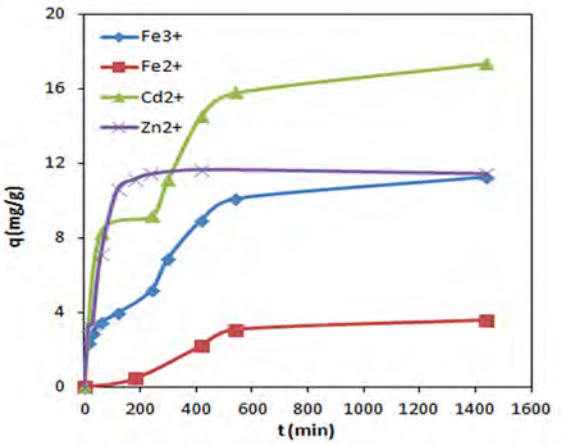

Figure 7. The adsorption capacity of Fe^{3+}, Fe^{2+}, Cd^{2+} and Zn^{2+} metal ions onto the hydrogel composite with 5 wt % diatomite.

CONCLUSION

The DHC was synthesized via in situ free radical addition polymerization technique and were characterized by FTIR, DSC and optical microscope analyses. The insertion of diatomite into the hydrogel structure was also confirmed by FTIR spectrum and optical microscope image. The maximum SD of DHC (the load of 5.0 wt% and particle size of -45μm) was found to be as 29.2 g/g while the swelling degree of the pure hydrogel was 1.1 g/g. The swelling properties of hydrogel were dramatically increased by the adding of diatomite to the hydrogel structure**.** The DSC results indicated that Tg and Tm were increased for the DHC containing 2 wt% diatomite. But, the addition more than 5 wt% of diatomite into the hydrogel structure decreased Tg and Tm. It was also determined that the hydrogel composite with 5 wt% diatomite exhibited important alternative for zinc removal.

ACKNOWLEDGMENTS

The authors thank Ömer YURDAKUL and Duygu CANDEMIR for their helps in FTIR measurements and surface morphology analyses. Also, they are grateful D. Ali KOSE, Kadir EROL, Celal Utku DENIZ and Emel TAMAHKAR IRMAK for their help and support.

REFERENCES

1. Zhu Q, Li Z. Hydrogel–supported nanosized hydrous manganese dioxide: Synthesis, characterization, and adsorption behavior study for Pb^{2+}, Cu^{2+}, Cd^{2+} and Ni^{2+} removal from water. Chemical Engineering Journal 281 (2015) 69-80.
2. Ersen Dudu T, Sahiner M, Alpaslan D, Demirci S, Aktas N. Removal of As(V), Cr(III) and Cr(VI) from aqueous environments by poly(acrylonitril–co–acrylamidopropyl–trimethyl ammonium chloride)–based hydrogels. Journal of Environmental Management 161 (2015) 243–251.
3. Hua R, Li Z. Sulfhydryl functionalized hydrogel with magnetism: Synthesis, characterization, and adsorption behavior study for heavy metal removal. Chemical Engineering Journal 249 (2014) 189-200.
4. Souda P, Sreejith L. Magnetic hydrogel for better adsorption of heavy metals from aqueous solutions. Journal of Environmental Chemical Engineering 3 (2015) 1882-1891.
5. Xia M, Wu W, Liu F, Theato P, Zhu M. Swelling behavior of thermosensitive nanocomposite hydrogels composed of oligo(ethylene glycol) methacrylates and clay. European Polymer Journal 69 (2015) 472-482.
6. Soto–Quintero A, Meneses–Acosta A, Romo–Uribe A. Tailoring the viscoelastic, swelling kinetics and antibacterial behavior of poly (ethylene glycol)–based hydrogels with polycaprolactone. European Polymer Journal 70 (2015) 1-17.
7. Güler M A, Gök MK, Figen AK, Özgümüş S. Swelling, mechanical and mucoadhesion properties of Mt/starch–g–PMAA nanocomposite hydrogels. Applied Clay Science 112-113 (2015) 44-52.
8. Baek K, Clay NE, Qin EC, Sullivan KM, Kim DH, Kong H. In situ assembly of the collagen-polyacrylamide interpenetrating network hydrogel: Enabling decoupled control of stiffness and degree of swelling. Eur. Polym. J. (2015), http://dx.doi.org/10.1016/j.eurpolymj.2015.07.044.
9. Karpushkin E, Bogomolov A. Morphology assessment of poly(2–hydroxyethyl methacrylate) hydrogels using multivariate analysis of viscoelastic and swelling properties, Polymer 58 (2015) 222–229.
10. Lazo L M, Burillo G. Novel comb–type hydrogels of net–[PP–g–AAc]–g–4VP synthesized by gamma radiation, with possible application on Cu^{2+} immobilization. Radiation Physics and Chemistry 79 (2010) 1-8.
11. Adem E, Burillo G, Bucio E, Magana C, Avalos–Borja M. Characterization of interpenetrating Networks of acrylicacid (AAc) and N–isopropylacrylamide (NIPAAm) synthesized by ionizing radiation. Radiation Physics and Chemistry 78 (2009) 549-552.
12. Zheng Y, Wang A. Evaluation of ammonium removal using a chitosan–g–poly (acrylic acid)/rectorite hydrogel composite. Journal of Hazardous Materials 171 (2009) 671-677.
13. Zheng Y, Zhu Y, Wang A. Highly efficient and selective adsorption of malachite green onto granular composite hydrogel. Chemical Engineering Journal 257 (2014) 66-73.

14. Panic VV, Velickovic SJ. Removal of model cationic dye by adsorption onto poly (methacrylic acid)/zeolite hydrogel composites: Kinetics, equilibrium study and image analysis. Separation and Purification Technology 122 (2014) 384-394.
15. Pradhan AK, Rana PK, Sahoo PK. Biodegradability and swelling capacity of kaolin based chitosan-g-PHEMA nanocomposite hydrogel. International Journal of Biological Macromolecules 74 (2015) 620-626.
16. Li B, Huang H, Guo Y, Zhang Y. Diatomite-immobilized BiOI hybrid photocatalyst: Facile deposition synthesis and enhanced photocatalytic activity. Applied Surface Science 353 (2015) 1179-1185.
17. Yu TT, Li KL, Guo XL, Li F, Huang JM, Zhang YX. Facile decolorization of methylene blue by morphology-dependence δ-MnO_2 nanosheets-modified diatomite. Journal of Physical and Chemistry of Solids, http://dx.doi.org/10.1016/j.jpcs.2015.08.013.
18. Dehestaniathar S., Khajelakzay M, Ramezani-Farani M, Ijadpanah-Saravi H. Modified diatomite-supported CuO-TiO_2 composite: Preparation, characterization and catalytic CO oxidation. Journal of the Taiwan Institute of Chemical Engineers 000 (2015) 1-7.
19. Ozkahraman B, Acar I, Emik S. Removal of cationic dyes from aqueous solutions with poly (N-isopropylacrylamide-co-itaconic acid) hydrogels. Polym. Bull. 66 (2011) 551-570.
20. Ortaboy S, Acar ET, Atun G, Emik S, Iyim TB, Gülcü G, Özgümüs S. Performance of acrylic monomer based terpolymer/montmorillonite nanocomposite hydrogels for U(VI) removal from aqueous solutions. Chemical Engineering Research and Design 91 (2013) 670-680.
21. Liua J, Lia Q, Sua Y, Yue Q, Gao B. Characterization and swelling-deswelling properties of wheat strawcellulose based semi-IPNs hydrogel. Carbohydrate Polymers 107 (2014) 232-240.
22. Huang Y, Zeng M, Ren J, Wang J, Fan L, Xu Q. Preparation and swelling properties of graphene oxide/poly(acrylic acid-co-acrylamide) super-absorbent hydrogel nanocomposites", Colloids and Surfaces A: Physicochem. Eng. Aspects 401 (2012) 97- 106.
23. Hezaveh H, Muhamad II. Modification and swelling kinetic study of kappa-carrageenan-based hydrogel for controlled release study. Journal of the Taiwan Institute of Chemical Engineers 44 (2013) 182-19.
24. Sizir U, Kose DA, Yurdakul O. Synthesis, Spectroscopic and Thermal Characterization of Non-Metal Cation (NMC) Pentaborates Salts Containing 2-amino-5-nitropyridine and 2-amino-6-methylpyridine as Cation. Hittite Journal of Science and Engineering 2 (1) (2015) 91-96.
25. Chen J, Liu M, Liu H, Ma L. Synthesis, swelling and drug release behavior of poly (N,N-diethylacrylamide-co-N-hydroxymethyl acrylamide) hydrogel. Materials Science and Engineering C 29 (2009) 2116-2123.
26. Wang J, Ren S, Guo M. Preparation and humidity controlling behaviors of sepiolite/polyacrylic acid (sodium) composite. Procedia Engineering 27 (2012) 423 - 430.
27. Gao B, Hu H, Guo J, Li Y. Preparation of polymethacrylic acid-grafted HEMA/PVP microspheres and preliminary study on basic protein adsorption. Colloids and Surfaces B: Biointerfaces 77 (2010) 206-213.
28. Zheng L, Wang C, Shu Y, Yan X, Li L. Utilization of diatomite/chitosan-Fe (III) composite for the removal of anionic azo dyes from wastewater: equilibrium, kinetics and thermodynamics. Colloids and Surfaces A: Physicochem. Eng. Aspects 468 (2015) 129-139.
29. Ali A M , Ajji Z. Investigation and characterization of PVA-g-AAc/Zolmembranes for possible practical use in separation processes. Radiation Physicsand Chemistry78(2009)927-932.
30. Meradia H, Atoui L, Bahloul L, Labiod K, Ismail F. Contribution to characterization of the diatomite for industrial application. International Conference on Technologies and Materials for Renewable Energy. Environment and Sustainability, TMREES15 Energy Procedia 00 (2015) 000-000.
31. Ganesh S B, Suresh S. U, Ajay S C. Effects of NCO:OH ratio and HEMA on the physicochemical properties of photocurable poly(ester-urethane)methacrylates. J. Coat. Technol. Res., 12 (3) 571-585, 2015.
32. Soto-Quintero A, Meneses-Acosta A, Romo-Uribe A. Tailoring the viscoelastic, swelling kinetics and antibacterial behavior of poly(ethylene glycol)-based hydrogels with polycaprolactone. European Polymer Journal 70 (2015) 1-17.
33. Meena A K, Mishra G K, Rai P K, Rajagopal C, Nagar P N. Removal heavy metal ions from aqueous solutions using carbon aerogel as an adsorbent. Journal of Hazardous Materials B122 (2005) 161-170.
34. Amuda O S, Giwa A A, Bello L A. Removal of heavy metal from industrial wastewater using modified activated coconut shell carbon. Biochemical Engineering Journal 36 (2007) 174-181.
35. Hui KS, Chao C Y H, Kot S C. Removal of mixed heavy metal ions in wastewater by zeolite 4A and residual products from recycled coal fly ash. Journal of Hazardous Materials B127 (2005) 89-101.
36. Mohammad M, Maitra S, Ahmad N, Bustam A, Sen T K, Dutta B K. Metal ion removal from aqueous solutions using physic seed hull. Journal of Hazardous Materials 179 (2010) 363-372.
37. Ozkahraman B, Acar I, Güçlü K, Güçlü G. Synthesis of Zn(II) Ion-Imprinted Polymeric Adsorbent for Selective Removal of Zinc from Aqueous Solution. Polymer-Plastics Technology and Engineering 50 (2011) 216-219.

Hittite Journal of Science and Engineering, 2015, 2 (2) 181-185
ISSN NUMBER: 2149-2123
DOI: 10.17350/HJSE19030000023

Determination of Fundamental Probiotic Properties of *Lactobacillus* Strains Isolated from Turkish Local Yogurt

Gulcin Alp Avci[1], Emre Avci[1], Asiye Aslı Emniyet[2] and Burcin Ozcelik[3]
[1] Hitit University, Department of Molecular Biology and Genetics, Corum, TURKEY
[2] Hitit University, Department of Biology, Corum, TURKEY
[3] Hitit University, Department of Biology, Corum, TURKEY

ABSTRACT

Lactic acid bacteria have benefits for the digestive tract. They and some of their methabolic products stimulate the immune system and therefore regarded as probiotic. A good quality probiotic must have some features like stomach acid resistance, bile reduction, exopolysaccharide production and must be able to keep the intestinal mucosa. This research was aimed to determinate the resistance to acid, tolerance to bile and exopolysaccharide (EPS) production capacity of all *Lactobacillus* strains isolated from home-made yogurt gathered from 17 different Turkish villages. All strains were researched for acid and bile tolerance and EPS production. All values were measured spectrophotometrically. Acid and bile tolerance levels of isolates were in a different rate. And also, the lowest and highest EPS amounts were calculated as 20.82 and 121.01 mg/L, respectively. These features can be reference points to choose a probiotic microorganism.

Key Words:
Probiotic; *Lactobacillus*; Acid and Bile Tolerance; Exopolysaccharide Production.

Article History:
Received: 2015/11/10
Accepted: 2015/11/23
Online: 2015/12/30

***Correspondence to**: Gulcin ALP AVCI, Hitit University, Faculty of Science and Arts, Department of Molecular Biology and Genetics, Corum, TURKEY*
Tel: +90 (364) 2277000/1609
Fax: +90 (364) 2277005
E-Mail: gulcinalp@hitit.edu.tr, alp.gulcin@yahoo.com

INTRODUCTION

Lactic acid bacteria (LAB) convert carbohydrate to lactic acid and another product. They are gram-positive, aero-tolerant, catalase negative microorganisms and they do not include spore in their cell. They protect foods with fermentation from the spoilage and give a different taste and texture them. Very different fermented foods can be produced by using LAB like yogurt, butter, cheese, sausage and cereals products include probiotics [1-3]. LAB have a 'Generally Recognized as Safe' (GRAS) classification because of exopolysaccharides (extracellular polysaccharides, EPS) production specialty. EPS are metabolites located extracellular surface and emerge from the milk fermentation of LAB [4,5]. EPS production, because of its useful health effects, ensures functionality to the foods which include LAB [6]. The genera of *Lactobacillus, Streptococcus* and *Lactococcus* are EPS-producing lactic acid bacteria [7]. In general, LAB ferments sugars, produce lactic acid and can biosynthesis EPSs from this fermentation reaction [8]. LAB fermentation uses not only sugars but also some kind of fats, proteins, and organic acids which improve the food's typical aroma and texture. Milk was exposed to rapid acidification and lactic fermentation that prohibit proliferation of pathogens. Fermented milk products include EPS such as yogurt and cheese. In order to stay alive and be able to settle down the gastrointestinal area of LAB should express tolerance to acid and bile [9]. Lactic acid bacteria which are taken at diet should withstand stomach acid (pH 2) to reach intestine and to show probiotic effects. So a lactic acid bacteria strain must be resistant for acid and bile salt concentration [1, 10]

In this research, we aimed to determine acid and bile tolerance and EPS production capacity of *Lactobacillus* strains isolated from Turkish home-made yogurt.

MATERIAL & METHODS

Yogurt samples and isolation of *Lactobacillus* strains

Yogurt samples were collected from seventeen different villages in Corum/Turkey. Each sample

diluted with phosphate saline buffer (PBS) from 10^{-1} to 10^{-6}. After dilution, lactic acid bacteria were isolated from Turkish local yogurt using MRS (**De Man, Rogosa and Sharpe**) broth and MRS agar. Diluted samples inoculated on MRS agar plates and they were incubated in 37°C. After incubation, single colonies were examined with a microscope and lactic acid bacteria were chosen by using gram staining and microscopical morphology. Cultures were kept in -86°C until experiment.

Determination of acid and bile tolerance

To determine the ability to reach the intestine through the stomach's highly acidic environment of *Lactobacillus* sp., the stomach environment was simulated. For this purpose, MRS Broth pH was adjusted as pH 3.0, 4.0, 5.0, 7.0, 8.0 and 6.2 (control) using 1 N HCl acid before sterilization. The optical density of isolates was measured of 600 nm. These isolates inoculated to the pH adjusted medium in 1% ration. After inoculation, cultures were incubated at 37±1°C temperature for 16-18 hours. When incubation was completed, optical density was measured spectrophotometrically in 600 nm wavelength.

To determine the bile tolerance a similar method to the acid resistance of bacteria was used. MRS broth was sterilized. After sterilization, bile salt was added to broth by sterilization with micro-filter in different rates (0.15%, 0.2%, 0.3 and 0.4 %, respectively). The optical density of isolates was measured of 600 nm. These isolates inoculated to the pH adjusted medium in 1% ration. After inoculation, cultures were incubated at 37±1°C temperature for 16-18 hours. When incubation was completed, optical density was measured spectrophotometrically in 600 nm wavelength.

Determination of EPS production capacity

EPS production capacity was studied using the phenol-sulfuric acid method modified by Alp [10]. Firstly, to release exopolysaccharide, lactic acid bacteria were exposed to some processes. 1 ml active culture (Optical Density ≈ 600) were put in Eppendorf tube and boiled in 96°C for 10-15 minutes. Then samples were cooled until room temperature and 1 ml trichloracetic acid (TCA) was added and centrifuged at 13000 rpm for 25 minutes. After this process, 1 ml ethyl alcohol added in the tube and centrifuged again. When centrifugation was finished, pellets could be obtained on the bottom of the tubes. The pellet was separated from the supernatant, solved in 1 ml ethyl alcohol and precipitated with centrifugation. Finally precipitated sample was separated from alcohol and solved 1 ml distilled water. Sample became ready to be used for the phenol-sulfuric acid method.

According to the phenol sulfuric acid method, 0.5 ml phenol and 5 ml sulfuric acid were added above the 1 ml samples in the tube. The tube was incubated in room temperature for 10 minutes and when the time up samples were mixed well. After stirring, the tube was incubated in 30°C for 15-20 minutes. When incubation was complete, optical density (OD) was measured spectrophotometrically at 490 nm wavelength.

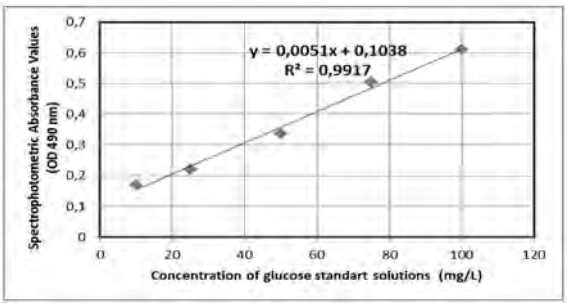

Graphic 1. Calibration line which was drawn with glucose standart solutions and its equation

Statistical Analysis

All experiment was done in triplicate. The results were determined to standard curve. Statistical analyzes were performed on the data by IBM SPSS 22.0 and standard curve graphic was drawn using Microsoft Office Excel program.

RESULTS AND DISCUSSION

Determination of acid and bile tolerance

Probiotic microorganisms should resist the stressful conditions of the stomach and intestine [9]. Acid and bile are believed to be the most detrimental factor affecting growth and viability of lactobacillia [11, 12]. Therefore, these strains may be expected to stay alive in acid and bile conditions that exist in fermented food products or gastrointestinal area [13]. The acid tolerance of the lactobacillus strains isolated from the Turkish local yogurt was determined using different pH values. The results determined by the spectrophotometric method shown in Table 1. When we look at the results, stomach acid resistance was found as quietly low. As acid ratio increased, bacterial density was decreased in the medium. When we considered all the strains, bacterial density was decreased at pH 3. And also, bile tolerance of the lactobacillus strains was determined very similar to acid tolerance experiment. Tolerance to the bile in the intestine by *Lactobacillus* strains varied according to the bile salt rate. Although the concentration of the bile salt 0.15 % has triggered the growth of bacteria, media were including bile salt in rate 0.2%, 0.3% and 0.4% inhibited the development of all strains in general. Bile tolerance data illustrated in Table 2. In literature, some *Lactobacillus*

Table 1. Results of acid resistance in *Lactobacillus* strains isolated from Turkish local yogurt.

Strains	Control[b] (pH 6.2)	pH[a]				
		3.0	4.0	5.0	7.0	8.0
Strain 1	1.40±0.00	0.13±0.01	0.59±0.01	1.39±0.04	1.22±0.20	0.80±0.02
Strain 2	1.39±0.01	0.16±0.02	0.52±0.08	1.40±0.07	1.19±0.06	0.91±0.11
Strain 3	1.52±0.28	0.14±0.00	0.52±0.00	0.89±0.01	1.02±0.01	0.92±0.08
Strain 4	1.72±0.00	0.15±0.00	0.68±0.01	1.51±0.23	0.99±0.02	0.81±0.01
Strain 5	1.58±0.15	1.13±0.00	0.19±0.00	1.53±0.03	1.51±0.00	1.89±0.02
Strain 6	1.42±0.01	0.36±0.02	0.64±0.02	1.34±0.06	1.05±0.05	0.86±0.08
Strain 7	1.47±0.10	0.13±0.00	0.19±0.00	1.14±0.14	0.42±0.05	0.36±0.01
Strain 8	0.98±0.00	0.16±0.00	0.26±0.01	0.96±0.03	0.66±0.03	0.69±0.01
Strain 9	1.61±0.02	0.14±0.00	0.11±0.00	0.20±0.00	0.30±0.00	0.35±0.03
Strain 10	0.82±0.03	0.26±0.00	0.30±0.00	0.99±0.41	0.61±0.05	0.71±0.06
Strain 11	1.32±0.00	0.23±0.00	0.36±0.00	0.76±0.01	1.44±0.02	1.69±0.03
Strain 12	0.99±0.02	0.20±0.07	0.24±0.00	0.78±0.01	0.39±0.01	0.32±0.00
Strain 13	1.11±0.07	0.15±0.00	0.23±0.01	1.02±0.17	0.68±0.06	0.35±0.03
Strain 14	1.42±0.00	0.13±0.00	0.13±0.00	0.72±0.01	1.74±0.02	1.89±0.03
Strain 15	1.69±0.08	0.13±0.00	0.14±0.00	1.22±0.19	2.04±0.10	1.89±0.08
Strain 16	0.92±0.03	0.16±0.02	0.30±0.00	0.99±0.43	0.61±0.05	0.71±0.06
Strain 17	1.78±0.05	0.13±0.01	0.25±0.00	1.78±0.05	1.26±0.16	0.49±0.05
Mean±SD	1.36±0.26	0.22±0.01	0.33±0.24	1.09±0.27	1.00±0.02	0.92±0.21
P values		.484	.951	.736	.657	.793

[a]Sprectrophotometric optical density of the strains in 600 nm

[b]Control pH: pH of the medium was used in the study.

SD. Standard Deviation. P values compared each bile concentrations with control, P=0.05.

Table 2. Results of the bile salt resistance of *Lactobacillus* isolated from Turkish local yogurt.

Strains	Control[b]	Bile concentration (%)[a]			
		0.15	0.20	0.30	0.40
Strain 1	1.55±0.00	1.18±0.00	1.08 ±0.04	1.16±0.01	0.86±0.04
Strain 2	1.59±0.01	1.31±0.07	0.75±0.05	0.85±0.04	0.39±0.01
Strain 3	1.48±0.02	1.08±0.00	1.04±0.00	1.14±0.01	0.73±0.02
Strain 4	1.54±0.06	1.24±0.07	1.09±0.01	1.12 ±0.02	0.55±0.03
Strain 5	1.33±0.05	1.39±0.14	0.35±0.03	0.48±0.03	0.35±0.00
Strain 6	1.64±0.00	1.21±0.01	0.73±0.00	0.51±0.02	0.37±0.00
Strain 7	1.64±0.06	1.28±0.02	0.45±0.02	0.46±0.03	0.35±0.06
Strain 8	1.62±0.02	1.28±0.08	0.95±0.02	1.07±0.01	0.64±0.03
Strain 9	1.94±0.06	0.33±0.01	0.31±0.00	0.32±0.00	0.34±0.00
Strain 10	1.44±0.03	1.15±0.03	1.07±0.01	0.90±0.03	0.90±0.02
Strain 11	1.52±0.02	1.18±0.00	1.04±0.00	1.12±0.01	0.68±0.02
Strain 12	1.44±0.06	1.18±0.02	0.42±0.03	0.39±0.01	0.34±0.00
Strain 13	1.45±0.04	1.08±0.03	1.10±0.02	1.06±0.04	0.86±0.00
Strain 14	1.70±0.01	1.67±0.00	1.60±0.00	1.59±0.00	1.50±0.01
Strain 15	1.52±0.07	1.01±0.04	0.68±0.02	0.47±0.02	0.25±0.05
Strain 16	1.60±0.02	1.38±0.07	1.09±0.05	1.21±0.00	0.73±0.03
Strain 17	1.42±0.06	0.91±0.03	0.58±0.02	0.30±0.00	0.28±0.00
Mean±SD	1.55±0.09	1.16±0.19	0.84±0.35	0.83±0.60	0.59±0.41
P values		.022	.506	.436	.467

[a]Concentration of the bile salt in percentage of the broth

[b]Control: As a control MRS broth not include bile salt was used in the study.

SD. Standard Deviation. P values compared each bile concentrations with control. P= 0.05.

strains from infant feces were tested for their ability to tolerance low pH (pH 3.0) and bile salt. Stay alive ratio of the test strains ranged between 0.01%-68.3% at pH 3.0 and 10.3%-57.4% at 0.15% bile salts [14]. It was also shown that *Lactococcus lactis* subsp. *lactis* lost viability at pH 2.0 and 0.2 % bile salts [15]. In another research, LAB strains isolated from local Korean food showed bile salt and acid resistance [16]. When we compare the results of the current work with those results in the literature, our strains have shown a good performance at low pH and bile salts.

Determination of EPS levels

Exopolysaccharides (EPS) are sugar polymers that secreted by the microorganism out of the cell. For microorganism, EPS provide resistance to harmful effects of nutrients and enzymatic activities in habitats and also EPS are important for cells in microbial aggregates to communicate each other [17]. In our study, EPS production capacities were determined spectrophotometrically using the phenol- sulphuric acid method and calculated. EPS production amounts of all *Lactobacillus* strains isolated from Turkish local yogurt was showed at Table 3. As shown Table 3, the lowest and highest EPS amounts were calculated respectively as 20.82 and 121.01 mg/L. In this study EPS production was observed in all strains but depending on the strain amount of EPS products were determined different. According to Korakli et al (2002), *Bifidobacterium* and *Lactobacillus* strains isolated from cereal products have EPS production activity, and this ensures fermentation and is important for typical flavor [3]. Vinderela G et al (2006), suggested that exopolysaccharide is protective immunity, maintaining intestinal homeostasis, enhancing the IgA production at both the small and large intestine level and influencing the systemic immunity through the cytokines released to the circulating blood [4]. Alp and Aslım (2010) reported that lactic acid bacteria and Bifidobacterium isolated from breast milk and infant feces showed acid resistance and bile salt tolerance. There has been a correlate with EPS production capacity and acid production-bile salt reduction activity [10].

CONCLUSION

Scientists have studied many times to determine the probiotic features of some *Lactobacillus* strains of LAB from the natural isolates to improve human health quality. These microorganisms are used biotechnological and industrial area and still we have not enough information their physiological features. These experiments provide an improvement to our knowledge about lactic acid bacteria as a probiotic microorganism. In this research, we determined to acid resistance, bile tolerance and EPS production capacity of *Lactobacillus* strains isolated from Turkish local yogurt. In Turkish population consuming yogurt and other local main Corum/Turkey. So, it is valuable in terms of the being an indicator of public health. Choosing most efficient strain from local yogurt and to develop its features may contribute to

Table 3. Exopolisaccaride (EPS) production amounts of *Lactobacillus* strains isolated from Turkish local yogurt.

Strains	*OD_{490} Value*	*EPS Amount (mg/L)*
Strain 1	*0.278*	*34.15*
Strain 2	*0.258*	*30.24*
Strain 3	*0.247*	*28.07*
Strain 4	*0.250*	*28.67*
Strain 5	*0.317*	*41.02*
Strain 6	*0.210*	*20.82*
Strain 7	*0.226*	*23.96*
Strain 8	*0.395*	*57.09*
Strain 9	*0.317*	*41.8*
Strain 10	*0.383*	*54.74*
Strain 11	*0.367*	*51.60*
Strain 12	*0.374*	*52.98*
Strain 13	*0.389*	*55.92*
Strain 14	*0.328*	*43.96*
Strain 15	*0.366*	*51.41*
Strain 16	*0.721*	*121.01*
Strain 17	*0.404*	*58.86*
Mean±SD	*0.34±0.09*	*46.84±17.47*

OD_{490}. Optical density was measured spectrophometrically at 490 nanometer wavelength.
SD. Standard Deviation.

obtain healthier properties.

ACKNOWLEDGEMENTS

The authors wish to acknowledge this research experiment was a part of Hitit University Scientific Research Project Program (Project no.SYO01.13.001).

REFERENCES

1. Doleyres Y, Fliss I, Lacroix C. Increased stress tolerance of Bifidobacterium longum and Lactococcus lactis produced during continuous mixed–strain immobilized–cell fermentation. J Appl Microbiol 97 (2004) 527-39.
2. Sömer VF, Akpınar D, Başyiğit Kılıç G. *Lactobacillus casei*'nin Sağlık Üzerine Etkileri ve Gıda Endüstrisinde Kullanımı, Gıda 37 (3) (2012) 165–172.
3. Korakli M, Ganzle MG, Vogel RF. Metabolism by bifidobacteria and lactic acid bacteria of polysaccharides from wheat and rye, and exopolysaccharides produced by Lactobacillus sanfranciscensis, Journal of Applied Microbiology 92 (2002) 958-965.
4. Vinderola G, Perdigo´n G, Duarte J, Farnworth E, Matar C. Effects of the oral administration of the exopolysaccharide produced by Lactobacillus kefiranofaciens on the gut mucosal immunity. Cytokine 36 (2006) 254-260.
5. Sutherland IW. The biofilm matrix an immobilized but dynamic microbial environment. Trends in Microbiology. 9 (5) (2001) 222–227.
6. Welman AD, Maddox IS. Exopolysaccharides from lactic acid bacteria: perspectives and challenges. Trends in Biotechnology 21(6) (2003) 269–275.
7. Kranenburg van R, Vos HR, van Swam, Kleerebezem M, de Vos WM. Functional analysis of glycosyltransferases genes from Lactococcus lactis and other gram–positive cocci: complementation, expression, and diversity. J. Bacteriol. 181 (1999) 6347-6353.
8. Laws A, Gu Y, Marshall V. Biosynthesis, characterisation, and design of bacterial exopolysaccharides from lactic acid bacteria. Biotechnology Advances. 19 (2001) 597-625
9. Pan X, Chen F, Wu T, Tang H, Zhao Z. The acid, bile tolerance and antimicrobial property of Lactobacillus acidophilus NIT. Food Control 20 (2009) 598-602.
10. Alp G, Aslim B. Relationship between the resistance to bile salts and low pH with exopolysaccharide (EPS) production of Bifidobacterium spp. isolated from infants feces and breast milk, Anaerobe 16 (2010) 101-105.
11. Lin W, Hwang C, Chen L, Tsen H. Viable counts, characteristic evaluation for commercial lactic acid bacteria products. Food Microbiology 23(2006) 74-81.
12. Brink M, Todorov SD, Martin JH, Senekal M, Dicks LMT. The effect of probiotics on production of antimicrobial compounds, resistance to growth at low pH and in the intestinal mucus. J. Appl. Microbiol (2006) 1364–5072.
13. Noriega L, Gueimonde M, Sánchez B, Margolles A, de los Reyes–Gavilán CG. Effect of the adaptation to high bile salts concentrations on glycosidic activity, survival at low pH and cross–resistance to bile salts in *Bifidobacterium*. International Journal of Food Microbiology, 94 (1) (2004) 79-86.
14. Xanthopoulos V, Litopoulou–Tzanetaki E, Tzanetakis N. Characterization of *Lactobacillus* isolates from infant faeces as dietary adjuncts. Food Microbiol 17(2000) 205–215.
15. Kim W, Ren J, and W. Dunn (1999). Differentiation of *Lactococcus lactis* subspecies lactis and subspecies cremoris strains by their adaptive response to stress. Fems Microbiol. Lett. 171(1999) 57–6.
16. Chang JH, Shim YY, Cha SK, Chee1 KM. Probiotic characteristics of lactic acid bacteria isolated from kimchi. Journal of Applied Microbiology 109 (2010) 220-230.
17. Laspidou CS, Rittmann BE. A unified theory for extracellular polymeric substances, soluble microbial products, and active and inert biomass. Water Research. 36 (2002) 2711-2720.

Hittite Journal of Science and Engineering, 2015, 2 (2) 187-191
ISSN NUMBER: 2149-2123
DOI: 10.17350/HJSE19030000024

The Cytologic Investigation of Brown Adipose Tissue of *D.laniger* (Felten & Storch, 1968) (Mammalia: Rodentia) in Hibernation

Aydın Ozluk[1], Diler Salman[1], Dilek Yılmaz[2], Ahmet Cilak[3], Nursel Gul[4] and Menderes Suicmez[1]
[1] Hitit University, Department of Biology, Corum, TURKEY
[2] Hitit University Training and Research Hospital, Department of Pathology, Çorum, TURKEY
[3] Physio-Thermal Healthy Living Centre, Balgat/Ankara/Turkey
[4] Ankara University, Department of Biology, Ankara, TURKEY

ABSTRACT

This study was conducted on the *D.laniger* samples maintained in the laboratory condition after collecting from the natural environment. Investigations were performed in the experimental groups in the active period at the time of hibernation and at the period of intermediate awakening during hibernation. The brown adipose tissue (BAT) of these animals investigated was removed by dissection. The tissue samples dissected were prepared for the analysis at Transmission Electron Microscopy (TEM) and photographed. It was observed for the *D. laniger* BAT cells in the active period that there are high amount mitochondria and whereas the scarce amount of the lipid droplets. However, it was drawn attention to BAT cell of animals in hibernation that there plenty of capillary vessels and lipid droplets between them. The contact between lipid droplets with each other in the cytoplasm of animal at intermediate awakening in the winter during hibernation and cytoplasmic material loss and melting of mitochondria cristae partly were observed. These results of this study suggest that it may be useful to understand the importance of the brown adipose tissue of some hibernating mammals.

Key Words:
Dryomys Laniger; Brown Adipose Tissue; Mitochondria; Hibernation.

Article History:
Received: 2015/11/12
Accepted: 2015/12/07
Online: 2015/12/30

***Correspondence to**: Aydın Ozluk, Hitit University, Faculty of Science and Arts, Department of Biology, Corum, TURKEY*
Tel: +90 (364) 2277000/1631
Fax: +90 (364) 2277005
E-Mail: aydinozluk@hitit.edu.tr

INTRODUCTION

Hibernation and torpor

All living things show various adaptations to cope with the challenges in the environmental conditions. With the changes in the temperature at winter, the challenges arise such as to find food to meet the required amount of energy. Some of the behavioral characteristics of the animals are intended to prevent or to reduce the heat loss from the body (1). The selection of suitable feeding grounds with the desired thermal property is one of the behaviors that reduces heat loss. Nest construction and also behaviors to come together are the behaviors that are aimed at maintaining the body temperature. Most living things are somnolent and minimize their energy requirements by lowering metabolism in order to overcome these kinds of difficulties (1). Mammals has been evolved as having the proficiency to keep the body temperature higher than that of the environment (ambient) and at that level constant using the heat produced by internal origin (endogenous) (2). The hibernation is a kind of lethargy and sleepiness state to conserve energy and to get rid of unsuitable conditions in winter. It is a seasonal activity routinely and estimated that begins with the arrival of winter. The warm-blooded animals have an inherent response mode for cold winter conditions. These animals show long sleep periods, reducing metabolic rate and lowering the body temperature (3-7). Their metabolic rate at the time of deep sleep is much slower than that of the normal daily life(8,9).

The period of inactivity and sleepiness at which the metabolism is extremely slow, and thus the body temperature decreases, hereafter the heart rate decreases is called torpor. The hibernation also known as seasonal sleep consists of the total of torpor phases in a specific subsequent order (7,10,11).

In winter, at regular intervals, the short awakening

times are observed to eat the nutrients stored in the nest and to excrete. The body temperature is raised to survive during these awakening times. These short awakening times become increasingly rare towards the middle of winter, the duration of torpor increases, whereas the torpor durations decreases towards the spring and the animals remain awake for longer periods of time. This model is available for all of the living things having real hibernation (9, 11, 12).

The cytology of adipose tissue in mammals

There are 2 types of adipose tissue known with different location, structure and color. Their distribution in the body, the color, the relationship with the veins and the metabolic activity are different (13). White (unilocular) adipose tissue (adipose tissue made up of cells with a single space), when fully developed, are made up of cells containing a yellow big lipid drop in the middle of cytoplasm. Brown adipose tissue (multilocular adipose tissue) is made of cells including a plenty of lipid droplets and copious amounts of brown mitochondria. The amount of BAT owned by animals hibernating or surviving in a cold environment is quite high as compared to others (13). Both types of the adipose tissues mentioned have also a rich blood flow.

There are many reports published by many researchers reporting the distinguishing features between white and brown adipose tissue. The most important difference between these two tissues is that brown adipose tissue has more than one (multiloculer) lipid droplets, whereas the white adipose tissue has only one (uniloculer).

The BAT cells are rich in terms of mitochondria. White adipose tissue has mitochondria in the cell size of 0.3 μ and a small number of, on the contrary brown lipid cell has the one in the cell size of 0.5 μ and many. The cristae extends along the entire width of the mitochondrion. The mitochondrion has tightly arranged cristae with the amount of approximately 8-15 extending along the mitochondria which are 1 μ in lengths. The cristae is slightly curved. This case is the phenomenon observed in the mitochondrion of many active tissue cells. The mitochondrion is oval or rounded in shape (14).

In addition to a big lipid droplet observed via light microscope, the presence of small lipid droplets in each adipose cell was proven by the electron microscopy studies. There is no membrane around the small lipid droplets. There is basal lamina around each adipose cell (15). It was reported that there are a plenty of free ribosomes in the brown adipose cells of young and adult animals, and polysomes can be monitored partly (16.17).

Physiology of brown adipose tissue

All mammalian brown adipose tissue has the same structural appearance. The physiology of this tissue was understood comprehensively for hibernating animals (18). Brown adipose tissue is used especially by hibernating animals as a source of energy for the continuity of life during sleep. This tissue located especially in the dorsa and neck area of hibernating animals is vital for living things. It is usually located around the shoulders of rats and a few other mammals. This tissue is seen in a few places in the human embryo and newborn babies, moreover, it is known that this tissue remains in some places after birth. It becomes crucial because of the fact that it protects newborn against the cold by creating heat in the first few months usually after birth. Brown adipose tissue cells generate heat by the oxidation of fatty acids stored in lipids (19). The main function of the brown adipose tissue is to produce heat. It is estimated that the maximum respiratory capacity of that tissue is 10 times greater than that of skeletal muscle (20).

In the case of a real hibernator, the body temperature at the time of deep sleep can fall into the values of 3-4°C. Increasing the body temperature from the lower level to the previous higher level (36-37°C) during awakening takes a considerable time (9). The location of this heat production is the brown adipose tissue. The body is heated to a certain extend by the heat released from the brown adipose tissue stimulated (21,22). The protein named by thermogenin enables the release of energy from ATP as in the form heat energy. Later, the animal begins to tremble, heart beat and respiration rate rise and the animal wake up. (23,24).

When the studies are examined, there are more or less a few studies on hibernation and brown adipose tissue found, but most of these studies are about the physiology of this tissue (18,25,26). Nonetheless, ultrastructural studies on brown adipose tissue are fewer. In some of these studies, some important organs were examined using light and electron microscopy, morphometric, cytochemical and immunocytochemical approaches (27). Our cytological study on the BAT will contribute to literature with lack of such studies about the hibernation of mammals.

MATERIAL AND METHODS

This study was carried out on the *D.laniger* samples collected from the natural environment in Antalya, Elmalı district and stored in the laboratory. The first step in the investigation was to form different experimental group cared separately in different cages to determine the hibernation biology of specie. The animals were fed

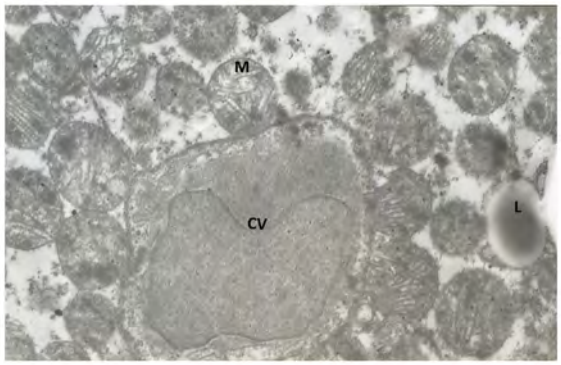

Figure 1. The brown adipose tissue of *Dryomys laniger* in active period. M**:** Mitochondria, **L:** Lipid Droplet, **CV:** Capillary Vessel (TEM, x 10.000)

on regular during controls carried out daily. *D.laniger* specimens were hosted in steel cages (37x17x12 cm) individually during the time they were in the laboratory. The odorless litter and cotton were placed in the cages as a bedding and nest material, respectively. In addition, enough water and feed were given to each of *D.laniger* specimens (28). The samples were taken via dissection from BAT of these animals. Dissection procedures were conducted through 3 different times as when some specimens were in active period, when some were in torpor and when some in intermediate awakening in winter.

The hibernation of *D.laniger* samples

During the experimental period, the temperature of the laboratory where the *D. laniger* samples were placed was ranged between 24°C-7°C. By the start of hibernation, the illumination period was set so as to have constant dark conditions and this condition was continued until the end of the heterothermal period. During this period, the experimental animals were not given food and water. This application, i.e. no to give food and water throughout the heterothermal period to the animals brought to the laboratory from the nature, is a standard for research on hibernation (28,29).

The preparation of slides for transmission electron microscope

First fixation was performed in phosphate buffered 3% glutaraldehyde (pH = 7.2, +4°C) for 4 hours for the *D.laniger* samples, removed by the dissection in the laboratory. Later on, it was washed every half hour for 2 hours only with the buffer solution used for fixation solution. Second detection operations were performed for 1 hour in 1% osmium tetroxide solution freshly prepared in phosphate buffer. After fixation, the block was prepared in resin. Block resin were mixed in an order and performed as follows:

Araldite CY – 212……..……..……..10cc
HY-964 (DDSA)…… ……..……..10cc
DY-064 (DMP-30)……..……..0,5cc
Dibutyl phthalate……..……..0,5cc

The polymerization process was performed at 45°C for 24 hours and at 60°C for 24 hours by placing samples into the resin. As a following process, thin and semi thin section were obtained using ultra microtome from these hardened blocks. After thin sections were taken on the grid, they were stained using uranyl acetate-lead citrate dye. Section prepared in this way were examined and photographed via JEOL 100 CX-II Transmission Electron Microscope.

RESULTS AND DISCUSSION

BAT has been investigated by several researchers with great interest for various animal species in terms of ontogenetic, histological, histochemical, electron microscopic, physiological and biochemical view (13,18). Brown adipose tissue is significantly important due to its role in regulating body temperature during hibernation. The color of this tissue is coming from blood vessels and cytochromes in mitochondria those it contains. Although white adipose tissue spreads throughout the body, brown adipose tissue is concentrated in the body's specific locations (20). In our study, the BAT has attracted markedly great attention as the brown color on the back of the animal in hibernation.

In our study, it was determined as a result of the examination of brown adipose tissue of *D.laniger* in active period that there are mitochondria in various sizes, capillary vessel and rarely present lipid droplets. Despite the abundance of mitochondria, it was observed a few lipid droplets in the cell. The most conspicuous formations in the *D. laniger* BAT cells are lipid droplets and mitochondria. The lack of cytoplasmic material in cell cytoplasm was drawn attention (Figure 1). During the active period, despite the excess mitochondria in the cells, the existence of a lack of the lipid droplets may be thought to be related with the energy usage in the active period (30). Similarly, some other authors have interpreted that this shortage is because of the usage of glycogen and lipid content of these cells and so reduces of the volume as a first response of brown adipose cells against cold effects (31).

There are mitochondria observed located between the spherical lipid droplets in BAT cell of *D.laniger* samples in torpor during the winter (Figure 2a and 2b). The number of lipid droplets in the cells of animals in torpor was higher as compared to those in the active period. It was observed that there are plenty of capillary vessels between the cells in the

general structure of the tissue (Figure 2a). The abundance of capillary vessels carrying blood to the brown adipose tissue has been expressed in other studies performed in rats (13).

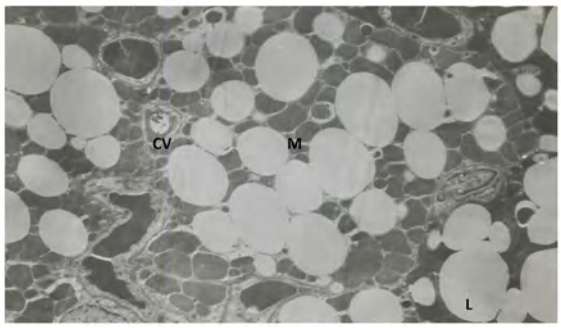

Figure 2a. The brown adipose tissue of *D.laniger* in torpor period. **M:** Mitochondria, **L:** Lipid Droplet, **CV:** Capillary Vessel (TEM, x 1900)

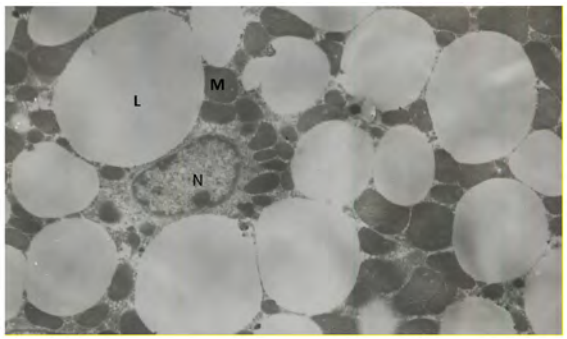

Figure 2b. The brown adipose tissue of *D.laniger* in torpor period. **M:** Mitochondria, **L:** Lipid Droplet, **N:** Nucleus (TEM, x 4800).

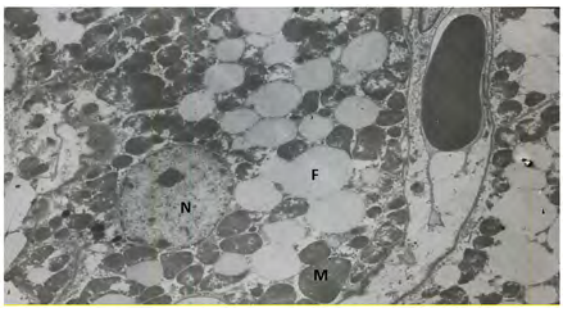

Figure 3a. The brown adipose tissue of *D.laniger* in intermediate awakening period in winter **N:** Nucleus, **F:** Fused lipid droplets, **M:** Mitochondria (TEM, x 2900).

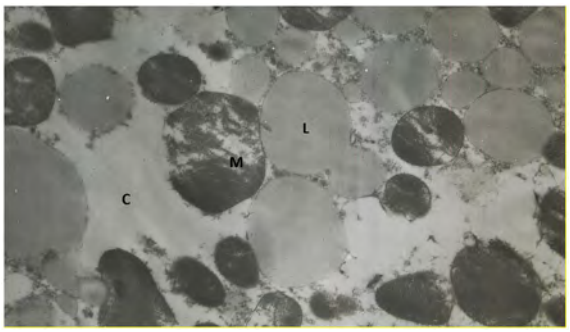

Figure 3b. The brown adipose tissue of *D.laniger* in intermediate awakening period in winter. **L:** Lipid droplets, **M:** Mitochondria, **C**: Cytoplasmic material loss (TEM, x 4800).

It was observed that the lipid droplets within the cytoplasm of adipose cells of *D. laniger* in intermediate awakening period during winter were in contact with each other and the nucleus has a spherical shape (Figure 3a). There are partly cytoplasmic material loss and lysis in the cristae of mitochondria observed (Figure 3b). It was found that brown adipose tissue of *D. laniger* sample in an intermediate awakening period of the hibernation has mitochondria in various sizes. With a higher magnification ratio in the SEM studies, it can be seen if an adipose cell considered in detail that there are damages in the cells attracted more attention (Figure 3b). Similarly, Çiftçi (32) has reported in a study conducted in rats that lipid droplets in the BAT cells are not wrapped with a membrane and these lipid droplets are combined with each other. The lipid droplets in BAT cells of the rat in his study were so great sometimes so that two or three of these droplets can cover the entire optic field of electron microscopy. In BAT of *D. laniger*, the big, rough and notched nucleus located near the center of the cell had no significant difference in terms of chromatin distribution as compared to those of the animals in active period. Çiftçi (1989b) has reported in another study he worked that there are no differences between lipid droplets and mitochondria of control group rats to which he has injected physiological saline solution and those of the experimental group.

There are some differences between the findings of the researchers working on the KYD of rats in the cold environment. Many of these differences may be dependent on the various factors such as the age of the animal in the cold, living conditions in the cage etc.

CONCLUSIONS

In this study, *D.laniger* samples were examined in uncontrolled laboratory temperature. Some of the animals have been observed during the summer in active period, some of them during winter in hibernation period and some others during the winter in the intermediate awakened periods. Brown adipose tissue fragments taken from the interscapular part of these samples were photographed in the Transmission Electron Microscope. When the *D. laniger* samples in active period were analyzed via images taken from electron microscopy it was determined that there are plenty of mitochondria in the BAT cells, but rarely the lipid droplets. The lack of cytoplasmic material of the cell cytoplasm was drawing attention. There were mitochondria observed located between spherical lipid droplets in various sizes due to the features of the adipose tissue in BAT cells of *D.laniger* samples in hibernation (torpor) period. There are plenty of capillary vessels observed between the cells in the general structure of the tissue. There were lysis of

cristae in mitochondria, contact between lipid droplets and partly cytoplasmic material loss observed in the *D.laniger* cells during the intermediate awakening period of hibernation.

The significant part of the biological richness of a country constitutes mammals. This study is important due to the fact that *D. laniger* is chosen because of being an endemic specie and there is no such study conducted before in the literature. The findings obtained from this study has enabled us to have information about brown adipose tissue of *D. laniger* in our country. Moreover, this study is also important because it gave us new information about hibernation encountered in some mammals. The work we have conducted here is an original study. The information obtained from this study is intended to form the basis for future hibernation related studies on this species.

REFERENCES

1. Boyer BB, Barnes BM. Molecular and metabolic aspects of mammalian hibernation. Bio Science. 49 (1999) 713–724.
2. Carey H, Andrews MT, Martin SL. Mammalian Hibernation: Cellular and molecular responses to depressed metabolism and low temperature. Physiol. Rev. 83 (2003) 1153–1181.
3. Nelson RA. Protein and fat metabolism in hibernating bears. Fed. Proc. 39 (1980) 2955–2958.
4. Hofmann RA. Terrestrial animals in the cold: hibernators. In: Dill DC, Adolph EF and Wilber CG. (eds). Handbook of Phisiology, Section 4, Adaptation to the Environment. American Physilogical Society. Washington DC. (1964) 379–403.
5. Lyman CP. Who is who among the hibernators. In Hibernation and torpor in mammals and birds (Edited by Lyman CP, Willis JS, Malan A and Wang LCH), (1982) 12–36. Academic Press, New York.
6. Wang LCH. Mammalian hibertation. In: Grout BWW and Morris GJ (eds). The effects of low temperature on biological systems. Edward Arnold, London. (1987) 349–386.
7. French AR. The patterns of mammalian hibernation, American Scientist. 76 (1988) 569–575.
8. Storey KB, Storey JM. Metabolic rate depression and biochemical adaaptation in anaerobiosis, hibernation and estivation. Q. Rev. Biol., 65 (1990) 145–174.
9. Geiser F and Ruf T. Hibernation versus daily torpor in mammals and birds: Physiological veriables and classification of torpor patterns. Physiol Zool. 68 (1995) 935–966.
10. Wade O. The behaviour of certain spermophiles with special references to estivation and hibernation. J. Mamm. 11 (1930) 160–188.
11. Barnes BM. Freeze avoidance in a mammal body temperatures below 0°C in an Arctic hibernator. Sci. 244 (1989) 1593–1595.
12. 12. Geiser F. Metabolic rate and body temparature reduction during hibernation and daily torpor. First published 2003. Annu. Rev. Physiol. 66 (2004) 239–274.
13. Çiftçi N. Tiroksinin oda ısısında sıçan skapular arası kahverengi yağ dokusuna etkisinin elektron mikroskobu düzeyinde incelenmesi. Ondokuz Mayıs Üniversitesi Tıp Fakültesi Dergisi, 6(1989a) 465–472.
14. Suter ER. The fine structure of brown adipose tissue. I. Coldinducen changes in the rat. J. Ultrastruct Research. 26 (1969) 216–241.
15. Altunkaynak BZ and Özbek E. Yağ dokusu endokrin bir organ mıdır? Dicle Tıp Dergisi. 32 (2005) 211–217.
16. Revel JP and Sheridan JD. Electrophysiological and ultrastructural studies of intercellular function in brown fat. The Jornual of Physiology. 194 (1968) 34–35.
17. Lindberg O. Brown adipose tissue. American Elsevier Pub. Co., New York , USA, (1970) 337.
18. Watanabe J, Kanamura S, Tokunaga H, Sakaida M and Kana K. Significance of increase in glucose 6–phosphatase activity in brown adipose cells of cold–exposed and starved mice. The Anatomical Record. 219 (1987) 39–44.
19. Sternberg S. Brown Adipose Tissue. Second edition histology for pathologist. Ed: Stephen S. Sternberg. Lippincott–Raven publishers. (1997) 173–175.
20. Wang LCH and Abbots B. Maximum thermogenesis in hibernators: magnitudes and seasonal variations. In: Musacchia XJ and Jansky L (eds). Survival in the cold. Elsevier, Amsterdam. (1981) 77–97.
21. Himms–Hagen J. Brown adipose tissue and cold acclimatation. In: Trayhurn P and Nicholls DG (eds). Brown adipose tissue. Edward Arnold, London. (1986) 214–268.
22. Kolaeva SG, Kramarova LI, Ilyasova FE. The kinetics and metabolism of the cells of hibernating animals during hibernation. Int. Rev. Cytol. 66 (1980) 148–169.
23. Zancanaro C, Malatesta M, Merigo F, Benati D, Fakan S and Gazzanelli G. Ultrastructure of organs and tissue of dormice during hibernation. In: Heldmaier G and Klingenspor M (eds). Life in the cold, Springer, Berlin. (2000) 269–276.
24. Akay MT. Genel Histoloji. Palme Yayıncılık, Ankara (1999) 200.
25. Kramarova LI, Bronnikov GE, Ignat'ev DA, Cannon B and Nedergaard J. Adrenergic receptor density in brown adipose tissue of active and hibernating hamsters and ground squirrels. Comparative Biochemisrty and Physiology, Part A. (2007) 408–414.
26. Malatesta M, Fakan S, Zancanaro C. Cell and tissue structural modifications in hibernating dormice. Hystrix It. J. Mamm. 16 (2005) 41–52.
27. Göney G. D.laniger (Felten & Storch, 1968) (Mammalia: Rodentia)'in davranışsal açıdan hibernasyonunun incelenmesi. Yayınlanmamış Yüksek Lisans Tezi, Hitit Üniversitesi Fen Bilimleri Enstitüsü, Çorum. (2011).
28. Vaughan DK, Gruber AR, Michalski ML, Seidling J, Schlink S. Capture, care, and captive breeding of 13–lined ground squirrels, Spermophilus tridecemlineatus. Lab Animal. 35 (2006) 33–40.
29. Horwitz BA, Hamilton JS and Kott KS. GDP binding to hamster brown fat mitochondria is reduced during hibernation. Am. J. Physiol. 249 (1985) 689–693.
30. Andrews JF, Richard D, Jennings G and Trayhurn P. Annals of nutrition and metabolism. 30 (1986).
31. Çiftçi N. Tiroksinin soğuk ortamda sıçan skapular arası kahverengi yağ dokusuna etkisinin elektron mikroskobu düzeyinde incelenmesi. Ondokuz Mayıs Üniversitesi Tıp Fakültesi Dergisi. 6(1989b) 373–383.

NATIONAL & INTERNATIONAL SCIENTIFIC EVENTS

MULTIPHYSICS 2016

Venue: ZHAW School of Engineering
Location: Zurich, Switzerland

BEGINS: Dec 08, 2016
Ends: Dec 09, 2016

11th Triennial Congress of the World Assoc.ion of Theoretical and Comput. Chem. (WATOC2017)

Venue: Gasteig München GmbH
Location: Munich, Bavaria, Germany

BEGINS: Aug 27, 2017
Ends: Sep 01, 2017

2016 8th International Conference on Bioinformatics and Biomedical Technology (ICBBT 2016)

Venue: Hotel Colón
Location: Barcelona, Spain

BEGINS: Jun 10, 2016
Ends: Jun 12, 2016

2016 7th International Conference on Environmental Science and Technology (ICEST 2016)

Venue: HOTEL COLÓN
Location: Barcelona, Spain

BEGINS: Jun 10, 2016
Ends: Jun 12, 2016

2016 5th International Conference on Petroleum Industry and Energy (ICPIE 2016)

Venue: Colón Hotel Barcelona
Location: Barcelona, Spain

BEGINS: Jun 10, 2016
Ends: Jun 12, 2016

2016 3rd Int. Con. on Mech. and Mechatronics Res. (ICMMR 2016)--Ei & Scopus (ICMMR 2016)

Venue: Crowne Plaza Chongqing Riverside
Location: Chongqing, China

BEGINS: Jun 15, 2016
Ends: Jun 17, 2016

2016 2nd Int. Con. on Power Control and Opt. (ICPCO 2016)--Ei & Scopus (ICPCO 2016)

Venue: Crowne Plaza Chongqing Riverside
Location: Chongqing, China

BEGINS: Jun 15, 2016
Ends: Jun 17, 2016

WCSE 2016 6th International Workshop on Computer Science and Engineering _ EI,SCOPUS

Venue: Park Hotel Tokyo
Location: Tokyo, Japan

BEGINS: Jun 17, 2016
Ends: Jun 19, 2016

ICEIM 2016 5th Int. Con. on Engineering and Innovative Materials_SCOPUS, Ei Compendex

Venue: Amb. Row Hotel Suites by Lanson Place
Location: Kuala Lumpur, Malaysia

BEGINS: Sep 10, 2016
Ends: Sep 12, 2016

2016 3rd Int. Conf. on Power and Energy Systems Engineering (CPESE 2016)

Venue: Kitakyushu Int. Conference Center
Location: Kitakyushu, Japan

BEGINS: Sep 08, 2016
Ends: Sep 10, 2016

ICRED 2016 2nd International Conference on Renewable Energy and Development_Ei, Scopus

Venue: Kitakyushu Int. Conference Center
Location: Kitakyushu, Japan

BEGINS: Sep 08, 2016
Ends: Sep 10, 2016

2016 5th International Conference on Nutrition and Food Sciences --Ei Geobase

Venue: Ananta Legian Hotel
Location: bali, Indonesia

BEGINS: Jun 25, 2016
Ends: Jun 27, 2016